

QUANTITATIVE RESERVOIR CHARACTERIZATION
INTEGRATING SEISMIC DATA
AND GEOLOGICAL SCENARIO UNCERTAINTY

A DISSERTATION
SUBMITTED TO THE DEPARTMENT OF ENERGY RESOURCES
ENGINEERING AND THE COMMITTEE ON GRADUATE
STUDIES OF STANFORD UNIVERSITY
IN PARTIAL FULFILLMENT OF THE REQUIREMENTS
FOR THE DEGREE
OF DOCTOR OF PHILOSOPHY

Cheolkyun Jeong
May 2014

Abstract

The main objective of this dissertation is to characterize reservoir models quantitatively using seismic data and geological information. Its key contribution is to develop a practical workflow to integrate seismic data and geological scenario uncertainty.

First, to address the uncertainty of multiple geological scenarios, we estimate the likelihood of all available scenarios using given seismic data. Starting with the probability given by geologists, we can identify more likely scenarios and less likely ones by comparing the pattern similarity of seismic data. Then, we use these probabilities to sample the posterior PDF constrained in multiple geological scenarios. Identifying each geological scenario in metric space and estimating the probability of each scenario given particular data helps to quantify the geological scenario uncertainty.

Secondly, combining multiple-points geostatistics and seismic data in Bayesian inversion, we have studied some geological scenarios and forward simulations for seismic data. Due to various practical issues such as the complexity of seismic data and the computational inefficiency, this is not yet well established, especially for actual 3-D field datasets. To go from generating thousands of prior models to sampling the posterior, a faster and more computationally efficient algorithm is necessary. Thus, this dissertation proposes a fast approximation algorithm for sampling the posterior distribution of the Earth models, while maintaining a range of

uncertainty and practical applicability.

Lastly, the proposed workflow has been applied in an actual reservoir. The field, still in the early stage, has limited well data, seismic data, and some geological observations. Accordingly, the proposed workflow can guide several processes, from selecting geological scenarios to suggesting a set of models for decision makers. The case study, applied in a turbidite reservoir in West Africa, demonstrates the quantitative seismic reservoir characterization constrained to geological scenarios. It contains a well log study, rock physics modeling, a forward simulation for generating seismic responses, and object-based prior modeling. As the result, we could pick some promising geological scenarios and its geological parameters from seismic data using distance-based pattern similarity. Next, based on the selected geological scenarios, Metropolis sampler using Adaptive Spatial Resampling (M-ASR) successfully sampled the posterior conditioned to all available data and geological scenario uncertainty.

Acknowledgments

I would be a person who believes the best is yet to come as Frank Sinatra said. However, I have already tasted the best thing because living and studying at Stanford could never be better in any other places. My five years journey for a Ph.D. degree has been the most wonderful experience in my life. I have felt privileged to study in Stanford University with the greatest faculty and the smartest students. Recalling my past years I am fully indebted to all the people who have made this possible.

First and foremost, I would like to express my gratitude to Professor Tapan Mukerji for being an exceptional adviser. Like parents, he always taught me gently and precisely. Whenever I faced obstacles in my research, Tapan was there to rescue me. Whenever I made mistakes, Tapan corrected me with incredible patience. Also he was always approachable and open-minded for any discussion. He was not only a great teacher for my research but also a good mentor for my life. He encouraged me to approach various scientific investigations and help me in my life-changing events. Without his guidance, encouragement, consistent support and brilliant ideas, this dissertation would have been impossible. I firmly believe that the opportunity to work with Tapan was the best of luck in my lifetime.

I want to thank Professor Jef Caers for providing me the incredible support and guidance. He always motivated and taught me how to make excellent scientific works. Thanks to his endless research ideas and insightful advices, my work could reach the final destination. I really appreciate his help with my heart.

I would also like to express my gratitude to Professor Gary Mavko. His mentorship and remarkable classes have tremendously enriched my resources of research. His critical comments, feedback and ideas always helped me to shape and refine my PhD.

I wish to acknowledge the contributions of Céline Scheidt and Gregoire Mariethoz for co-working on my research. Thanks to their contributions and valuable comments, my research could move forward and be done. I express my sincere gratitude to my co-authors.

I also thank the members of my PhD committee: Roland Horne and Steve Graham. I have learned a lot of geology from Steve, both in class and discussion. The discussions with Steve and Eli Moises have been very helpful for my thesis. Also I acknowledge Tim McHargue and Ezequiel Gonzalez for their constructive comments.

I express a great deal of thanks to the SCRF program and its sponsors for the financial support during five years of my stay at Stanford. Along with that, I sincerely thank Thuy Nguyen for extraordinary administrative support.

I acknowledge Hess Corporation for providing us an excellent dataset from Equatorial Guinea, offshore West Africa. A special thanks to Steve Utchtyl and Scott Marler for support.

I acknowledge ConocoPhillips and Schlumberger for providing me the opportunities to learn real practice through their summer internship programs. Thanks to Claude, Lin, Mario, Yongshe, Sahyun, Selin, Denis, Jaideva and Vikas for their help during these internships.

I thank all the current and former students of SCRF. You all have enriched my life. I hope we can share our life forever as a SCRF family. Sincerely, it was my honor to be a member of SCRF.

I am thankful to ERE Koreans: Jaehoon, Kwangwon, Hyungki, Yongduk, Wonjin, Sandy, Jieun, and Kyungjin. I am also very thankful to all KBSK members. You all

made my time at Stanford as a wonderful experience.

I also send my sincere gratitude to my previous professors who help to study here in Stanford: Joomyung Kang, Jonggeun Choe, and Changsoo Shin.

None of this could have been possible without the support of my family. I really appreciate my parents, Byungjoo Jeong and Hwasoon Lim, and sister, Heekyung. I also appreciate my parents-in-law. They have always been encouraging me and providing unconditional love and selfless support.

Lastly, I dedicate this dissertation to my wife, Yoojin Shin. Without her patience, encouragement and endless support, I would not be able to finish my PhD. I firmly believe I am really fortunate to share my life with her.

This dissertation is also dedicated to my holy God who led me here.

Contents

Abstract	iv
Acknowledgments.....	vi
Contents.....	ix
List of Tables.....	xiii
List of Figures	xv
Chapter 1 Introduction	1
1.1 Objective.....	1
1.2 Motivation.....	2
1.2.1 Geological scenarios for spatial modeling	2
1.2.2 Seismic inverse modeling for reservoir characterization	4
1.3 Problems and challenges.....	6
1.3.1 How can we include geological information and quantify its uncertainty?...6	
1.3.2 How can we integrate seismic data and geological scenarios into a reservoir model?	7
1.3.3 What is the most appropriate process to apply the proposed workflow in actual reservoir cases?	8
1.4 Chapter descriptions	8
1.5 References.....	11

Chapter 2 Modeling Geological Scenario Uncertainty from Seismic Data using Pattern Similarity	13
2.1 Abstract.....	13
2.2 Introduction.....	15
2.3 Methodology.....	16
2.3.1 Distance-based approximation for uncertainty estimation.....	16
2.3.2 Pattern capturing (1): Multiple-Point Histogram (MPH).....	18
2.3.3 Pattern capturing (2): Discrete Wavelet Transform (DWT)	22
2.3.4 Jensen-Shannon divergence for defining a distance	27
2.3.5 A pyramid of multiple resolution.....	28
2.4 Synthetic case study.....	30
2.5 Results.....	33
2.5.1 Case 1 (good quality seismic)	35
2.5.2 Case 2 (low quality seismic)	40
2.6 Conclusions.....	44
2.7 Acknowledgment	44
2.8 References.....	45
Chapter 3 A fast approximation for seismic inverse modeling: Adaptive Spatial Resampling.....	47
3.1 Abstract.....	47
3.2 Introduction.....	48
3.3 Methodology.....	54
3.3.1 Seismic inverse modeling in a Bayesian framework	54
3.3.2 Rejection sampling.....	56
3.3.3 Iterative spatial resampling	57
3.3.4 Adaptive spatial resampling.....	62

3.4 Application of the methodology in 2D	69
3.4.1 2D section examples	69
3.4.2 Sensitivity of parameters	73
3.4.3 Case study 1: 2D acoustic impedance inversion	75
3.4.4 Case study 2: 2D seismograms inversion.....	80
3.4.5 Case study 3: Identifying a facies not observed in wells	83
3.5 A 3D seismic inversion compared to sequential approach	85
3.6 Conclusions.....	90
3.7 Acknowledgment	91
3.8 Reference	91

Chapter 4 Field Application to a Channelized Turbidite Reservoir in Equatorial Guinea, West Africa.....96

4.1 Abstract.....	96
4.2 Introduction.....	97
4.3 Methodology.....	99
4.4 Field application	99
4.3.1 Seismic inversion in a Bayesian framework integrating seismic data and geological scenario uncertainty.....	99
4.4.1 Field introduction	101
4.4.2 Modeling a submarine canyon	105
4.5 Defining geological scenario uncertainty	110
4.5.1 Hierarchy of geological scenario uncertainty.....	110
4.5.2 Rockphysics uncertainty	111
4.5.3 Geometry uncertainty.....	116
4.5.4 Spatial distribution uncertainty	123
4.5.5 Forward simulation for seismic data prediction.....	125
4.6 Results.....	129
4.6.1 Modeling geological scenario uncertainty	129

4.6.2 Seismic inverse modeling conditioned to the geological scenario uncertainty	139
4.7 Conclusions.....	145
4.8 Acknowledgement	146
4.9 References.....	146
Chapter 5 Conclusion.....	150
5.1 Summary.....	150
5.2 Future implications and visions	152

List of Tables

Table 2. 1: Comparison of features in the MPH and CHP algorithm.....	21
Table 2. 2: Multiple (16) geological scenarios using different parameter settings.	32
Table 2. 3: Bayesian confusion matrix of MPH-based for Case 1	38
Table 2. 4: Bayesian confusion matrix of DWT-based for Case 1.....	38
Table 2. 5: Probability of each scenario given seismic data for the proposed approach and rejection sampling - Case 1	39
Table 2. 6: Bayesian confusion matrix of MPH-based for Case 2	42
Table 2. 7: Bayesian confusion matrix of DWT-based for Case 2.....	42
Table 2. 8: Probability of each scenario given seismic data for the approach and rejection sampling - Case 2.....	43
Table 3. 1: Comparison of input and output between the proposed inversion and sequential inversion.	87

Table 4. 1: Input geological parameters for generating object-based models spanning the range of geological scenarios.137

List of Figures

Figure 2. 1: A schematic diagram of process converting patterns in seismic data into multiple-point histogram.	20
Figure 2. 2: Examples of multiple point histograms (MPH, left) and cluster-based histogram of patterns (CHP, right) projected in a 2D MDS map. The result of CHP demonstrates the same or even better distinctions of each scenario in 2D while the computational time and cost is drastically less.	20
Figure 2. 3: Schematic diagram of 1D wavelet transform.....	25
Figure 2. 4: Schematic diagram of 2D wavelet transform.....	26
Figure 2. 5: A pyramid algorithm of multiple resolutions. Original image (top) is 150x80 pixels; the second image (middle) is a half of the original, and the smallest image (bottom) is one third of the first image. A pyramid algorithm considers these all in a distance matrix using weights.....	29
Figure 2. 6: Example of a few models (from scenario 1(top), 8(mid), and 11(bottom), left) and its forward simulated seismic data for high resolution (center) and low resolution (right).....	32

Figure 2. 7: A process of estimating $P(Sk|d)$. First, generate 50 prior models from each scenario and project it in MDS map. Next, create the probability density function by using adaptive kernel density estimation, and estimate the probability of data location from the multi-dimensional pdf.....34

Figure 2. 8: 2D representation of metric space (Case 1). The reference is represented by a black cross.37

Figure 2. 9: 2D representation of metric space (Case 2). The reference is represented by a black cross.41

Figure 3. 1: A flowchart of the McMC process with the Metropolis sampler. In the resampling step for selecting conditioning points, the proposed ASR algorithm adaptively resamples a subset from the lastly accepted model instead of random selection in ISR.....53

Figure 3. 2: Sketch of the Iterative Spatial Resampling method (ISR). An initial model m_1 is randomly sampled to obtain the subset, which is used as conditioning data for generating next model m_2 . m_2 displays similar local features as m_1 due to the constraints imposed by the conditioning data, but represents a different realization from the prior multi-point geostatistical model.....60

Figure 3. 3: The iteration of a Markov chain using ISR. Left: generated facies models; Right: the residual between seismic impedance and predicted impedance from the earth model in each step. This misfit is getting smaller with iterations.....61

Figure 3. 4: Sampling algorithm of the subset points in ASR. The seismic attribute used here is the inverted seismic impedance. Background green zone is the low residual points while both red and blue have higher error. In the residual error map, randomly sampled points (top, ISR) are located in both low and higher error

zone while adaptive sampling subsets (bottom, ASR) are located preferentially in low error zones.67

Figure 3. 5: Subset sampling algorithm for seismogram in the ASR. Since the seismogram is traces consisted of wiggles in travel time, directly subtracted variability can miss similar local feature. We used cross correlation coefficients between each trace for adaptive sampling of subset points. The location of a trace having high correlation coefficient with the corresponding data trace has more chance to be selected as subset points for conditioning the next iteration in the chain.68

Figure 3. 6: Left: The spatial distribution of the facies, P-wave velocities (V_p) and densities (ρ) are assumed as the reference. The filtered seismic band acoustic impedance and normal-incidence seismogram are at bottom left. Right: The data of two wells are given as above and the wells are located at CDP25 and CDP125, respectively. Training image for MPS is shown at the bottom of the right column.71

Figure 3. 7: Representation of the averages of ensembles of models. Left: (top) the reference facies and (bottom) averaged prior models. Right: (top) the E-type of rejection sampling results and (bottom) its variance.....72

Figure 3. 8: Performance assessment for testing different parameters. A dotted line is a Markov chain and a thick line is the average of five different chains. Top: adaptive resampling with 1% fraction of conditioning subset points performs slightly better than the other values, but this can be different depending on the problem; Bottom: The sensitivity of the number of traces is tested in 2D seismic section case. 8 traces case was an ideal setting in this study.74

Figure 3. 9: Representation of the averages of ensembles of models. Top: (first row) the E-type of rejection sampling results, ISR and ASR using acoustic impedance

as the observed seismic attribute; (second row) the variance of each algorithm, respectively. Bottom: (first row) the E-type of rejection sampler, ISR and ASR using seismogram section as the obtained data, and (second row) its variance. Within limited evaluations, ASR show similar E-type and variance map compared with the result of rejection sampling in both cases.77

Figure 3. 10: Adaptive spatial resampling (blue curves) and iterative spatial resampling (red curves) are compared for 5 Markov chains. The average of 5 chains for each case is shown as a thick line. ASR chains reach lower error zone more rapidly.78

Figure 3. 11: Right: After the burn-in period of the ISR chain, posterior models are sampled from 5 ISR (red dots) and ASR (blue dots) chains, respectively. Left: Each distribution of samples is shown as histogram. The distribution of ISR is slightly higher than the ASR. However, they are nearly overlapped and the median values are almost the same in histogram.79

Figure 3. 12: Multi-Dimensional Scaling (MDS) projection of all models using a Euclidean pixel-wise distance. The gray points are prior models and the red point is the reference. Blue dots are the posterior models by rejection sampling. ASR and ISR results are shown by green and magenta points, respectively.....82

Figure 3. 13: A case study for detecting oil sand distribution away from wells, when wells do not have any oil sand: Representation of the averages of ensembles of models. a) the reference three facies, b) a training image, and c) a bivariate pdf of each facies as a rockphysics model; d) the probability maps for oil sand facies obtained from the rejection sampler and e) the probability maps of the oil sand facies obtained from the posterior models sampled by ASR. Within relatively limited evaluations, ASR shows similar probability maps compared to the result of rejection sampler.84

Figure 3. 14: A 3D case study for comparing sequential inversion with the proposed simultaneous inversion. Left: (top) the reference of sand and shale facies and (bottom) a training image of the first layer of the Stanford VI reservoir; Right: we have (top) 4 wells located at (25,25), (25,75), (75,25), (75,75) and (bottom) acoustic impedance data as seismic data.....	88
Figure 3. 15: A result of the 3D case study. Left: A set of result of the proposed simultaneous inversion using ASR; (top) a sampled posterior, (middle) an averaged Etype map of 20 posterior models, and (bottom) the given acoustic impedance. Right: A set of result of the sequential inversion using soft data; (top) a sampled posterior, (middle) an averaged Etype map of 20 posterior models, and (bottom) the sand probability map used as soft data for geostatistical simulation (Castro et al., 2005).....	89
Figure 4. 1: Location of the study area (white rectangle) in offshore Equatorial Guinea, West Africa.....	103
Figure 4. 2: Present-day seafloor map interpreted from 3D seismic data.	104
Figure 4. 3: 2D seismic sections from Inline 1301 (left) and Xline 950 (right) for modeling the top (green line) and base (orange line) surfaces. Along the distinctive seismic reflections, both surfaces are interpreted.....	106
Figure 4. 4: A modeled submarine canyon. Top: The top and base surfaces are shown with their topography in TWT. Bottom: the seismic amplitudes (bottom picture) are extracted along the canyon boundary. Seismic reflections inside of the canyon show mixed responses of infill geobodies.	107
Figure 4. 5: A thickness map between the top and base surfaces. The contour map, colored in blue and purple, shows the target canyon from the right corner to the left center.....	108

Figure 4. 6: Thickness map in 3D (top) and 2D (bottom). The black rectangle is the target grid for modeling infill geological scenarios. 109

Figure 4. 7: A diagram of geological scenario uncertainty hierarchy. 111

Figure 4. 8: Multiple well log data from well X. Well X is located in the middle of the target grid and encounters oil sand while drilling. In well X, the target zone from 1050m to 1150m (100m deep) is marked by black lines. 113

Figure 4. 9: (a) Rockphysics relationship generated from well X in the target zone. Oilsand (marked by red), Carbonate-Cemented Oilsand (CCOilSand, marked by blue), and Shale (marked by magenta) facies are classified from well log information. (b) Rockphysics relationships, including Brinesand distribution (marked by green). Brinesand distribution is obtained via water sand below the oil-water-contact line in well X. This second rockphysics model is prepared for geological scenarios having brinesand distributions away from the well. 114

Figure 4. 10: Facies classification results from an inverted P-impedance cube using a Naïve Bayes classifier. Depending on the rockphysics models, facies classification results and their proportions can be very different. These classification results can be used as a guideline for the proportion of each facies. 119

Figure 4. 11: (a) An example of the Earth model based on rockphysics model 1. The minimum values from each uniform distribution are applied for the example: 10% proportion for oilsand and 3% proportion for carbonate-cemented oilsand. (b) An example of the Earth model based on rockphysics model 2. The maximum values from a range of parameters are applied to generate the model: 25% proportion for oilsand. 25% proportion for brine sand, and 10% proportion for carbonate-cemented oil sand. 120

- Figure 4. 12: (a) Examples of the width variation. The left model is made from a 125m wide sample while the right one is generated from with 250m as the width value. The both examples used the same Width/Height (W/H) ratio as 1. Since the 2D slice is vertically 25 times exaggerated, the W/H ratio 1 means 25m in horizontal and 1m in vertical. (b) Examples of the width/height ratio difference. Within the same width (250m wide), the left model uses 0.5 (5m deep) and right model uses 1.5 (15m deep) as the w/h ratio. 121
- Figure 4. 13: A set of sinuosity variations from wavelengths 200 to 50. Note the wavelength value means the number of voxels between two peaks. 122
- Figure 4. 14: Spatial distribution uncertainty is modeled as a wide variety of staking patterns. In this dissertation, we set up three stacking patterns for a series of turbidite channels: (a) isolated, (b) multi-story, and (c) multi-lateral. 124
- Figure 4. 15: A schematic diagram of forward simulation for seismic responses corresponding to the geological scenarios. 126
- Figure 4. 16: Well-tied wavelet extraction in HRS software. A source wavelet is extracted in the software, and the predicted seismograms using the extracted wavelet (blue and red) and actual seismic section (black) are well matched. 127
- Figure 4. 17: Well-tied wavelet extraction in HRS software. Among the preset wavelets, Ricker wavelet shows the best match. 128
- Figure 4. 18: Some examples of various geological scenarios. Compared to (a), (d) scenario contains smaller channel proportion with only two sand facies such as oil-sand (green) and carbonated cemented oil-sand (red). Stacking pattern in scenario (d) is multi-story (vertically stacked) while channels in scenario (a) spread out widely. We can see a variety of channel dimension from scenario (d),

(e), and (f). A range of sinuosity is also shown in scenario (b), (c) and (f). Scenario (b) is less sinuous while scenario (c) has meandering channels. 132

Figure 4. 19: A schematic diagram to calculate pairwise distances between the obtained seismic data and the forward simulated geological scenarios. Here we do not compare the local amplitude trace by trace but we globally compare the patterns and count the frequency of each pattern in seismic data. 133

Figure 4. 20: A MDS projection of Cluster-based Histogram of Patterns (CHP) results using 450 models to obtain seismic data. The data (marked with a black cross) is located in the middle of blue clouds, and thus we can infer that rockphysics model 2 is more likely than rockphysics model 1 in the target grid of the case study. 134

Figure 4. 21: To discover the most promising geological setting, close samples are selected. The models are selected by their distance from the data in MDS map (marked in red). 135

Figure 4. 22: A cumulative frequency of histogram for the CHP result. The histograms of patterns are closer, the cumulative functions are more similar each other. All prior models are plotted as black curves and the selected model in MDS map are marked by red curves. The data (marked by blue) shows very similar cumulative frequency of histogram with the red curves. 136

Figure 4. 23: Most probable geological scenarios and its geological parameters. Based on the MDS projection, all models from rockphysics model 2 are rejected, while a multi-story stacking pattern is promising in this study area. Also, we can observe that the range of proportion, width, and W/H ratio are relatively narrower than the initial input distribution. 137

Figure 4. 24: Re-generated models based on the three nearest geological scenarios and its geological parameters. Based on the MDS projection and Kernel-Smoothing

density estimation, geological scenario 2 is more likely among the selected scenarios.....	138
Figure 4. 25: A functional estimation of Mean Absolute Error(MAE) between the given seismic data and predicted one. With iterations, a Markov chain formed by ASR is getting closer to the posterior distribution.	141
Figure 4. 26: Correlation coefficients after the burn-in period. To sample independent posteriors which are not correlated with a previous sample, we tested cross-correlation between models in a Markov chain after the burn-in period. After 10 iterations later, cross-correlation is almost disappeared (correlation coefficient is 0.14) and we setup this as a lag distance to sample posteriors.....	142
Figure 4. 27: (a) A sampled posterior from M-ASR. (b) A transparent image of the posterior and it shows all sand channel distributions. (c) Conditioned to geological scenarios and given seismic data, oil sand distribution (cyan) and carbonate cemented oil sand distribution (yellow) are predicted.....	143
Figure 4. 28: An Ensemble average map of 20 posterior samples.	143
Figure 4. 29: 2D seismic section matching. (a) A 2D seismic section from the obtained seismic data, and (b) the forward simulated seismic section based on a facies model shown in (d). (c) Cross-correlation between (a) and (b) shows overall traces are matched well.	144

Chapter 1

Introduction

“Good tests kill flawed theories; we remain alive to guess again.”

- *Karl Popper*

1.1 Objective

The main objective of this dissertation is to develop a workflow for quantitative reservoir characterization from seismic data and geological information. This general objective entails three specific goals: 1) to model geological scenario uncertainty from seismic data, in order to identify more likely geological scenarios among the all available geological possibilities; 2) to discover a posterior distribution as a set of models, constrained to seismic data within time and cost; and 3) to apply the proposed

workflow in an actual dataset (a turbidite reservoir in West Africa) to verify its applicability. The motivations and current issues for each of these specific objectives are described below.

1.2 Motivation

1.2.1 Geological scenarios for spatial modeling

Modeling the subsurface reservoir is a highly uncertain process due to the scarcity of data and to geological heterogeneity. Uncertainty is not only related to errors in measurement or data processing: even if data were perfectly measured, major sources of uncertainty still exist in building the Earth models. These sources include structural uncertainty, geological uncertainty, spatial uncertainty, physical uncertainty of a forward model, data interpretation uncertainty, and so forth (Caers, 2011). Since we cannot deal with all these sources at the same time, we have to address specific uncertainty depending on each model's application.

For example, say some petroleum engineers need to make a decision about further exploitation in an exploration field with few wells and seismic data. In this situation, the typical key issues would be modeling the subsurface reservoir and quantifying the uncertainty. If the reservoir engineers want to know the original oil in place, they would need a spatial facies model or reservoir parameters such as net-to-gross or porosity. If they need additional drilling well positions, then the analysis should focus

on reservoir connectivity. Thus, spatial uncertainty is one of most important keys for reservoir modeling.

Spatial modeling is an old but still difficult issue in geostatistics. Various techniques, notably the process-based, object-based, and geostatistical sequential simulation techniques, have been suggested and studied (Caers, 2005). Process-based algorithms make the most geologically realistic models, but they are slow and make it hard to condition the data, because the model is generated by calculating the governing equations and boundary conditions. On the other hand, variogram-based sequential simulations are fast and easy for honoring data, but cannot capture geological reality. Multiple point geostatistics (MPS) algorithms have been widely applied to generate geologically realistic models by using training images. Training images work like a variogram in two-point geostatistics. Since the training image is based on geological observation or analogy analysis of a nearby outcrop, it can represent one possible geological scenario for the reservoir. Due to the important role of these training images in MPS, another issue is linked to geological uncertainty and how to obtain correct geological scenarios as training images.

Geological scenario uncertainty is created by uncertain geological observations or ignorance about the real Earth. There are many ongoing research efforts to develop MPS algorithms capable of handling more realistic training images, and for more practical aspects of defining and selecting appropriate training images based on geology. Since geological interpretation is based on little data and the subjective

decision of geologists, a training image may be a major source of uncertainty. Caumon (2004) reported that the choice of geological scenario has a stronger impact in the assessment of reservoir uncertainty than the stochastically modeled property distribution. Suzuki et al. (2006) suggested using multiple possible geological scenarios with multiple training images, to reduce geological uncertainty by means of production data. However, the question still remains how to modify these multiple geological scenarios to quantify the uncertainty of models.

1.2.2 Seismic inverse modeling for reservoir characterization

Another critical issue we treat in this dissertation is the uncertainty of seismic inversion. Since this uncertainty is related both to the physical uncertainty in the forward model and to uncertainty in data interpretation, integrating seismic data into reservoir models is a significant challenge. Seismic measurements also have larger scales of resolution than well data, so reconciling multi-scale data for spatial modeling of reservoir properties is necessary. Seismic inversion has been studied widely and applied to several final goals, such as seismic impedance inversion or seismic inversion for reservoir property. Recent seismic inversion schemes successfully incorporate these data by using rock physics information for reservoir property, and by applying geostatistical models for spatial continuity. Gonzalez et al. (2008) introduced a seismic inversion technique in a Bayesian framework, combining multiple points geostatistics (MPS) and rock physics. They generated multiple realizations of reservoir

facies and saturations, conditioned to seismic and well data. MPS was used to characterize the prior geologic information, and conditional rock physics linked between reservoir properties and elastic properties. Their method provided multiple realizations, all consistent with the expected geology, well-log and seismic data, and local rock-physics transformations. However, this workflow does not produce samples of the posterior probability density function, but rather generates multiple optimized models.

To quantify the uncertainty of the models with given data, producing posterior samples is important. These posterior samples represent all models which honor all the obtained data and exist in prior distribution. Regardless of the importance and advantages of sampling, most of the seismic inversion methods apply a deterministic optimization approach because it requires fewer computations and less time (Doyen, 2007, Sams and Saussus, 2008). Reducing CPU demand for multiple realizations of any geostatistical inversion scheme is still one of the biggest issues in this area. To apply this inversion workflow to the real field data, we have to overcome several limitations of previous methods.

Since the conventional MPS algorithms such as SNESIM or SIMPAT store all data events from the training image (Strebelle, 2000; Arpat, 2005), computing load is dramatically increased according to the size of the template and the number of facies. Hence, it is slow and not applicable for complex structures. For instance, it takes tremendous time to generate thousands of prior models in 3D, containing several

million gridblocks. On the other hand, in posterior sampling methods, the rejection sampling method (Tarantola, 2005) in a Bayesian frame is the only one to represent perfect posterior probability density function (PDF). However, since it requires a large number of evaluations of the forward model, rejection sampling is inefficient and not suitable to the seismic inversion. A key issue for practicality is to generate prior models and to sample the posterior, honoring obtained data in limited time and at a reasonable cost.

The objective of this Ph.D. research is to develop a workflow for producing posterior samples of reservoir models consistent with geology, well logs, and seismic data within time and cost. Relevant issues and problems are sequentially included in the workflow, which is then applied to real field tasks.

1.3 Problems and challenges

1.3.1 How can we include geological information and quantify its uncertainty?

First, all available geological prior information should be grouped into geological scenarios. These multiple geological scenarios can be used as multiple training images in a reservoir modeling workflow. However the most important challenge is to find more promising scenarios and quantify the geological scenarios' uncertainty. Even though geologists have successfully built possible geological models, they are very uncertain, and it's hard to quantify that uncertainty. To address the uncertainty of

multiple geological scenarios, we have to test these scenarios with the given data. In this dissertation, we propose a workflow as the following process. Starting with the same probability (or the probability given by geologists), we can identify more likely scenarios and less likely ones by comparing the pattern similarity of seismic data. Then we use these probabilities to sample the posterior PDF constrained in multiple geological scenarios. Identifying each geological scenario in metric space, and estimating the probability of each scenario given particular data, help to quantify the geological scenario uncertainty. This detailed methodology is discussed in Chapter 2.

1.3.2 How can we integrate seismic data and geological scenarios into a reservoir model?

Secondly, combining MPS and seismic data in Bayesian inversion will be studied with some geological scenarios and forward simulations for seismic data. Due to various practical issues such as the complexity of seismic data and the computational inefficiency, this is not yet well established, especially for actual 3-D field datasets. To go from generating thousands of prior models to sampling the posterior, a faster and more computationally efficient algorithm is necessary. At the same time, these methods should not violate Bayes' rule. Thus, this dissertation proposes a fast approximation algorithm for sampling the posterior distribution of the Earth models, while keeping a range of uncertainty and practical applicability.

1.3.3 What is the most appropriate process to apply the proposed workflow in actual reservoir cases?

Lastly, the application process in an actual reservoir will be discussed. A field in early stage has very limited data such as little well data, seismic data, and some geological observations. Accordingly, the proposed workflow can be a guideline for a full package, from selecting geological scenarios to suggesting a set of models conditioned to well data, seismic data and geological observations for decision makers. The case study, applied in a turbidite reservoir in West Africa, can be a sample recipe of the workflow. It contains a well log study, rock physics modeling, a forward simulation for generating seismic responses, and object-based prior modeling. Based on distance-based pattern similarity results, promising geological scenarios will be selected as training images for seismic inverse modeling. Then Metropolis sampler can sample a posterior distribution consistent with all available data and geological scenarios.

1.4 Chapter descriptions

This thesis consists of five chapters, including this introduction. The chapters are linked together and represent a possible solution according to the problems introduced in this chapter.

Chapter 2 introduces a workflow to model geological scenario uncertainty from

seismic data, using pattern similarity algorithms. We propose to assess the consistency of all available geologic scenarios with the observed data, by defining a pattern similarity between seismic data and forward simulated data. To estimate this probability, we generate a set of models from each scenario, and calculate distances between forward modeled seismic data and actual data. The distance between two seismic responses is defined as the difference in the frequency of their patterns. We use two different pattern-based techniques, namely Multiple Points Histogram (MPH) and Discrete Wavelet Transform (DWT). Next we apply the Jensen-Shannon (JS) divergence to evaluate the distance between the frequency distributions of two images. The resulting distance matrix is projected in multi-dimensional scaling (MDS) space to estimate the likelihood distributions of each scenario given the data. The evaluated likelihood represents the probability of each scenario, so low likelihood scenarios can be eliminated. This chapter was co-worked with Céline Scheidt, Jef Caers, and Tapan Mukerji, and it was presented at the International Association for Mathematical Geosciences conference (September 2-6, 2013), in Madrid, Spain.

Chapter 3 presents an adaptive spatial resampling (ASR) algorithm as a fast approximation for seismic inverse modeling. As a variant of the Markov Chain Monte Carlo (MCMC) method, the Metropolis-ASR performs an approximate sampling of the posterior distribution, conditioned to the seismic data. In this chapter, we introduce Direct Sampling (DS) for generating a realization in a Markov chain, and the ASR algorithm to form a Markov chain for sampling posteriors. The Iterative Spatial Resampling (ISR) algorithm perturbs realizations of a spatially dependent variable

while preserving its spatial structure, by conditioning to subset points. However, in most practical applications, when the subset conditioning points are selected at random, the algorithm can get stuck for a very long time in a non-optimal local minimum. Thus we improve the efficiency of ISR by adaptive resampling. This chapter was co-worked with Tapan Mukerji, and Gregoire Mariethoz, and it was presented at The SEG International Exposition and 82th Annual Meeting (November 5-9, 2012) in Las Vegas, Nevada. This chapter has been submitted to *Mathematical Geosciences* (under review).

Chapter 4 provides a practical recipe for applying the proposed workflow into actual reservoir modeling. A turbidite reservoir in Equatorial Guinea, West Africa is used for verification of the workflow, and the study is started from the beginning stage of reservoir modeling. Based on a few well logs from one well, rockphysics relationships which links reservoir property (facies) and elastic properties (P-velocity and density) is established, and it is used for seismic forward simulation. After modeling a target canyon in seismic resolution, the process of modeling geological scenarios is performed to find more important geological parameters by sensitivity analysis, and to assess more promising scenarios. With the final results reservoir modelers can provide a set of models constrained to well data, seismic data, and geological scenario uncertainty. This chapter has been submitted for presentation at the International Association for Mathematical Geosciences (October 17-20, 2014), in New Delhi, India.

1.5 References

- Arpat, B. G., 2005. Sequential simulation with patterns: Ph.D. dissertation. Stanford University.
- Caers, J., 2011, Modeling uncertainty in the Earth sciences, Wiley-Blackwell.
- Caumon, G., Lepage, F., Sword, C. H., and Mallet J., 2004, Building and editing a sealed geological model, *Mathematical Geology* 36 (4): 405-424.
- Doyen, P. M., 2007. Seismic reservoir characterization: An earth modeling perspective. EAGE Publications.
- Gonzalez, E. F., Mukerji, T., and Mavko, G., 2008. Seismic inversion combining rock physics and multiple-point geostatistics. *Geophysics*, 73, no. 1, R11-R21.
- Sams, M., and Saussus, D., 2008, Comparison of uncertainty estimates from deterministic and geostatistical inversion: 78th Annual International Meeting, SEG, Expanded Abstracts, 1486–1490.
- Strebelle, S., 2002, Conditional simulation of complex geological structures using Multiple-Point Statistics, *Mathematical Geology*, 34 (1): 1-22, doi:10.1023/A:1014009426274.
- Suzuki, S. and Caers, J., 2006, History matching with an uncertain geological scenario, Paper SPE 102154 presented at the SPE Annual Technical Conference and Exhibition, San Antonio, Texas, USA, 24-27 September. doi:10.2118/102154-M.

Tarantola, A., 2005. Inverse problem theory and methods for model parameter estimation. SIAM.

Chapter 2

Modeling Geological Scenario Uncertainty from Seismic Data using Pattern Similarity

“Essentially, all models are wrong, but some are useful.”

- *George E. P. Box*

2.1 Abstract

Traditional seismic inversion approaches have focused on reducing error between data and model within a fixed geological scenario. The problem with this approach is that either uncertainty related to geological interpretation is ignored or that inversion

needs to be repeated for each scenario. In this chapter we propose to first assess the consistency of all available geologic scenarios with the observed data by defining a pattern similarity between seismic data and forward simulated data. The considered scenarios include geologic variables (such as facies proportions, geobody size, and stacking patterns), as well as rock physics relationships relating rock properties to seismic data. We develop a pattern-based procedure to estimate the probability of each scenario given seismic data. Low probability scenarios are rejected. To estimate this probability, we generate a set of models from each scenario, and calculate distances between forward modeled seismic data and actual data. The distance between two seismic responses is defined as the difference in frequency of patterns found in the images. We use two different pattern-based techniques, namely Multiple Points Histogram (MPH) and Discrete Wavelet Transform (DWT). Next we apply the Jensen-Shannon (JS) divergence to evaluate the distance between the frequency distributions of two images (MPH frequencies and wavelet coefficients frequencies in each sub-band). The resulting distance matrix can be projected in multi-dimensional scaling (MDS) space to estimate the likelihood distributions of each scenario given the data. The likelihood is evaluated using an adaptive kernel smoothing technique. The proposed workflow is applied on 2D seismic section with 16 geologic scenarios, and verified by success rates of a Bayesian confusion matrix and a comparison with rejection sampler.

2.2 Introduction

Most current approaches of seismic inversion aim to reduce error between the obtained data and predicted models, and use a set of matched models for forecasting geological heterogeneity and future reservoir performance. However, since these inversion approaches are limited within a fixed geological scenario, it cannot handle larger sources of geological uncertainty. Finding the best fit models with the given data does not guarantee an accurate future prediction. Even worse, we often have to discard the previously matched models due to discrepancy with newly obtained data. The discrepancy can be caused by too narrow range of uncertainty as the result of an incorrect geological scenario. If our geological scenario is completely wrong, the seismic inversion is extremely inefficient. Thus, to model multiple geological scenario uncertainty is an essential pre-requisite task. In more realistic geomodeling, we have to consider uncertainty in various sources of geological variables such as facies proportion, geobody size, stacking patterns, number of faults, kinds of faults, rockphysics relationships, fluid-rock type and so forth. Then a main challenge is which scenarios are more likely or less likely and how to screen all the available scenarios.

We develop a pattern-based procedure for estimating the probability of each scenario from the obtained seismic data. To estimate this probability, we generate a set of models from each scenario, and calculate differences between forward simulated seismic data and actual data. We define the differences between the responses as

distances in metric space. First, we applied pattern capturing algorithms such as Multiple Points Histogram (MPH) and Discrete Wavelet Transform (DWT) analysis for converting seismic data as a histogram of patterns. Next, JS divergence algorithm is applied for calculating the distance between two frequency distributions. Lastly the distances are projected in Multi-Dimensional Scaling (MDS, Borg & Groenen, 1997; Caers, 2011) map for estimating probability of each scenario given data. As the result, we can quantify geological scenario uncertainty and low probability scenarios are rejected. The proposed workflow is applied on 2D seismic section with 16 scenarios, and two different pattern capturing algorithms (MPH and DWT) are tested. The proposed workflow is verified by success rates of a Bayesian confusion matrix and a comparison with rejection sampler.

2.3 Methodology

2.3.1 Distance-based approximation for uncertainty estimation

If we have several discrete parameters to explain geological heterogeneity, we can propagate it as a set of multiple scenarios in a Bayesian framework as:

$$P(m_{res}, S|d) = \sum_k P(m_{res}|S_k, d) P(S_k|d) \quad (2.1)$$

where S_k is the k -th scenario, $P(S_k|d)$ is the posterior probability of each geological scenario given data, $P(m_{res}|S_k, d)$ is the data-likelihood given the k -th

scenario and models, and final posterior probability is calculated by summing up the all likelihood values depending on each scenario. Here, $P(S_k|d)$ means that each scenario has different probability and we can calculate this as following equation (2.2).

$$P(S_k|d) = \frac{P(d|S_k)P(S_k)}{\sum_k P(d|S_k)P(S_k)} \quad (2.2)$$

where $P(S_k)$ is the prior probability and the values are assessed by geologists. If it is hard to estimate, we can assume that $P(S_k)$ is equiprobable. To estimate $P(S_k|d)$, we propose a distance-based approximation method. It assumes the density function $f(d|S_k)$ can be approximated by density of samples in MDS map for each scenario (Park et al., 2013). Thus,

$$P(d|S_k) \approx f(d|S_k) \approx f(X|S_k) \quad (2.3)$$

where f is probability density function in MDS map, and X is the projection of the observed data indicating a location on the MDS map. The dots in MDS map represent forward simulated seismic responses from each model. From the dots of each scenario, we generate probability density function of the scenario k , and use the pdf for estimating $f(X|S_k)$. Since seismic data is 2D or 3D image response, a big challenge is to define distances between the seismic images. Traditional Euclidean distance is

not appropriate for our goal because what we are interested in is patterns similarity or dissimilarity of seismic response influenced by various geologic parameters not the specific locations of geobody in seismic data. Therefore the key issues are how to capture the patterns in seismic responses and how to define its differences. To do this we applied pattern similarity algorithms consisted of MPH or DWT for comparing patterns in seismic responses, and Jensen-Shannon divergence for defining a distance between two seismic responses.

2.3.2 Pattern capturing (1): Multiple-Point Histogram (MPH)

To compare seismic responses as pattern similarity, not residual error between two responses, first we have to define similarity itself. We propose to convert seismic data into a histogram of patterns by the multiple-point histogram algorithm (MPH, Deutsch and Gringarten, 2000; Lange et al., 2012). Figure 2.1 explains the algorithm schematically. We have a thresholded seismic image (middle of Figure 2.1) generated from a 2D seismic section data (top of Figure 2.1). Then the image has three categorical variables such as positive amplitude, negative amplitude, and zero. A 2x2 template in 2D makes 3^4 (=6,561) possible data-event configuration. Each data-event configuration is located in X coordinate and its frequency is recorded in Y coordinate to build a histogram (right of Figure 2.1). Since each histogram counts frequency of all patterns, similarity of histogram accounts for existing analogous patterns between two seismic responses.

However, the current MPH algorithm only can handle categorical variables due to the computer memory limits. Even though it uses only three categories, the computational issues are problematic when the size of template gets larger. For example, in Figure 2.2, 5x3 in 2D template has 14,348,907 data-event possibilities. Thus the applicability of MPH algorithm is circumscribed by a small template.

Instead of using all patterns, we cluster the patterns into groups using the methodology described in Honarkhah and Caers (2010). For each cluster, we record the number of patterns and calculate the prototype, and it represents each cluster. The prototype can be a mean of the patterns within that cluster or a medoid pattern. It can dramatically reduce the memory burden as shown in Table 2.1. The 14,348,907 patterns captured by MPH are classified as 602 prototypes by Cluster-based Histogram of Patterns (CHP). In this dissertation, first we do the clustering and generate prototypes based on the obtained seismic data. Then we classify the prior models' patterns by calculating distances with the data prototypes, and simply assign the pattern to the closets prototype. By repeating the process, we obtain the same number of clusters as the prototype patterns for all prior models from each scenario and the obtained data. Since the cluster-based histogram of patterns (CHP) lists relatively a small number of prototypes and their frequencies, instead of recording all patterns, it drastically reduce computing time and cost. Compared to the MPH of the full patterns, Figure 2.2 demonstrates that CHP leads to the same distinctions of each scenario in 2D MDS map. Table 2.1 summarizes the advantages of the CHP based on an example of the size of template, 5-by-3.

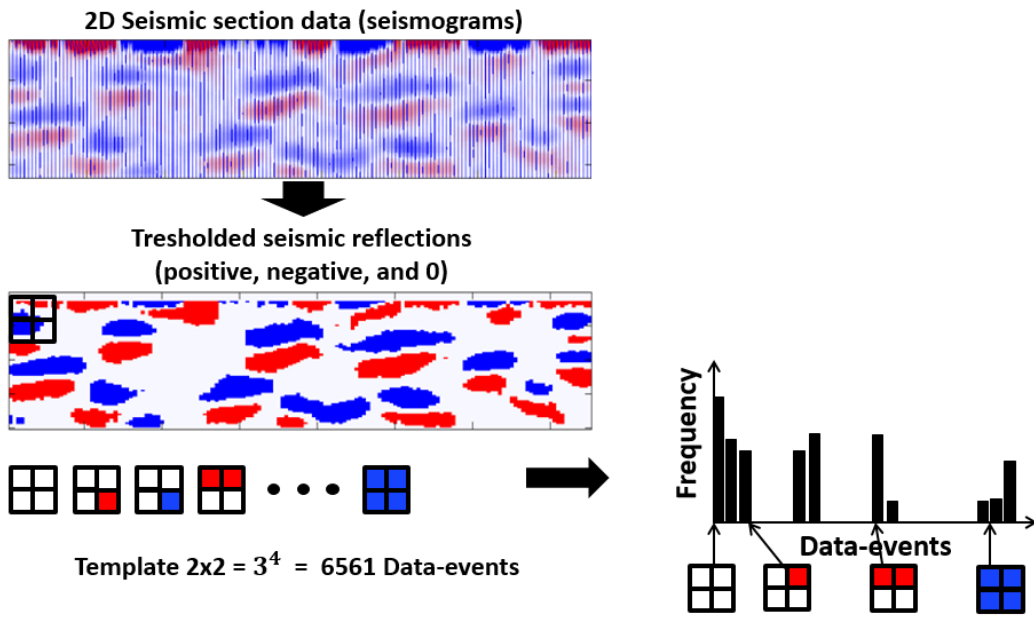


Figure 2. 1: A schematic diagram of process converting patterns in seismic data into multiple-point histogram.

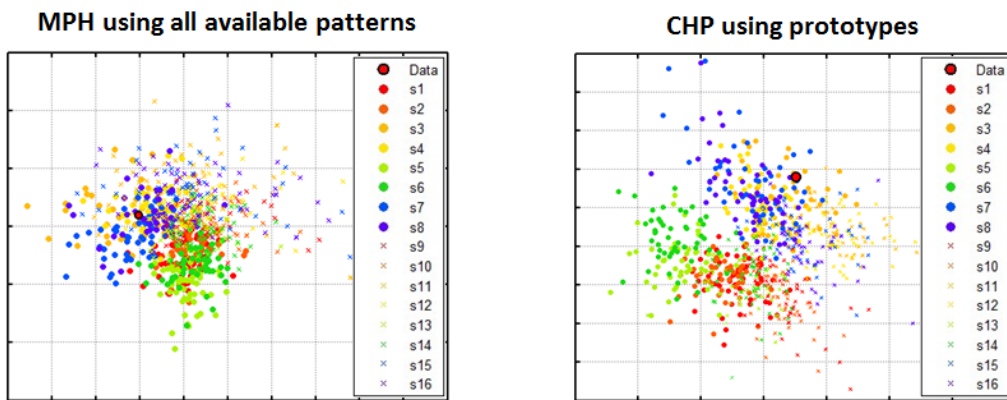


Figure 2. 2: Examples of multiple point histograms (MPH, left) and cluster-based histogram of patterns (CHP, right) projected in a 2D MDS map. The result of CHP demonstrates the same or even better distinctions of each scenario in 2D while the computational time and cost is drastically less.

Table 2. 1: Comparison of features in the MPH and CHP algorithm

	MPH	CHP
Variables	Categorical only	Categorical or continuous
Patterns in template size 5x3	14,348,907 patterns	602 prototypes
Time for 800 models in 3 layers*	10 hours	15 minutes

(*for computing, Matlab runs in a machine of 3.3GHz (4 CPUs) and 16GB RAM)

2.3.3 Pattern capturing (2): Discrete Wavelet Transform (DWT)

A wavelet is a mathematical function that is used mostly for digital signal processing and image compression or denoising (Chui, 1992; Daubechies, 1992; Mallat, 1999). In reservoir engineering, Sahni and Horne (2006) used wavelet transform of the parameter distribution (permeability) to generate a set of reservoir models for history matching. Awotunde and Horne (2012) used one-dimensional wavelet decomposition of production data for parameter estimation.

Wavelet transformation decomposes a signal $f(x)$ as a combination of two families of basis functions called wavelets (represented by Ψ and ϕ). Wavelets can be expressed at different scales and different frequencies by translation and dilatation of Ψ (mother wavelet) and ϕ (scaling function):

$$\psi_{s,p}(x) = 2^{-s/2} \psi(2^{-s}x - p) \quad \text{and} \quad \phi_{s,p}(x) = 2^{-s/2} \phi(2^{-s}x - p) \quad (2.4)$$

where p denotes the position of the wavelet and s the scale (wavelet width). A signal $f(x)$ can then be decomposed as

$$f(x) = \sum_s \sum_p [a_{sp} \phi_{s,p}(x) + c_{sp} \psi_{s,p}(x)] \quad (2.5)$$

with a_{sp} and c_{sp} the coefficients after wavelet transformation. The coefficients concentrate on some critical values; in general, most of the coefficients are zero.

The scaling function $\phi_{s,p}(x)$ is associated to a low-pass filter, or in other words as an averaging filter. The wavelet function $\psi_{s,p}(x)$ is associated to a high-pass filter, which extract details of the signal.

In practice, one-dimensional DWT consists in splitting the signal into two parts, by passing the subsequently subsampled by two (according to Nyquist's rule). The low pass filter generates signal through a low-pass ($\phi_{s,p}(x)$) and a high-pass ($\psi_{s,p}(x)$) filter. The outputs are the approximation coefficients A_1 and the high-pass filter generates the so-called details coefficients C_1 . The procedure can then be repeated using the resulting approximation coefficients A_1 . A multi-level pyramid can then be obtained by applying the same procedure to the approximation coefficients at lower levels (l), resulting in coefficient A_l, C_l . Note that the number of coefficients is the same as the number of samples n of the signal. As a consequence, A_1 and C_1 contain both $n/2$ coefficients, A_2 and C_2 contains $n/4$ coefficients and so on.

A schematic diagram illustrating the principle of the 1D wavelet transform is shown in Figure 2.3.

Two-dimensional wavelet transforms are useful to analyze images (or two-dimensional datasets). Two-dimensional wavelets are an extension of one-

dimensional wavelets. They are composed of four different functions: a two – variable scaling function ($\phi(x,y)$) and three two-variables wavelet functions ($\psi^H(x,y)$, $\psi^V(x,y)$ and $\psi^D(x,y)$):

$$\phi_{s,p,q}(x,y) = 2^{-s/2} \phi(2^{-s}x - p, 2^{-s}y - q) \quad (2.6)$$

$$\psi_{s,p,q}^i(x,y) = 2^{-s/2} \psi^i(2^{-s}x - p, 2^{-s}y - q), \quad i = \{H, V, D\} \quad (2.7)$$

The principle is to apply a one-dimensional wavelet transform to each row of the original image, subsample the rows by 2 and then apply a one-dimensional wavelet transform to each column of the resulting matrix and subsample the columns by 2. Thus Two-dimensional wavelet transform generates four sub-images of coefficients: A1 (the approximation coefficients), H1 (horizontal), V1 (vertical), and D1 (diagonal) details coefficients, each of size $N_x/2 \times N_y/2$ for an initial image of size $N_x \times N_y$. A schematic diagram representing a 2D wavelet transform is illustrated in Figure 2.4.

In this dissertation, we use the Haar wavelet. The Haar wavelet is the first and also simplest wavelet to be proposed (Chui, 1992). The Haar wavelet's mother function can be described as (in 1D):

$$\psi(x) = \begin{cases} 1 & 0 \leq x < 1/2 \\ -1 & 1/2 \leq x < 1 \\ 0 & \text{otherwise} \end{cases} \quad (2.8)$$

Its scaling function is defined as:

$$\phi(x) = \begin{cases} 1 & 0 \leq x < 1 \\ 0 & \text{otherwise} \end{cases} \quad (2.9)$$

Other types of wavelets (Daubechies, Coiflets, Discrete Meyer, etc.) have been considered for this study, the Haar wavelet resulted in a better differentiation of the different scenarios. In addition, the number of levels of wavelet decomposition has been studied in the application below. In this case, a 2-level wavelet decomposition seems to be the most appropriate ($L=2$).

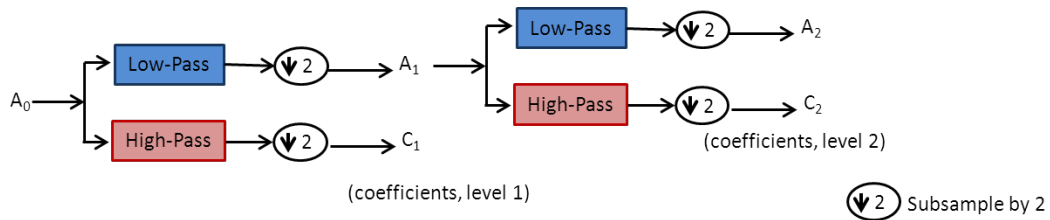


Figure 2. 3: Schematic diagram of 1D wavelet transform.

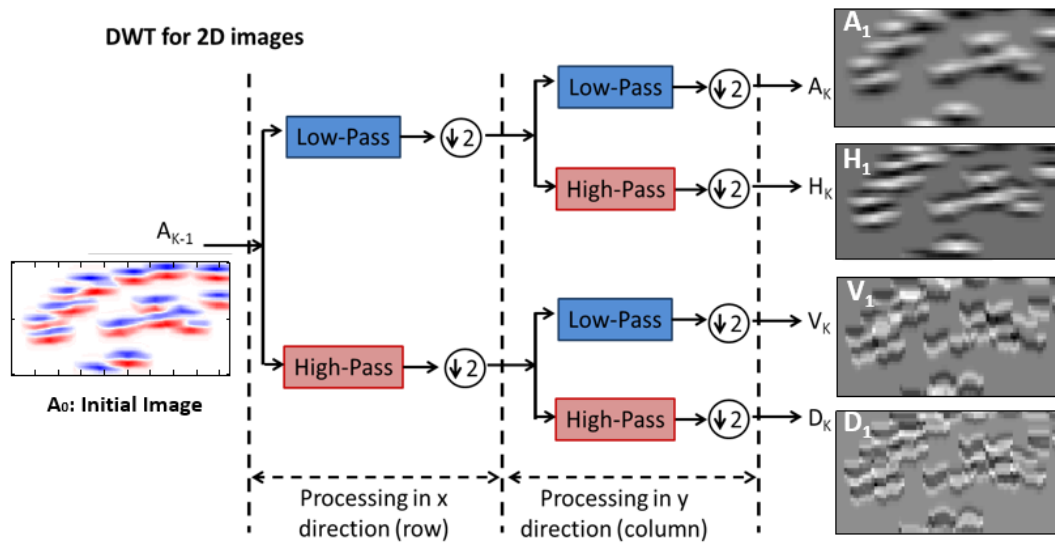


Figure 2. 4: Schematic diagram of 2D wavelet transform.

2.3.4 Jensen-Shannon divergence for defining a distance

Once the histograms of patterns (or wavelet coefficients) are computed by MPH and DWT for all seismic responses, the Jensen-Shannon (JS) divergence is used to evaluate the distance (Kullback and Leibler, 1951; Kullback, 1983). The JS divergence estimates the difference between two frequency distributions h_i and h_j in Equation (2.10) (Cover and Thomas, 1991; Endres and Schindelin, 2003).

$$d_{JS}(h_i, h_j) = \frac{1}{2} \sum_i h_i \log \left(\frac{h_i}{h_j} \right) + \frac{1}{2} \sum_i h_j \log \left(\frac{h_j}{h_i} \right) \quad (2.10)$$

Other statistical measures of difference such as the chi-squared distance can be used but such distance is not robust in the context of MPHs (or CHPs) whose frequencies vary widely. Given L realizations of each scenario k and the given data, the distance matrix D is represented by the following equation (2.11).

$$D = \{d_{ij}\}, \quad d_{ij} = d_{JS}(h_i, h_j) \quad \forall i, j = 1, \dots, (L \times k + 1) \quad (2.11)$$

The calculated distance matrix is projected in MDS map for generating a probability density function of each scenario and estimating the probability of scenario given data. The workflow used in this study to estimate the posterior probability of

each scenario given the data is presented in Park et al. 2013.

2.3.5 A pyramid of multiple resolution

We also consider that pattern variations occur in multiple scales. For this purpose, we build a pyramid of multiple resolution views (similar to Heeger & Bergen, 1999) of the same realization. Figure 2.5 shows an example setting in this dissertation, and we used a pyramid of 3 layers. The original image (top of Figure 2.5) is 150x80 pixels; the second image (middle of Figure 2.5) is a half of the original and it is 75x40 pixels. The smallest image (bottom of Figure 2.5) is one third of the first image. To resize the original image, bicubic interpolation is applied. The output pixel value is a weighted average of pixels in the nearest 4 by 4 neighborhood. Next we applied pattern capturing algorithms to convert seismic responses of each layer into histograms, and JS divergence to calculate distances between the converted histograms. A pyramid algorithm considers all of these three layers' distances in a distance matrix using weights in following equation (2.12).

$$D_{pyramid} = \sum_{l=1}^n \frac{1}{l^2} D_{MR_l} \quad \forall n = \# \text{ of multiple resolution} \quad (2.12)$$

where, D_{MR} is the distance matrix of size $(L \times k+1) \times (L \times k+1)$, L realizations of k -th scenario and the given data.

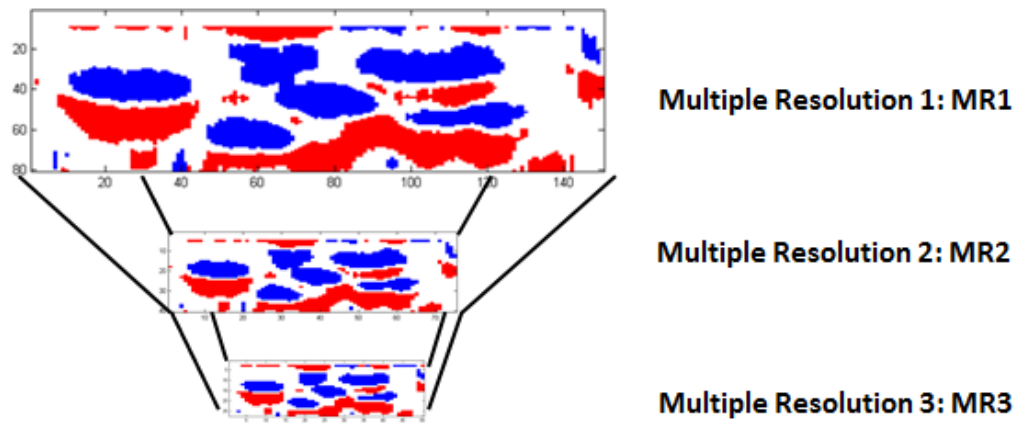


Figure 2. 5: A pyramid algorithm of multiple resolutions. Original image (top) is 150x80 pixels; the second image (middle) is a half of the original, and the smallest image (bottom) is one third of the first image. A pyramid algorithm considers these all in a distance matrix using weights.

2.4 Synthetic case study

To validate the proposed workflow we prepared the synthetic 2D facies case with two different seismic resolution. The reference facies model is a sand-shale channel system with 80 cells in the vertical (z) direction ($dz = 1\text{m}$) and 150 cells in x ($dx = 12.5\text{m}$). To model geological scenario uncertainty, 16 distinct channels scenarios are suggested as shown in Table 2.2. The channel size, the proportion of facies, the number of facies and the position of channels are varying for each scenario. The parameter values are presented in Table 2.2. 50 models were generated for each scenario, resulting in a total of 800 realizations. Examples of some realizations are shown in Figure 2.6 (left). Normal-incidence reflection seismic data is forward modeled on each realization using a convolution model with a target depth of 1000m and frequency of 50Hz, for two cases:

Case 1 (good quality seismic): we use a simple rock-physics model, with constant velocity and density in each facies. In addition, the grid cell size is 12.5 by 2.5 meter, which allows for a better seismic resolution.

Case 2 (low resolution seismic): we use a realistic rock-physics model, borrowed from real well data (from North Sea). A geostatistical algorithm, sequential Gaussian simulation is used to spatially sample heterogeneous values of velocity and density. The dz of the grid cell is reduced to 1m, which makes the channel below seismic resolution.

Example of some of the seismic responses obtained for each case is shown in

Figure 2.6 (center: high resolution and right: low resolution). For each seismic quality, the probability of each scenario given the data is computed using the proposed approach and compared with rejection sampling. Note that in rejection sampling, we select the models based on the JS divergence distance, i.e. models having similar histograms to the reference.

Table 2. 2: Multiple (16) geological scenarios using different parameter settings.

Facies Geometry	Proportion (Shale/Sand)	Channel size (width:thick= 1.5:1)	Rockphysics (B/O)	Scenario (Random)	Scenario (Stacked)
Random or Stacked	Sand:20%	Thickness: 10	2 facies	1	9
			3 facies	2	10
		Thickness: 20	2 facies	3	11
			3 facies	4	12
	Sand:30%	Thickness: 10	2 facies	5	13
			3 facies	6	14
		Thickness: 20	2 facies	7	15
			3 facies	8	16

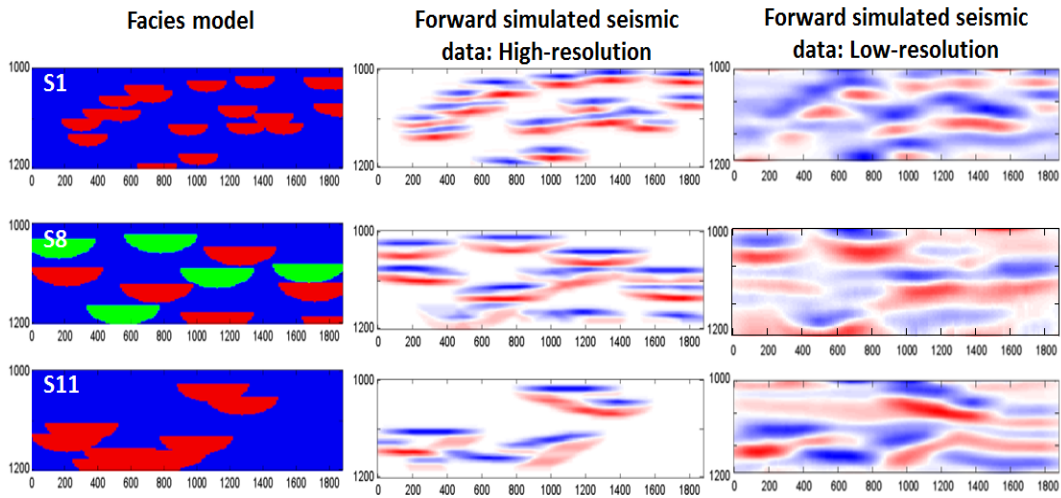


Figure 2. 6: Example of a few models (from scenario 1(top), 8(mid), and 11(bottom), left) and its forward simulated seismic data for high resolution (center) and low resolution (right).

2.5 Results

First, we generated 50 prior models from each scenario (total 800 models) using object-based geostatistical algorithm (SGems-Ti generator). The models of each scenario are used to generate a probability density function in MDS map by adaptive kernel smoothing technique (See Figure 2.7). As stated in methodology, pattern capturing technique and JS divergence are applied to project the distances between the models and the obtained data. According to the Equation (2.2) and (2.3), the estimated pdf value represents the likelihood of each scenario within the obtained data. In an example of Figure 2.7, we used 10 dimensions for generating kernel density function since eigenvalues of 10 dimensions can explain over 99% of variances; however, for visualization we showed it in 2D. As the same way, we repeat this for all 16 scenarios and estimate the probability.

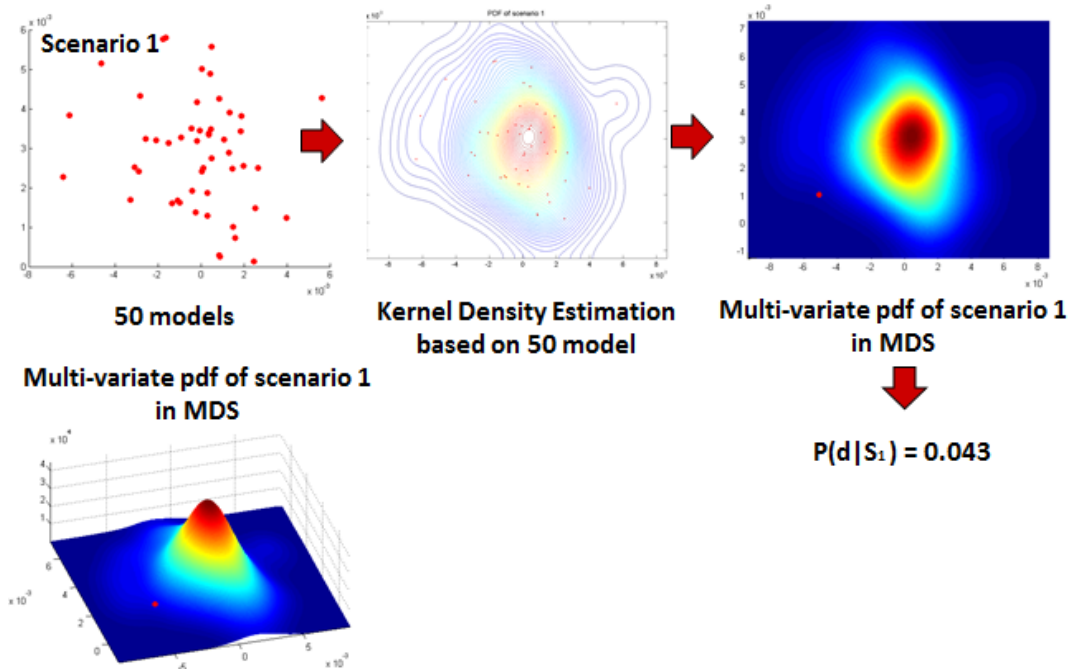


Figure 2. 7: A process of estimating $P(S_k|d)$. First, generate 50 prior models from each scenario and project it in MDS map. Next, create the probability density function by using adaptive kernel density estimation, and estimate the probability of data location from the multi-dimensional pdf.

2.5.1 Case 1 (good quality seismic)

Figure 2.8 shows 2D representations of the metric space defined by the MPH-based distance (left) and DWT-based distance (right). The values displayed on the axes indicate the contribution of each dimension (eigenvalues). The first dimension in this case is quite dominant, with over 71% and 80% of the total contribution, respectively. We observe that points in the same scenarios are close to each other, which indicates a reasonable distinction between the scenarios. A Bayesian confusion matrix is computed to assess the classification performances of the proposed distance. The matrix is constructed by counting the number of times the predicted value matches the actual (expected value). For perfect classification, the matrix will have zeros everywhere except on the diagonal with 100% models classified in the correct class. The Bayesian matrix is computed by finding which scenario the model belongs to, after evaluating the probability of each scenario given the model using MDS and kernel smoothing.

For Case 1, the Bayesian confusion matrix is represented in Table 2.3 (for MPH-based distance) and Table 2.4 (for DWT-based distance). The total misclassification error is about 11% and 12%, which indicates a reliable classification. Analysis of the matrix shows that the most important misclassification of MPH-based distance occurs from difference in the number of facies (highlighted in red). The DWT-based distance analysis shows that the main misclassification appears in difference of proportion (green) and position or stacking pattern (blue). Note that the kernel smoothing and

therefore the Bayesian confusion matrix is a function of the dimension of the MDS space and the number of clusters chosen in the adaptive kernel smoothing. An optimization procedure was performed to find the values that minimize the misclassification in the Bayesian confusion matrix. For this example, 6 dimensions and 2 clusters are optimal. For the references (illustrated in Figure 2.8 (top, left)), the posterior probabilities obtained by kernel smoothing (KS) in MDS and rejection sampling (RS) are shown in Tables 2.5. The probabilities obtained by KS and RS are very close. However, the number of model evaluations required for RS to obtain 30 models that are close to the given reference data is dramatically increased to 78,681 in MPH-based distance and 108,647 in DWT-based distance. The proposed methodology derives posterior probability similar to the one obtained by rejection sampling, at only a fraction of the cost.

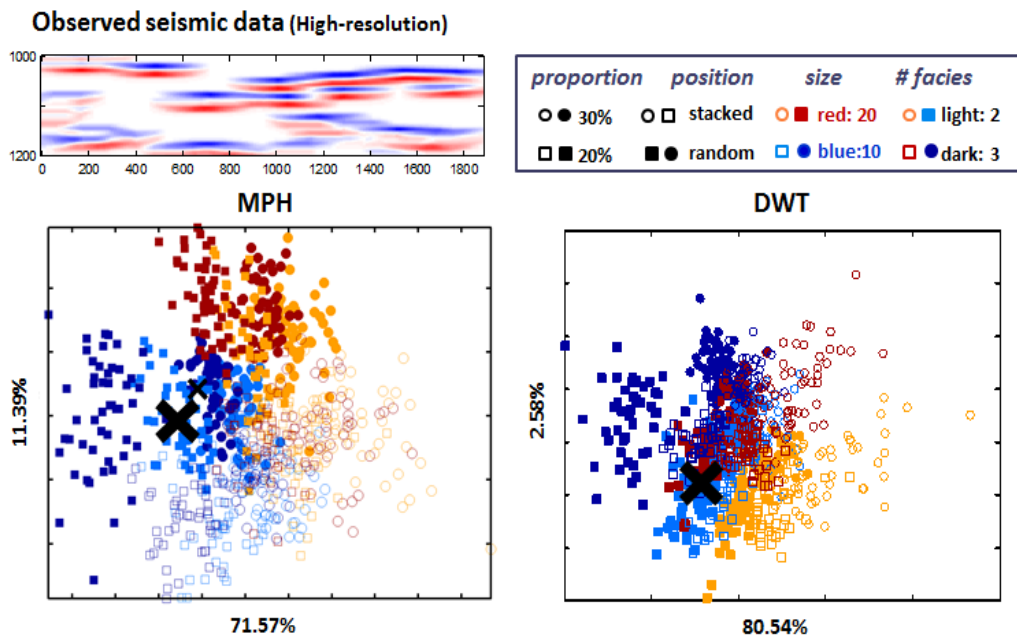


Figure 2. 8: 2D representation of metric space (Case 1). The reference is represented by a black cross.

Table 2. 3: Bayesian confusion matrix of MPH-based for Case 1

		Predicted class															
		Difference in # facies															
		Sc1	Sc2	Sc3	Sc4	Sc5	Sc6	Sc7	Sc8	Sc9	Sc10	Sc11	Sc12	Sc13	Sc14	Sc15	Sc16
Actual class	Sc1	84	10	-	-	-	-	-	-	2	4	-	-	-	-	-	-
	Sc2	2	98	-	-	-	-	-	-	-	-	-	-	-	-	-	-
	Sc3	-	-	86	12	-	-	-	-	-	-	-	2	-	-	-	-
	Sc4	-	-	4	96	-	-	-	-	-	-	-	-	-	-	-	-
	Sc5	2	4	-	-	90	-	-	-	-	-	-	-	-	-	4	-
	Sc6	-	-	-	-	2	98	-	-	-	-	-	-	-	-	-	-
	Sc7	-	-	2	-	-	-	88	2	-	-	-	-	-	-	-	8
	Sc8	-	-	-	-	-	-	-	100	-	-	-	-	-	-	-	-
	Sc9	-	-	-	-	-	-	-	-	86	14	-	-	-	-	-	-
	Sc10	4	-	-	-	-	-	-	-	14	82	-	-	-	-	-	-
	Sc11	-	-	2	-	-	-	-	-	-	-	96	2	-	-	-	-
	Sc12	-	-	-	-	-	-	-	-	-	-	16	78	-	-	2	4
	Sc13	-	-	-	-	4	-	-	-	2	4	-	-	78	12	-	-
	Sc14	-	-	-	-	-	-	-	-	-	-	-	-	2	98	-	-
	Sc15	-	-	2	-	-	-	-	-	-	-	10	8	-	-	70	10
	Sc16	-	-	-	-	-	-	-	-	-	-	-	-	-	-	2	98

Table 2. 4: Bayesian confusion matrix of DWT-based for Case 1

		Predicted class															
		Difference proportion															
		Difference position															
		Sc1	Sc2	Sc3	Sc4	Sc5	Sc6	Sc7	Sc8	Sc9	Sc10	Sc11	Sc12	Sc13	Sc14	Sc15	Sc16
Actual class	Sc1	94	-	-	-	-	-	-	-	6	-	-	-	-	-	-	-
	Sc2	-	98	-	-	-	-	-	-	-	2	-	-	-	-	-	-
	Sc3	-	-	94	-	-	-	2	-	-	-	4	-	-	-	-	-
	Sc4	-	2	-	98	-	-	-	-	-	-	-	-	-	-	-	-
	Sc5	4	-	-	-	88	-	-	-	-	-	-	-	8	-	-	-
	Sc6	-	-	-	-	-	96	-	-	-	-	-	-	-	4	-	-
	Sc7	-	-	4	-	-	-	86	-	-	-	-	-	2	-	6	2
	Sc8	-	-	-	4	-	-	-	94	-	-	-	-	-	-	-	2
	Sc9	12	-	2	-	-	-	-	-	82	-	2	-	-	-	-	2
	Sc10	-	4	-	-	-	-	-	-	2	92	-	-	-	-	-	2
	Sc11	-	-	8	-	-	-	-	-	2	-	78	-	-	-	12	-
	Sc12	-	-	-	2	-	-	-	-	-	4	4	84	-	-	-	6
	Sc13	4	2	-	-	16	-	-	-	8	-	-	-	70	-	-	-
	Sc14	-	-	-	-	-	-	-	-	-	-	-	-	-	100	-	-
	Sc15	-	-	4	-	-	-	2	-	-	-	22	-	-	-	68	4
	Sc16	-	-	-	4	-	-	-	-	-	-	-	6	-	-	2	88

Table 2. 5: Probability of each scenario given seismic data for the proposed approach and rejection sampling - Case 1

<MPH>	S1	S2	S3	S4	S5	S6	S7	S8	S9	S10	S11	S12	S13	S14	S15	S16
KS (800)	0.03	0	0	0	0.78	0	0	0.11	0	0	0	0	0.07	0	0	0
RS (78681)	0	0	0	0	0.80	0	0	0.10	0	0	0	0	0.10	0	0	0

<DWT>	S1	S2	S3	S4	S5	S6	S7	S8	S9	S10	S11	S12	S13	S14	S15	S16
KS (800)	0	0	0	0	0.9	0	0	0	0	0	0	0	0.1	0	0	0
RS (108647)	0	0	0	0	0.8	0	0	0.1	0	0	0	0	0.1	0	0	0

2.5.2 Case 2 (low quality seismic)

Figure 2.9 shows the MDS representation of the 800 initial models, colored by scenario. The eigenvalue contribution of the first dimension is much lower than for Case 1 (MPH: from 71% to 25%; DWT: from 80% to 43%). A reasonable distinction of the different scenarios is still observable in 2D. As expected, a higher misclassification error is observed for this case (55% for MPH-based and 43% for DWT-based, See Table 2. 6 and Table 2. 7). In both approaches, the principal errors in the classification were mostly due to misclassification of proportion of facies. A second source of error was the difference of positioning of the geobodies. For the reference cases (Figure 2.9), the probabilities obtained by kernel smoothing and rejection sampling are similar (Table 2. 8). Compared to the case 1 result, it has a less distinct seismic response and thus the classification is harder and fewer scenarios can be rejected. Scenarios 1, 5, 7 and 13 are possible given the seismic data.

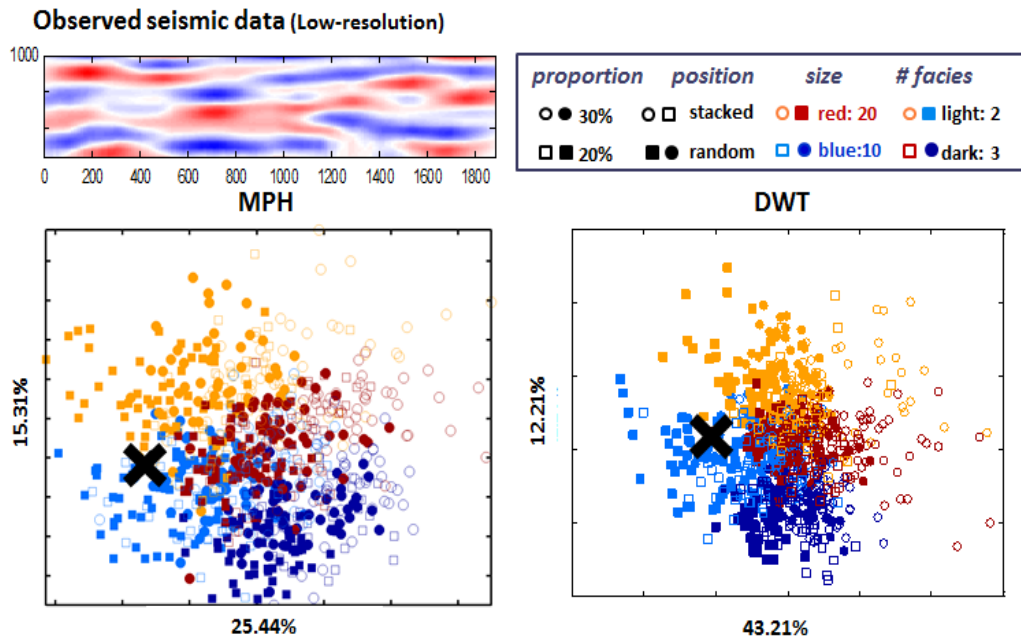


Figure 2. 9: 2D representation of metric space (Case 2). The reference is represented by a black cross.

Table 2. 6: Bayesian confusion matrix of MPH-based for Case 2

		Predicted class															
		Difference in # facies															
		Sc1	Sc2	Sc3	Sc4	Sc5	Sc6	Sc7	Sc8	Sc9	Sc10	Sc11	Sc12	Sc13	Sc14	Sc15	Sc16
Actual class	Sc1	84	10	-	-	-	-	-	-	2	4	-	-	-	-	-	-
	Sc2	2	98	-	-	-	-	-	-	-	-	-	-	-	-	-	-
	Sc3	-	-	86	12	-	-	-	-	-	-	2	-	-	-	-	-
	Sc4	-	-	4	96	-	-	-	-	-	-	-	-	-	-	-	-
	Sc5	2	4	-	-	90	-	-	-	-	-	-	-	-	-	4	-
	Sc6	-	-	-	-	2	98	-	-	-	-	-	-	-	-	-	-
	Sc7	-	-	2	-	-	-	88	2	-	-	-	-	-	-	-	8
	Sc8	-	-	-	-	-	-	-	100	-	-	-	-	-	-	-	-
	Sc9	-	-	-	-	-	-	-	-	86	14	-	-	-	-	-	-
	Sc10	4	-	-	-	-	-	-	-	14	82	-	-	-	-	-	-
	Sc11	-	-	2	-	-	-	-	-	-	-	96	2	-	-	-	-
	Sc12	-	-	-	-	-	-	-	-	-	-	16	78	-	-	2	4
	Sc13	-	-	-	-	4	-	-	-	2	4	-	-	78	12	-	-
	Sc14	-	-	-	-	-	-	-	-	-	-	-	-	2	98	-	-
	Sc15	-	-	2	-	-	-	-	-	-	-	10	8	-	-	70	10
	Sc16	-	-	-	-	-	-	-	-	-	-	-	-	-	-	2	98

Table 2. 7: Bayesian confusion matrix of DWT-based for Case 2

		Predicted class															
		Difference proportion															
		Difference position															
		Sc1	Sc2	Sc3	Sc4	Sc5	Sc6	Sc7	Sc8	Sc9	Sc10	Sc11	Sc12	Sc13	Sc14	Sc15	Sc16
Actual class	Sc1	94	-	-	-	-	-	-	-	6	-	-	-	-	-	-	-
	Sc2	-	98	-	-	-	-	-	-	-	2	-	-	-	-	-	-
	Sc3	-	-	94	-	-	-	2	-	-	-	4	-	-	-	-	-
	Sc4	-	2	-	98	-	-	-	-	-	-	-	-	-	-	-	-
	Sc5	4	-	-	-	88	-	-	-	-	-	-	-	8	-	-	-
	Sc6	-	-	-	-	-	96	-	-	-	-	-	-	-	4	-	-
	Sc7	-	-	4	-	-	-	86	-	-	-	-	-	2	-	6	2
	Sc8	-	-	-	4	-	-	-	94	-	-	-	-	-	-	-	2
	Sc9	12	-	2	-	-	-	-	-	82	-	2	-	-	-	-	2
	Sc10	-	4	-	-	-	-	-	-	2	92	-	-	-	-	-	2
	Sc11	-	-	8	-	-	-	-	-	2	-	78	-	-	-	12	-
	Sc12	-	-	-	2	-	-	-	-	-	4	4	84	-	-	-	6
	Sc13	4	2	-	-	16	-	-	-	8	-	-	-	70	-	-	-
	Sc14	-	-	-	-	-	-	-	-	-	-	-	-	-	100	-	-
	Sc15	-	-	4	-	-	-	2	-	-	-	22	-	-	-	68	4
	Sc16	-	-	-	4	-	-	-	-	-	-	-	6	-	-	2	88

Table 2. 8: Probability of each scenario given seismic data for the approach and rejection sampling - Case 2

<MPH>	S1	S2	S3	S4	S5	S6	S7	S8	S9	S10	S11	S12	S13	S14	S15	S16
KS (800)	0.27	0	0	0	0.73	0	0.01	0	0	0	0	0	0.21	0	0	0
RS (97406)	0.10	0	0	0	0.63	0	0.13	0	0	0	0	0	0.10	0	0	0
<DWT>	S1	S2	S3	S4	S5	S6	S7	S8	S9	S10	S11	S12	S13	S14	S15	S16
KS (800)	0	0	0	0	0.7	0	0.1	0	0	0	0	0	0.2	0	0	0
RS (113041)	0	0	0	0	0.5	0	0.1	0	0	0	0	0	0.3	0	0.1	0

2.6 Conclusions

We present a methodology to screen prior geological scenarios based on seismic data. A statistical distance between seismic images defined using pattern capturing algorithms (MPH or DWT) and JS divergence is capable of identifying geologic scenarios consistent with the observed seismic response (and hence helps to decide which scenarios can be rejected). Synthetic case studies having different seismic resolution with 16 different geologic scenarios are presented. As expected, the better the seismic quality, the better the distance and the distinction between the 16 scenarios. We also observe that the proportion and the positioning of the facies are the most difficult parameters to differentiate in this study, where more misclassification is present. Using the proposed approach, we were able to reproduce quite accurately the probabilities obtained by rejection sampling (and thus reject scenarios with zero probability), using only a fraction of evaluations.

To obtain fully matched models with the obtained seismic data under uncertain geological scenarios, a seismic inversion process $P(m|S_k, d)$ should be performed sequentially after the geological scenario modeling. Based on the result, Markov chain Monte Carlo (MCMC) algorithms can be applied to sample the posterior distribution integrating geological scenarios and the given seismic data.

2.7 Acknowledgment

The authors thankfully acknowledge Stanford Center for Reservoir Forecasting

(SCRF) sponsors.

2.8 References

Borg, I., Groenen, P. 1997. Modern multidimensional scaling: theory and applications, New-York, Springer.

Caers, J., 2011, Modeling uncertainty in the Earth sciences, Wiley-Blackwell.

Cover, T. M., Thomas, J. A., 1991, Elements of information theory, Wiley-Interscience, New York, NY, USA.

Deutsch, C., Gringarten, E., 2000, Accounting for multiple-point continuity in geostatistical modeling, In: of Southern Africa, G. A. (Ed.), 6th International Geostatistics Congress. Vol. 1. Cape Town, South Africa, pp. 156-165.

Endres, D. M. and Schindelin, J. E., 2003, A new metric for probability distributions, IEEE Transactions on Information Theory 49 (7), 1858-1860.

Heeger, D. J., and Bergen, J. R., 1995, Pyramid-based texture analysis/synthesis, In Proceedings of the 22nd annual conference on Computer graphics and interactive techniques, pp. 229-238, ACM.

Honarkhah, M. and Caers, J., 2010, Stochastic Simulation of Patterns Using Distance-Based Pattern Modeling, Mathematical Geosciences, 42: 487-517, DOI: 10.1007/s11004-010-9276-7.

- Kullback, S. and Leibler, R. A., 1951, On Information and Sufficiency, *Annals of Mathematical Statistics* 22 (1): 79–86, DOI:10.1214/aoms/1177729694. MR 39968.
- Kullback, S., 1983, Kullback information, *Encyclopedia of Statistical Sciences*, Vo14, 421-425 New York: Wiley.
- Lange, K., Frydendall, J., Cordua, K. S., Hansen, T. M., Melnikova, Y., & Mosegaard, K., 2012, A Frequency Matching Method: Solving Inverse Problems by Use of Geologically Realistic Prior Information, *Mathematical Geosciences*, 44: 783-803, DOI: 10.1007/s11004-012-9417-2.
- Park H., Scheidt C., Fenwick, D., Boucher A. and Caers J., 2013, History matching and uncertainty quantification of facies models with multiple geological interpretations, *Computational Geosciences*, DOI: 10.1007/s10596-013-9343-5.
- Thomas, E. C., and Stieber, S. J., 1975, The Distribution of Shale in Sandstones and Its Effect Upon Porosity: *Trans. Of the 16th Annual Logging Symposium of the SPWLA paper.*

Chapter 3

A fast approximation for seismic inverse modeling: Adaptive Spatial Resampling

*“All truths are easy to understand once they are discovered;
the point is to discover them.”*

- Galileo Galilei

3.1 Abstract

Seismic inverse modeling, which transforms appropriately processed geophysical data into physical properties of the Earth, is an essential process for reservoir characterization. We propose a workflow based on Markov chain Monte Carlo

(McMC), consistent with geology, well-logs, seismic data and rock-physics information. It uses the Direct Sampling (DS) multiple-point geostatistical method for generating realizations from the prior distribution, and Adaptive Spatial Resampling (ASR) to perform stochastic optimization and an approximate sampling from the posterior distribution conditioned to the geophysical data.

Sampling is a more general approach than just finding the most likely model as it can assess important uncertainties. However, since rejection sampling requires a large number of evaluations of forward model, it is inefficient and not suitable for reservoir modeling. Metropolis sampling is able to perform a reasonably equivalent sampling by forming a Markov chain. The Iterative Spatial Resampling (ISR) algorithm perturbs realizations of a spatially dependent variable while preserving its spatial structure by conditioning to subset points. However, in most practical applications, when the subset conditioning points are selected at random, it can get stuck for a very long time in a non-optimal local minimum. In this dissertation we improve the efficiency of ISR by adaptive sampling. Depending on the acceptance/rejection criterion, it is possible to obtain a chain of geostatistical realizations aimed at characterizing the posterior distribution with Metropolis. The validity and applicability of the proposed method is illustrated by results for seismic lithofacies inversion on the Stanford VI synthetic test set.

3.2 Introduction

Seismic data play a key role to reduce uncertainty in predictions of rocks and fluids away from well control points. However, in real applications it is nearly impossible to find a unique relationship between seismic response and reservoir properties. Seismic measurements are noisy and have larger scales of resolution than well data. Moreover, the relationships are non-unique due to the limited frequency of seismic waves, the forward modeling simplifications, and natural heterogeneity.

Statistical rock physics accounts for some of the uncertainty using multi-variate stochastic relations between elastic parameters and reservoir properties (Mukerji et al., 2001a; Mukerji et al., 2001b; Avseth et al., 2005). Many different workflows have been suggested to combine rock physics and geostatistical methods in seismic inversion. Bosch et al. (2010) classified these approaches into two groups, which are the sequential or cascaded approach and the joint or simultaneous workflow in a Bayesian formulation. Traditional approaches, known as sequential or cascaded approach (Dubrule, 2003; Doyen, 2007) start from transforming elastic properties into statistical classification properties (probability maps), and use it as soft data for geostatistical simulation. The joint or simultaneous workflow accounts for the elastic parameters and the reservoir properties together and provides combined uncertainties. These Bayesian workflows include rock-physics relations to link between reservoir properties and elastic properties, and geostatistical models to provide geologically consistent prior models. Forward modeled synthetic data are compared with obtained seismic data to calculate the likelihood, and the final solutions are posterior models consistent with the expected geology, well data and seismic data. Eidsvik et al. (2004)

formulate the simultaneous inversion using a Bayesian network model, and spatial continuity of priors is incorporated in a Markov random-field model. Larsen et al. (2006) incorporate vertical spatial correlation using a Markov-chain model, and Ulvmoen and More (2010) apply the Markov-chain model in lithology/fluid inversion in a Bayesian framework. Bachrach (2006) apply Markov chain Monte Carlo (MCMC) with stochastic rockphysics modeling for joint estimation of porosity and saturation. Contreras et al. (2005) suggest joint stochastic inversion of well logs and 3D pre-stack seismic data based on MCMC updates. Gonzalez et al. (2008) combine multiple points geostatistics (MPS) and rock physics for seismic inversion. They generate multiple realizations of reservoir facies and saturations, conditioned to seismic and well data. MPS is used to characterize the geologic prior information, and statistical rock physics links reservoir properties to elastic properties. Thus their method provides multiple realizations, all consistent with the expected geology, well-log, seismic data and local rock-physics transformations. However, this workflow does not produce samples of the full posterior probability density function but generates multiple optimized models around the mode of the posterior. Also the MPS algorithm is inefficient for application to 3-D and complicated actual field cases.

Among posterior sampling methods, rejection sampler (Tarantola, 2005) is a classic method to sample the posterior pdf. However, since it requires a large number of evaluations of forward model, rejection sampling is inefficient. Therefore, a key issue is to generate prior models and to find the posterior models honoring both spatial constraints and seismic data within limited computation time and cost.

We propose a Markov chain Monte Carlo (MCMC) workflow consistent with geology, well-logs, seismic data and rock-physics information. The workflow uses Direct Sampling (DS), a multiple-point geostatistical method (Mariethoz, 2010a), for generating realizations from the prior distribution and the Metropolis algorithm with Adaptive Spatial Resampling (ASR) for approximate sampling from the posterior distribution conditioned to the geophysical data. Since the conventional MPS algorithms such as SNESIM or SIMPAT store all data events from the training image (Strebelle, 2000; Arpat, 2005), computational cost is dramatically increased according to the size of the template and the number of facies. The DS algorithm directly samples the training image for any given data event, without storing all patterns in a database. The principle of the method is that, for each simulated node, the training image is randomly scanned for a given conditional data event. The value of the central node of the first matching data event is then used for simulation because it corresponds to a conditional sample. The advantage is that the simulation is very lightweight in terms of memory usage, CPU efficient, flexible and able to reproduce the structures of complex training images and deal with a range of non-stationary problems. However, strength of ASR is that it is not specific to DS but could be associated with any MPS algorithms such as SNESIM, DISPAT (Honarkhah and Caers, 2012), CCSIM (Tahmasebi et al., 2012) and so forth.

The MCMC algorithm (both ISR and ASR) perturbs realizations of a spatially dependent variable while preserving its spatial structure. The method is used as a transition kernel to produce a Markov chain of geostatistical realizations. These

realizations are then used in a forward seismic model to compute the predicted data which are compared to the observed data. Depending on the acceptance/rejection criterion in the Markov process, it is possible to obtain a chain of realizations aimed at characterizing the posterior distribution with Metropolis sampling. The proposed workflow is shown in Figure 3.1. The important difference between ISR and ASR is that ASR adaptively samples a subset of points from the previous accepted model instead of random selection. In most practical applications, we observed ISR chains getting stuck for a long time in a certain stage since the randomly selected unpromising points are iteratively used as conditioning points for model generation in the next step. In this dissertation we propose adaptive spatial resampling as a fast and approximate sampler for improving the efficiency of ISR, and we show how it can be applied for seismic inversion. Though ISR has been presented before, it has not been applied so far for seismic inversion. The proposed method is demonstrated on a synthetic test dataset.

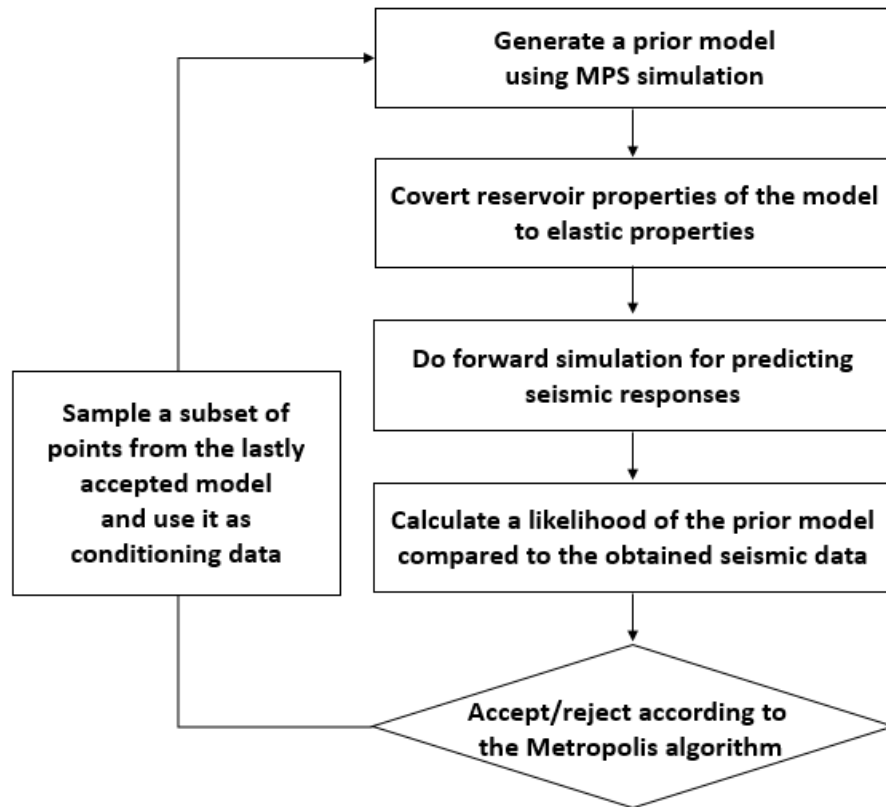


Figure 3. 1: A flowchart of the MCMC process with the Metropolis sampler. In the resampling step for selecting conditioning points, the proposed ASR algorithm adaptively resamples a subset from the lastly accepted model instead of random selection in ISR.

3.3 Methodology

3.3.1 Seismic inverse modeling in a Bayesian framework

The transformation of geophysical data into reservoir properties can be posed as an inference problem involving the updating of prior knowledge with newly available data (Tarantola, 1987, 2005). Following Baye's rule, it can be expressed as

$$P_{post}(m) = c P_{prior}(m) P_{data}(d_{obs} - g(m)), \quad (3.1)$$

where $P_{post}(m)$ is the posterior probability density and $P_{prior}(m)$ is a priori probability density. In Equation (3.1), c is a normalizing constant, and m is the earth model parameter configuration. The expression $P_{data}(d_{obs} - g(m))$ is the likelihood function; and it depends on the observations d_{obs} and their uncertainty, and the forward modeling operator g that maps the model space into the data space. The solutions of an inverse problem are the set of earth-model configurations that, when forward modeled into synthetic data, match the real data within some tolerance (Bosch et al., 2010).

Bosch et al. (2004) decomposed the model space into reservoir parameters (facies, porosity, etc.) and elastic parameters (seismic velocity and density), and thus the prior can be written as:

$$P_{prior}(m_{res}, m_{elas}) = P_{prior}(m_{res}) P_{prior}(m_{elas}|m_{res}), \quad (3.2)$$

where $P_{prior}(m_{res})$ is the prior pdf for the reservoir parameters (including their spatial distributions) and $P_{prior}(m_{elas}|m_{res})$ is a conditional probability for the elastic parameters that summarizes the rock physics relationships between reservoir property and elastic property. Thus, the final posterior pdf for the joint rock physics and seismic inversion is the following combination of Equation (3.1) and (3.2):

$$\begin{aligned} P_{post}(m_{res}, m_{elas}) \\ = c P_{prior}(m_{res}) P_{prior}(m_{elas}|m_{res}) P_{data}(d_{obs} - g(m_{elas})). \end{aligned} \quad (3.3)$$

The petrophysical conditional density $P_{prior}(m_{elas}|m_{res})$ is the rockphysics forward function that maps the reservoir model parameters (lithofacies, porosity and saturations) to the elastic model parameters. Many different seismic inversion workflows combining elastic properties, geostatistics, and rock-physics models to predict reservoir properties can be presented in the shape of Equation (3.3). This workflow in a Bayesian formulation guarantees consistency between the elastic and reservoir properties. The Equation (3.3) is one of the ultimate goals of this dissertation to find $P(m_{res}|S_k, d)$ shown in Equation (2.1). In this chapter, the posterior

distribution ($P_{post}(m_{res}, m_{elas})$) is sampled within given data and training images as the selected geological scenarios.

As shown by Hansen et al. (2012), the extended Metropolis algorithm samples the posterior pdf with the observed data and an assumed noise model. The likelihood of a given model is computed as

$$L(m_{elas}) = P_{data}(d_{obs} - g(m_{elas})) = \exp\left[-\frac{(d_{obs}^i - g^i(m_{elas}))^2}{2\sigma^2}\right], \quad (3.4)$$

where σ is the variance of the noise added to the synthetically forward simulated data. We applied two different noise models for each different type of seismic data. One of main sources of the noise in our example is the uncertainty in the rockphysics models for the sand and shale facies. Since P-wave velocities and densities are not constant values but assigned from a bivariate pdf of each facies, the computed acoustic impedance has a large variability. For the impedance data, we applied a frequency-domain Born filter to consider surface seismic reflection geometry with a 5~50 Hz bandwidth. For normal-incidence seismic section, we assumed convolutional seismic forward modeling with 10% random noise and applied a 50 Hz wavelet.

3.3.2 Rejection sampling

Sampling the posterior models is more important than a single optimization result but in practice it may be nearly impossible to apply because sampling takes tremendous time and cost. These problems are critical especially in complex models such as an actual reservoir case. Tarantola (2005) gives an overview of an exact method to obtain representative samples of $P_{post}(m|d)$. Rejection sampling is based on the fact that the posterior is a subset of the prior distribution, and therefore it can be evaluated by sampling the prior. The approach consists in generating candidate models m^* that are samples of $P_{prior}(m)$ and to accept each of them with a probability in Equation (3.5)

$$P(m^*) = \frac{L(m^*)}{L(m)_{max}}, \quad (3.5)$$

where $L(m)$ is likelihood which represents the misfit between observed data (d_{obs}) and the forward simulated model ($g(m)$). $L(m)_{max}$ denotes the supremum, which can be any number equal or above the maximum likelihood value that can be taken by $L(m)$. The distribution of the resulting samples follows posterior distribution of models. Since it requires a large number of evaluations of $P_{prior}(m)$, the rejection method is inefficient.

3.3.3 Iterative spatial resampling

The Metropolis algorithm (Metropolis et al., 1953) samples the posterior by forming a Markov chain of models, such that the steady-state distribution of the chain is precisely the posterior distribution that one wishes to sample from. It is similar to a random walk that would preferentially visit the areas where $P_{post}(m|d)$ is high (Hansen et al., 2008; Hansen et al., 2012). Specifically in reservoir modeling, the issue is how to form and perturb a Markov chain while preserving spatial structure of geomodels in the chain. One way is to sample a subset of points from previous model in a chain, and use the points as conditioning data for the next simulated realization. Since the simulation uses the same training image (or other spatial information about the prior) the spatial structure of the models in the chain is preserved.

Mariethoz et al. (2010b) suggested this Iterative Spatial Resampling (ISR) method to perturb realizations of a spatially dependent variable while preserving its spatial structure. This method is used as a transition kernel to produce Markov chains of geostatistical realizations. It has been applied for flow problems but has not been tested for seismic inversion. Implementing the Metropolis sampler using ISR (M-ISR) to sample the prior is accomplished by performing the following steps at each iteration i (Figure 3.2 and Figure 3.3).

Algorithm 1: Metropolis sampler using ISR (M-ISR)

Input: Training image, Obtained seismic data, A number of subset points

Steps:

- a. Generate the first model m_1 by multi-point geostatistical simulation and evaluate its likelihood, $L(m_1) = P_{data}(d_{obs} - g(m_{1,elas}))$. The model of current state $m_c = m_1$.
- b. Select r_i as a random subset of points from m_c .
- c. Generate a proposal model m^* by conditional simulation using r_i as conditioning data.
- d. Evaluate $L(m^*)$ and accept m^* with probability, $P_{accept} = \min(1, L(m^*)/L(m_c))$ (Metropolis et al, 1953; Mosegaard and Tarantola, 1995).
- e. If m^* is accepted $m_c = m^*$, else reuse m_c .
- f. Iterate b ~ e.

The Metropolis sampler using ISR theoretically samples the exact posterior distribution as an alternative method of a rejection sampler. However, in terms of efficiency, it is still slow and impractical. Thus we propose a compromise to make it applicable by using auxiliary information. The price to pay is that the sampling is inexact, even though illustrated test cases show that in practice the sampling is often reasonably accurate.

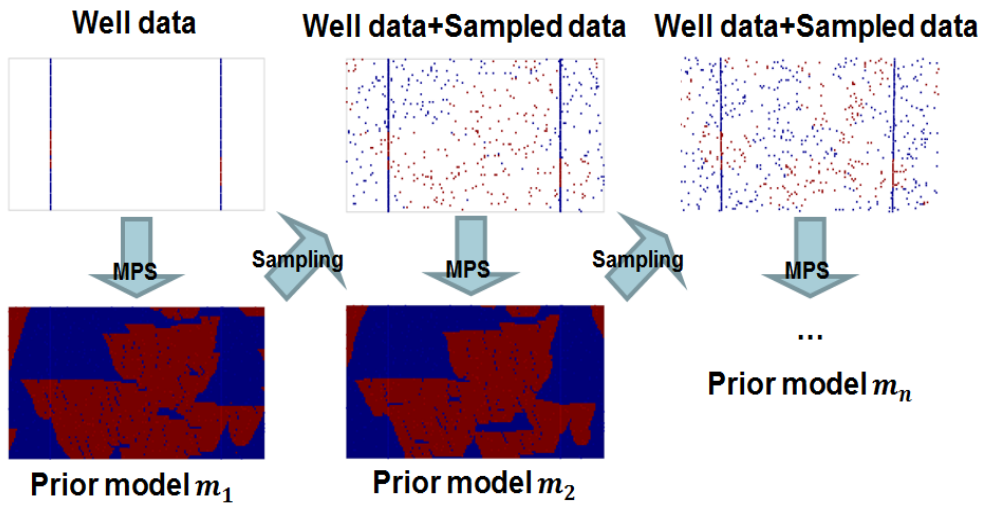


Figure 3. 2: Sketch of the Iterative Spatial Resampling method (ISR). An initial model m_1 is randomly sampled to obtain the subset, which is used as conditioning data for generating next model m_2 . m_2 displays similar local features as m_1 due to the constraints imposed by the conditioning data, but represents a different realization from the prior multi-point geostatistical model.

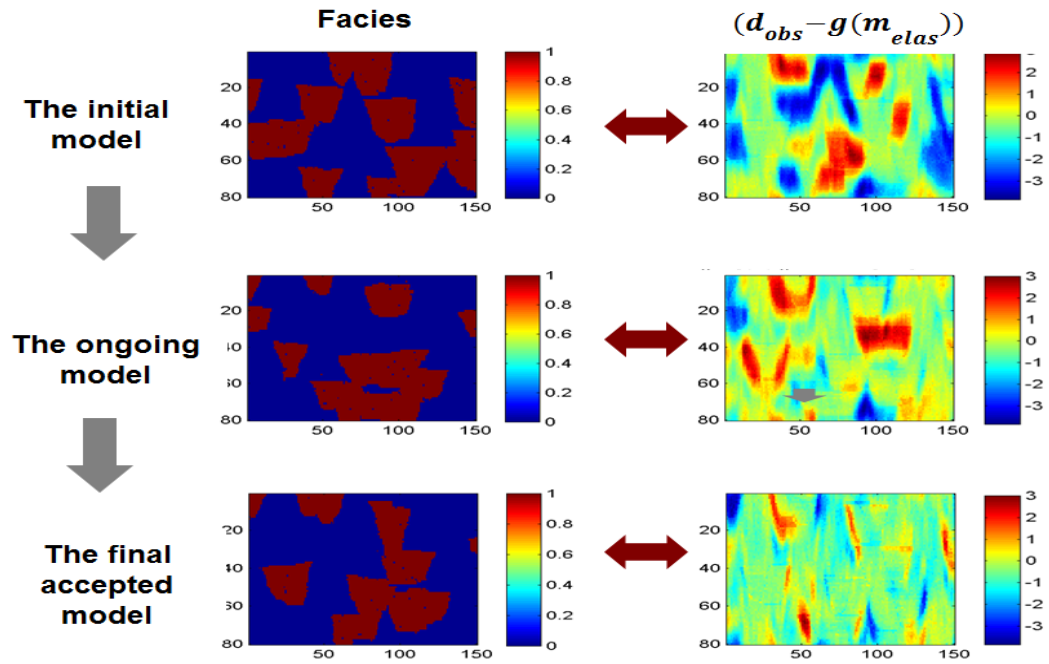


Figure 3. 3: The iteration of a Markov chain using ISR. Left: generated facies models; Right: the residual between seismic impedance and predicted impedance from the earth model in each step. This misfit is getting smaller with iterations.

3.3.4 Adaptive spatial resampling

The search strategy of ISR performs successive steps in random directions for exploring various regions of the solution space. Since the search is stochastic, the posterior distribution theoretically will be reached after an infinite number of iterations. However, in most practical applications, when the subset conditioning points are selected at random, it can get stuck for a very long time in a non-optimal local minimum. In this work we improve the efficiency of ISR by adaptive sampling.

At the every iteration, we compare the predicted seismic data with the observed data and thus we have a spatial error map. Figure 3.4 shows an example of the spatial error map and it is a residual error between a forward simulated model and the obtained data. We can use this spatial information for generating the next step. Instead of just randomly sampling a subset of points to condition the next realization, we adaptively sample important points having lower residual error (see Figure 3.4). The idea is to freeze for the next iteration parts of the domain that yield low error, while the high error locations can be updated. The algorithm probabilistically selects a subset of conditioning points, with a probability based on the residual error pdf. Locations with a lower error have a higher chance to be accepted as conditioning points. The probability of a location to be selected as conditioning data for the next iteration is defined in Equation (3.6),

$$P_{\text{cond}}(\mathbf{x}) \propto \frac{N - R(\mathbf{x}) + 1}{N} \quad \forall R(\mathbf{x}) = \text{Rank}(|\text{error}(\mathbf{x})|), \quad (3.6)$$

where $error(x)$ is the misfit at each cell location x and N is the total number of cells in an error map. The number of resampled points is defined as a fraction of the total number of cells. This preferential probabilistic selection of favorable locations causes Adaptive Spatial Resampling (ASR) to accelerate the procedure and to efficiently sample posterior models consistent with the given data.

The idea to use auxiliary values of a previous state with probabilistic preference is very similar to the adaptive McMC (Haario et al., 2001) and the auxiliary variable sampler (Andrieu et al., 2003). The adaptive McMC is a scheme to tune the proposal distribution using previous values of the chain. Since conventional Markov chains can get stuck at each state for a long time, updating the proposal distribution can help the chains to reach the posterior distribution earlier. Many algorithms and examples are discussed (Roberts and Rosenthal, 2009; Andrieu and Thoms, 2008), and we propose the ASR algorithm as a variant of adaptive McMC and auxiliary variable sampler. However, a problem is the adaptive McMC may violate the Markov property of the transition kernel. To avoid this problem, Andrieu et al. (2003) suggest using adaption only during an initial fixed number of steps, and next doing pure McMC after jumping to the posterior distribution. In this dissertation, we focus on the applicability of the ASR as an approximate and alternative posterior sampler; however, one could carry out theoretically sound posterior sampling with both ASR for burn-in period and ISR for standard McMC simulation.

Algorithm 2: Approximate Metropolis sampler using ASR (M-ASR)

Input: Training image, Obtained seismic data, A number of subset points

Steps:

a. Generate the first model m_1 by multi-point geostatistical simulation and evaluate its likelihood, $L(m_1) = P_{data}(d_{obs} - g(m_{1,elas}))$. The model of current state $m_c = m_1$.

b. Select r_i as an adaptive subset of points from m_c .

If the obtained spatial data is pixel-based data such as an inverted acoustic impedance in depth:

1. Build a pdf of Equation (3.5).
2. Visit a random point x and accept the point if $P_{cond}(x) > a, \forall a \in U[0,1]$.
3. Iterate above steps until the assigned number of subset points are found.

If the obtained seismic data is trace-based data such as a seismic section of seismogram in time:

1. Build a pdf of Equation (3.6).
2. Visit a random CDP x and accept random points in the CDP x if $P_{cond}(x) > a, \forall a \in U[0,1]$.
3. Iterate above steps until the assigned number of subset points are found.

c. Generate a proposal model m^* by conditional simulation using r_i as conditioning data.

d. Evaluate $L(m^*)$ and accept m^* with probability, $P_{accept} = \min(1, L(m^*)/L(m_c))$ (Metropolis et al, 1953; Mosegaard and Tarantola, 1995).

e. If m^* is accepted $m_c = m^*$, else reuse m_c .

f. Iterate b ~ e.

The adaptive selection algorithm should be modified depending on the type of spatial data. Pixel-based spatial data such as inverted acoustic impedance in depth,

inverted controlled-source electromagnetic (CSEM) data or inverted resistivity sections can be compared with predicted data directly to calculate a residual error map as shown in Figure 3.4. This is because the realizations of the earth models are simulated in the volume of pixels, and the subset of points to condition the next model is also generated from the corresponding pixels. However, if the spatial data are not in the same depth co-ordinates as the earth models (i.e. the stacked seismic traces recorded in time before impedance inversion), then direct comparison between the observed data and a forward simulated synthetic data can be misleading because of timeshifts. In this case, we propose using trace-to-trace cross-correlation coefficients to guide the probability of selection as shown in Equation (3.7).

$$P_{cond}(\mathbf{x}) = Corr(m(\mathbf{x}), d(\mathbf{x})), \quad (3.7)$$

where $m(\mathbf{x})$ is a seismogram of proposed model at \mathbf{x} line and $d(\mathbf{x})$ is a seismogram of data at \mathbf{x} line. Higher correlation coefficient assigns a higher chance to be accepted as a conditioning location for next step. For example, two seismic sections of seismograms in Figure 3.5 show similar local features at CDP 20; however, since the seismic reflections do not exactly overlap in time axis, directly subtracted residual error is still high regardless of similarity of underlying facies. Instead of using residual error calculated from pixel values, we applied cross-correlation coefficients of pairwise traces for finding more likely regions. Azevedo et al. (2012) suggested

keeping the best parts of proposed model based on correlations between data and synthetic one. However, here we propose more probabilistic perturbation using subset points from higher correlation area rather than freezing the best part for optimization.

Depending on the acceptance/rejection criterion in the Markov process, it is possible to obtain a chain of realizations aimed to characterize a certain posterior distribution with Metropolis sampling. In the studied cases discussed below, M-ASR (Approximate Metropolis sampler using ASR) yields posterior distributions reasonably close to the ones obtained by rejection sampling, but with important reduction in CPU cost. Due to the directed resampling of points ASR does not produce a reversible Markov chain and therefore is not an exact sampler. However, at every iterative step in a chain, ASR proposes a possible subset configuration which has more informative points for finding a better model efficiently. The resampling process is performed probabilistically depending on the error pdf or cross correlation coefficients. To gain practical efficiency, M-ASR can be a promising alternative sampling method to both the Metropolis sampler with ISR and rejection sampler. Through the following illustrations, we demonstrate the M-ASR efficiently approximates the posterior distribution while keeping a similar range of uncertainty as a rejection sampler.

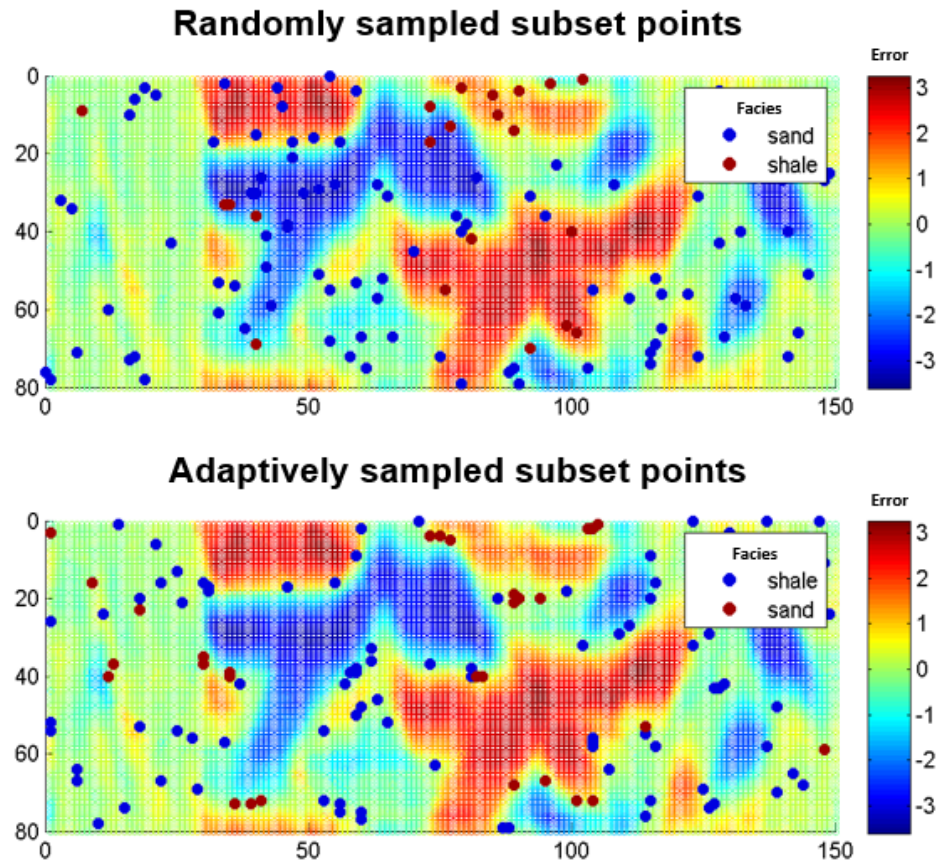


Figure 3. 4: Sampling algorithm of the subset points in ASR. The seismic attribute used here is the inverted seismic impedance. Background green zone is the low residual points while both red and blue have higher error. In the residual error map, randomly sampled points (top, ISR) are located in both low and higher error zone while adaptive sampling subsets (bottom, ASR) are located preferentially in low error zones.

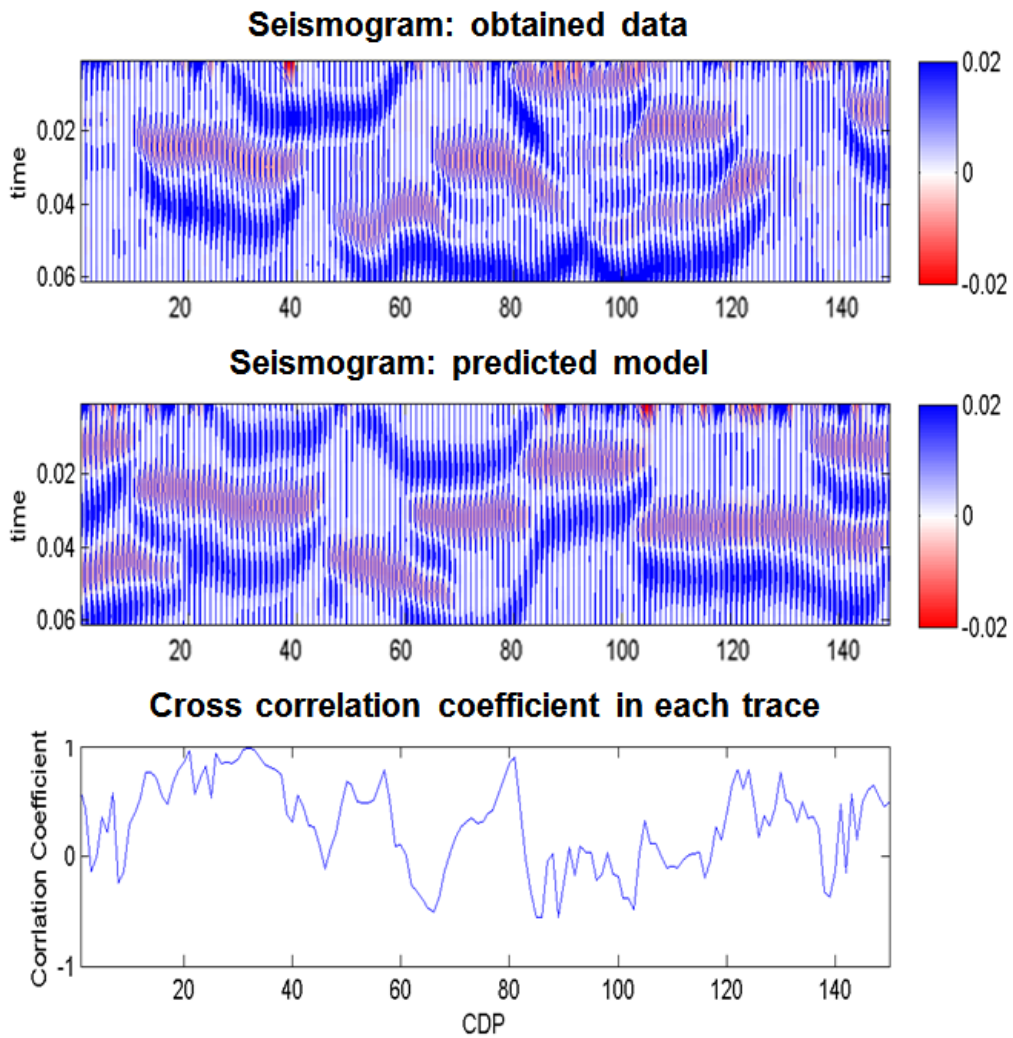


Figure 3. 5: Subset sampling algorithm for seismogram in the ASR. Since the seismogram is traces consisted of wiggles in travel time, directly subtracted variability can miss similar local feature. We used cross correlation coefficients between each trace for adaptive sampling of subset points. The location of a trace having high correlation coefficient with the corresponding data trace has more chance to be selected as subset points for conditioning the next iteration in the chain.

3.4 Application of the methodology in 2D

3.4.1 2D section examples

Synthetic 2D facies and seismic dataset are presented to demonstrate the validity of the proposed inversion technique. The two-dimensional models used were extracted from a modified version of the top layer of the Stanford VI synthetic reservoir (Castro et al., 2005). All the information about the model relevant to this work is summarized in Figure 3.6. The reference facies model is a sand-shale channel system with 80 cells in the vertical (z) direction ($dz = 1\text{m}$) and 150 cells in x ($dx = 25\text{m}$).

First, we generated multiple prior spatial models using multiple-point geostatistical algorithm (Direct Sampling) and these are used to find posterior models by rejection sampling. Rejection sampling method is one way to represent posterior pdf. Each accepted model of the rejection sampler is by definition a realization of posterior distribution. Figure 3.7 shows the results as the reference and the E-types (ensemble averages) of models. Since the hard data comes from two wells, the E-type map of priors shows its limitation of lateral resolution. Rejection sampling is accomplished to represent posterior pdf as the reference. We tested the M-ISR as an equivalent sampling method and the M-ASR as a fast approximation by comparing their results with rejection sampler. In the following sections, we introduce a sensitivity analysis of ASR parameters and three different 2D case studies. We show the use of ASR for two types of seismic data and a particular case for identifying facies not encountered in well data. The case study 1 is where we have P-impedance inverted from the seismic

section, and we use the impedance as an attribute for the stochastic lithofacies inversion. The case study 2 is where the seismic data are the normal-incidence seismograms themselves, before inversion for impedance. The case study 3 is where we try to find out a different reservoir fluid not encountered in wells by applying the Gassmann's equation (Avseth et al., 2005).

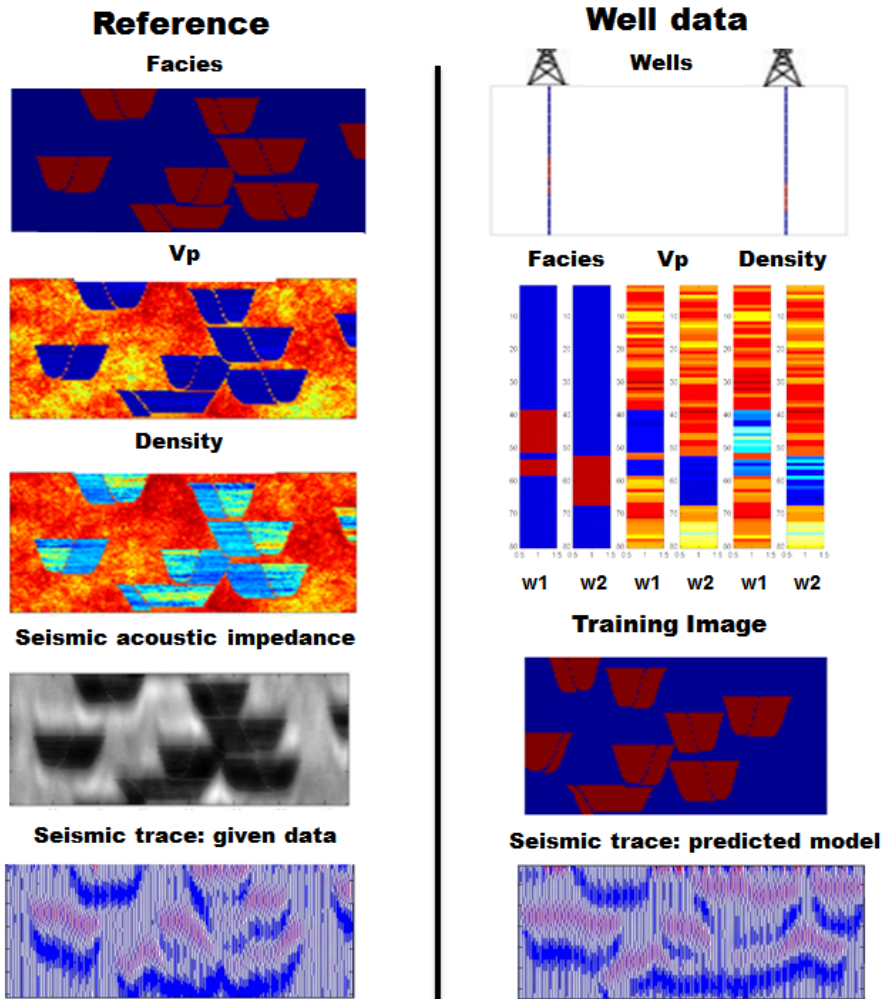


Figure 3. 6: Left: The spatial distribution of the facies, P-wave velocities (V_p) and densities (ρ) are assumed as the reference. The filtered seismic band acoustic impedance and normal-incidence seismogram are at bottom left. Right: The data of two wells are given as above and the wells are located at CDP25 and CDP125, respectively. Training image for MPS is shown at the bottom of the right column.

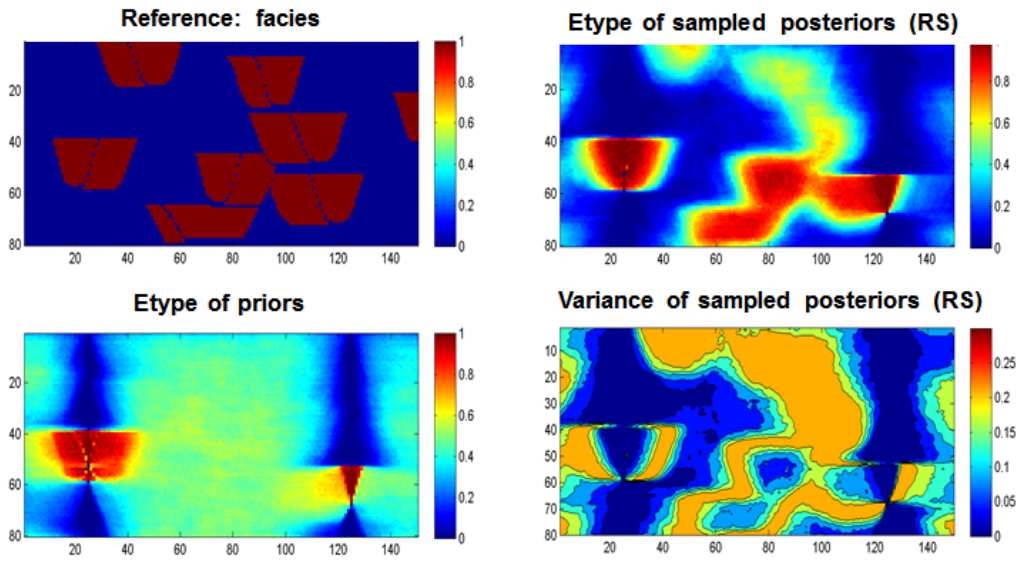


Figure 3. 7: Representation of the averages of ensembles of models. Left: (top) the reference facies and (bottom) averaged prior models. Right: (top) the E-type of rejection sampling results and (bottom) its variance.

3.4.2 Sensitivity of parameters

As shown in Mariethoz et al (2010b), the performance of ASR/ISR can be sensitive to input parameters such as fraction of selected conditioning points and number of trace locations in a seismogram section. The fraction of subset points controls iteration steps for searching the next better model. A large fraction of conditioning points makes too small a progress at every iteration step while a small fraction can move in relatively large steps but it may lose the local features of the previous model. The optimal fraction varies depending on the problems. We tested the sensitivity to this parameter and found that adaptive resampling with 1% proportion performs slightly better than the other values in the illustrated case (top, Figure 3.8). In this figure, we can find that retaining a large fraction rapidly reduces root the mean square error (RMSE) at the beginning but it gets stuck in a local minimum after 100 iterations. In contrast, chains with 1% fraction move relatively slower but can reach lower RMSE. The number of selected traces is also an important parameter for a seismic section data of seismograms. More traces account for more horizontal spatial structures while it may lose vertical information in the seismic trace since fewer points are selected per trace. In the illustration case (bottom, Figure 3.8), the number of traces affects the efficiency of the Markov chain while the fraction rate is fixed as 1%. The sensitivity test within our dataset shows 8 trace locations with 1% fraction rate are relatively suitable in this case.

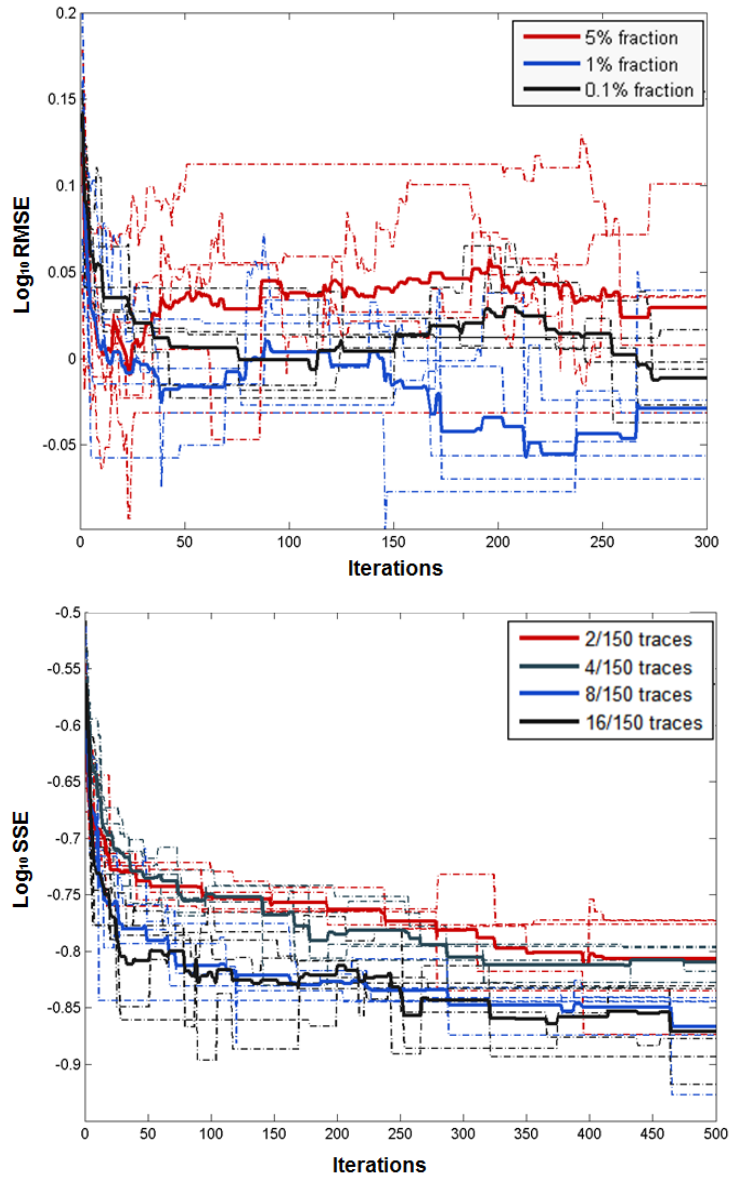


Figure 3. 8: Performance assessment for testing different parameters. A dotted line is a Markov chain and a thick line is the average of five different chains. Top: adaptive resampling with 1% fraction of conditioning subset points performs slightly better than the other values, but this can be different depending on the problem; Bottom: The sensitivity of the number of traces is tested in 2D seismic section case. 8 traces case was an ideal setting in this study.

3.4.3 Case study 1: 2D acoustic impedance inversion

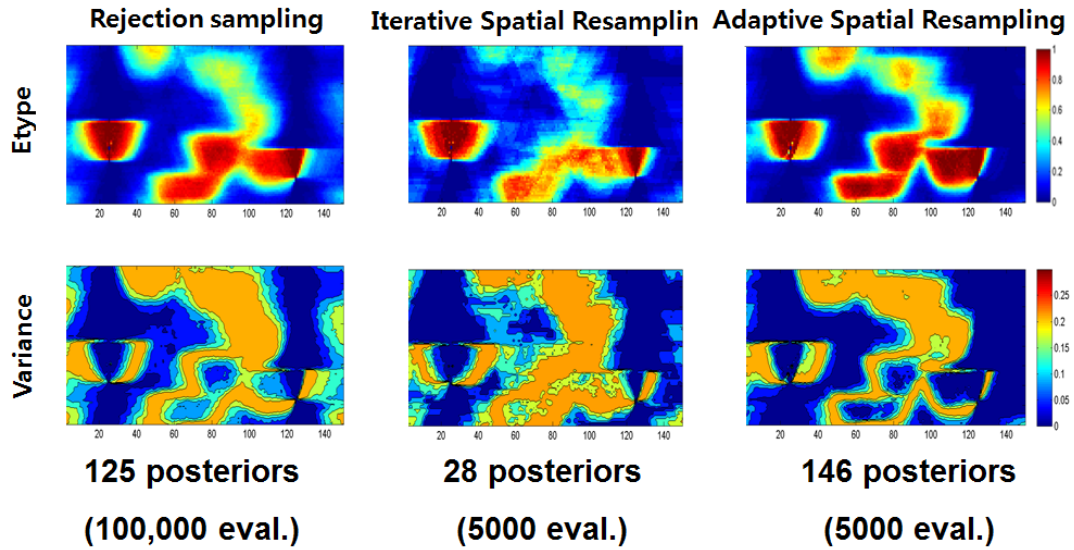
For the impedance inversion process, we assumed that we have only the 2D acoustic impedance data as the obtained seismic data, two wells with log information, and a training image. Based on a relationship between facies (reservoir property) and P-wave velocity & density (elastic properties) from the well data, Monte-Carlo simulation is performed to build a statistical rockphysics model as a bivariate pdf. Using the statistical rock physics model for the sand and shale, we compute acoustic impedance from the P-wave velocities and densities. Computation of the inverted seismic impedance is done by applying a frequency-domain Born filter for surface seismic reflection geometry with a 5~50 (Hz) bandwidth.

When we used acoustic impedance data as the seismic attribute, both rejection sampler and ASR found clear channel distributions and these results look the same while ISR found similar channel distribution with some ambiguity (first row of the Figure 3.9). However, the result of rejection sampler is the average of 125 accepted models after evaluating 100,000 prior models while ASR with Metropolis algorithm uses 5 Markov chain with 1000 iterations (146 posterior models sampled in ASR and 28 posterior models sampled in ISR). ASR shows significantly lower rejection rate when compared to ISR. The root mean square errors (RMSE) versus iterations for 5 Markov chains are shown in Figure 3.10, comparing the behavior of ISR and ASR. ASR chains reached lower error zone more rapidly than ISR chains yielding more

samples for the same number of iterations.

ISR chains also converge in the low error zone but it takes a longer time than ASR. The ASR chains move up and down rapidly and it hits many lower error models compared with ISR. Thus the averaged chain of ASR moves around the relatively lower error region than the averaged ISR chain in Figure 3.10 (thick lines). However, sampled posterior models from the ISR and ASR chains of Figure 3.10 show very similar distributions in Figure 3.11. The posterior samples are accepted after the burn-in period of ISR (100 iterations later). Sampling is performed at least 10 iterations later from the previous sample but not performed when the chain get stuck in a certain state. The histogram of ISR is distributed in slightly higher RMS error zone than ASR; however, both distributions are nearly overlapping and the median values are almost the same.

1. Acoustic impedance



2. Seismogram

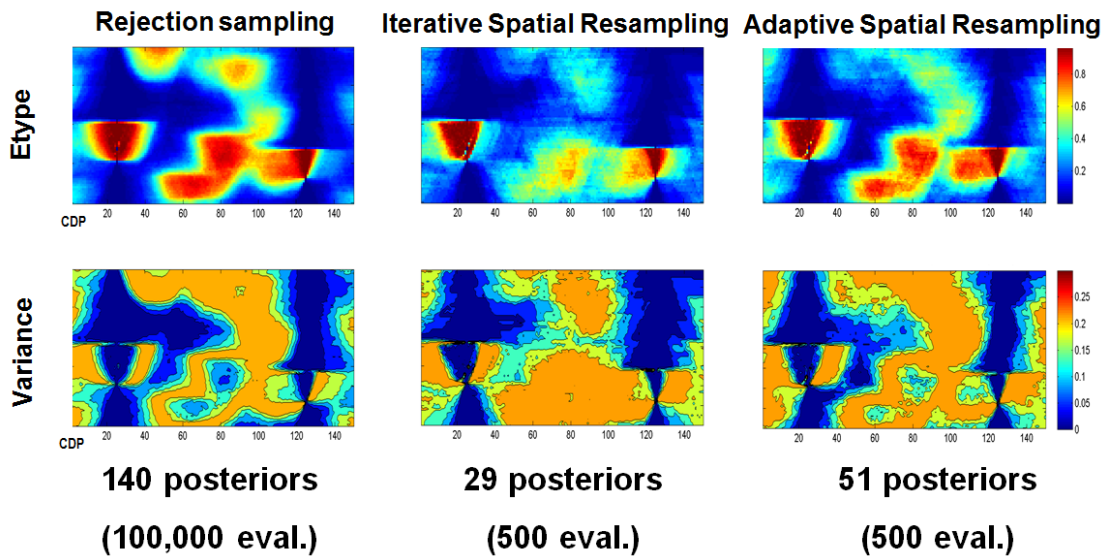


Figure 3. 9: Representation of the averages of ensembles of models. Top: (first row) the E-type of rejection sampling results, ISR and ASR using acoustic impedance as the observed seismic attribute; (second row) the variance of each algorithm, respectively. Bottom: (first row) the E-type of rejection sampler, ISR and ASR using seismogram section as the obtained data, and (second row) its variance. Within limited evaluations, ASR show

similar E-type and variance map compared with the result of rejection sampling in both cases.

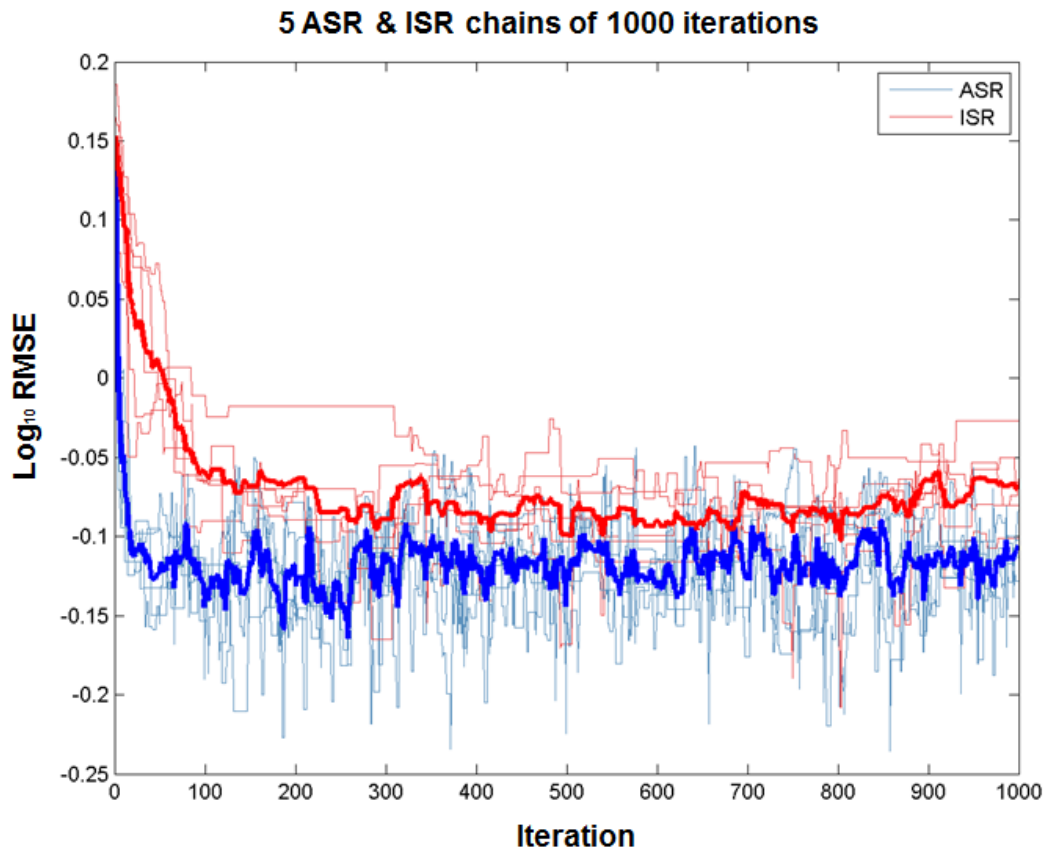


Figure 3. 10: Adaptive spatial resampling (blue curves) and iterative spatial resampling (red curves) are compared for 5 Markov chains. The average of 5 chains for each case is shown as a thick line. ASR chains reach lower error zone more rapidly.

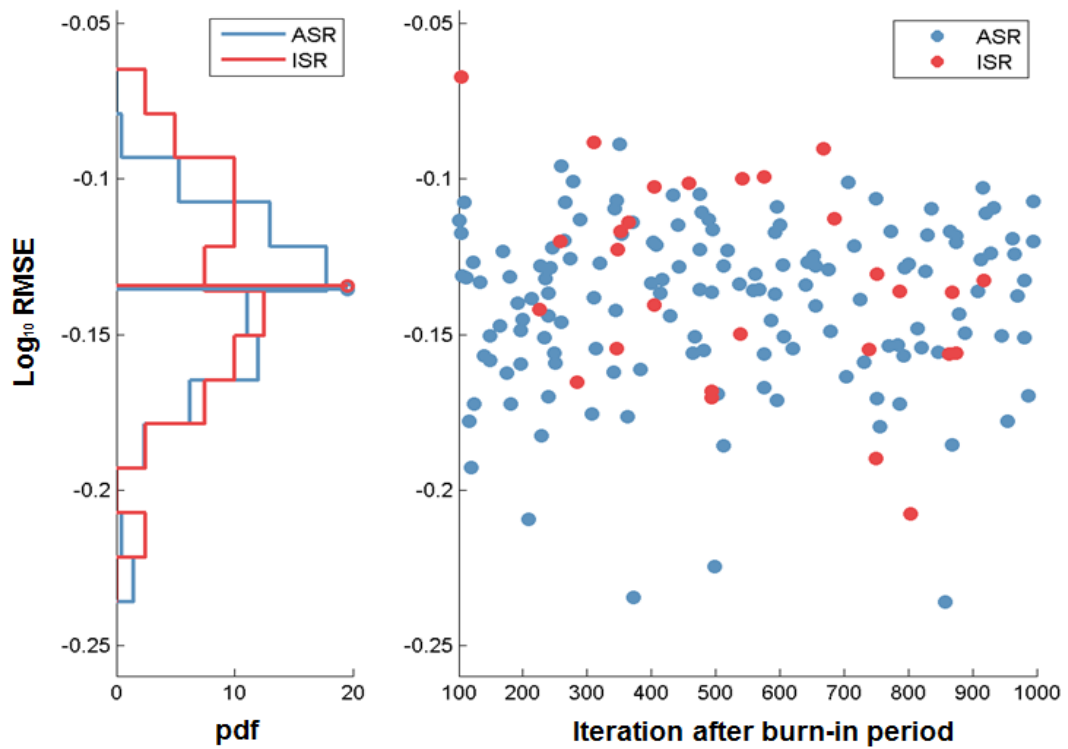


Figure 3. 11: Right: After the burn-in period of the ISR chain, posterior models are sampled from 5 ISR (red dots) and ASR (blue dots) chains, respectively. Left: Each distribution of samples is shown as histogram. The distribution of ISR is slightly higher than the ASR. However, they are nearly overlapped and the median values are almost the same in histogram.

3.4.4 Case study 2: 2D seismograms inversion

For the second case to generate a reference normal-incidence seismic section, we assumed convolutional seismic forward modeling with 10% white noise and applied a 50 (Hz) wavelet. For the inversion process, we assumed that we have only the seismogram section, two wells with log information, and a training image.

Since seismogram data have more uncertainty than acoustic impedance due to the wavelet effect and time shifts, the predictability of the sampling algorithm is critical in this case. The performance of ISR and ASR are compared in bottom of Figure 3.9, and it shows a large difference in the E-type result. ASR found similar spatial distribution of channels as the rejection sampler while ISR lost channels away from wells (ISR sampled 25 posterior models sampled in a chain). The M-ASR sampled 51 posterior models in 1 Markov chain with 500 iterations while rejection sampler accepted 140 posterior models among 100,000 priors. Variance map (bottom figures in each section of Figure 3.9) shows that ASR captures the range of uncertainty fairly well as compared with rejection sampler. Distance-based representation using multi-dimensional scaling (MDS; Scheidt et al., 2009) in Figure 3.12 also shows that the samples from M-ASR are distributed near the reference with the posterior models from rejection sampling. Thus we can conclude that the M-ASR is in this case a fair approximation of a rejection sampler. Since our reference is located away from most of the prior models, rejection sampler is inefficient to find posterior models. Sampled posterior models by M-ISR could not reach the whole posterior distribution yet due to

the limited iterations. In contrast, the similarity of the averaged ensemble map and variance between rejection sampler and the M-ASR shows that the M-ASR rapidly samples the posterior distribution approximately within the limited number of iterations

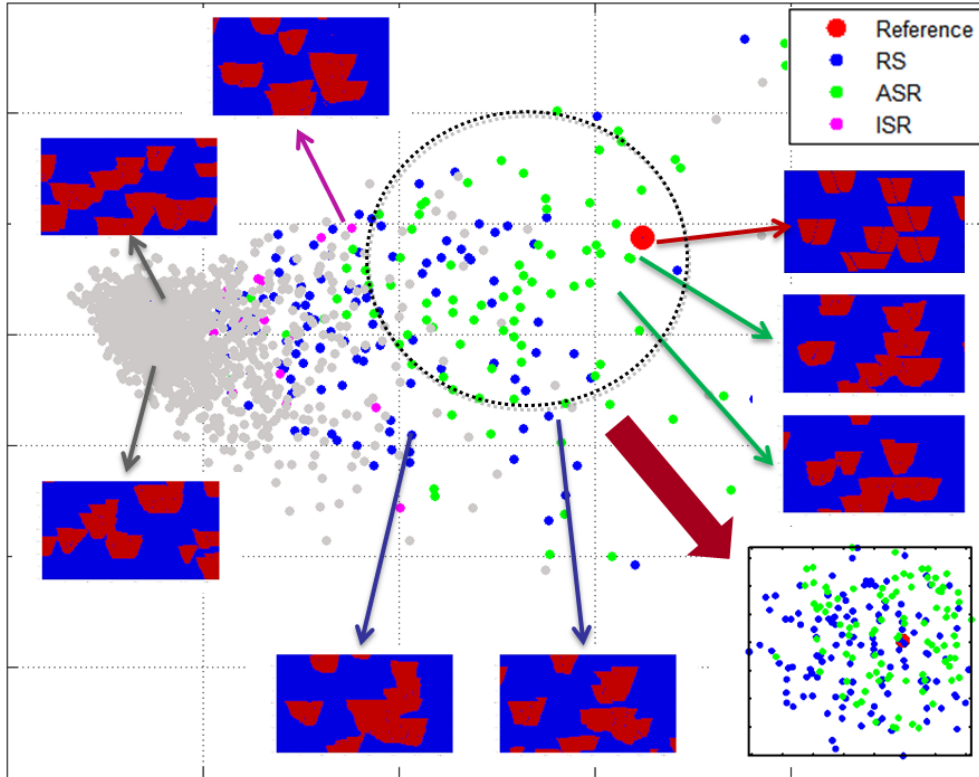


Figure 3. 12: Multi-Dimensional Scaling (MDS) projection of all models using a Euclidean pixel-wise distance. The gray points are prior models and the red point is the reference. Blue dots are the posterior models by rejection sampling. ASR and ISR results are shown by green and magenta points, respectively.

3.4.5 Case study 3: Identifying a facies not observed in wells

In this case, we assume one oil sand distribution away from the two wells locations. In this example, we have a 2D seismic section of seismograms, well logs without oil sand information, and a training image. For this task, we applied realistic rock physics relationship from actual well logs, and generated oil sand properties from the brine sand properties at the wells using Gassmann's equation (see Figure 3.13 c)). Figure 3.13 d) and e) show rejection sampler and M-ASR results as probability maps. Rejection sampler found a spatial distribution of facies close to the reference after 50,000 evaluations while M-ASR found similar distribution using one chain of 1,000 evaluations. In this more realistic setting, ASR also shows its applicability.

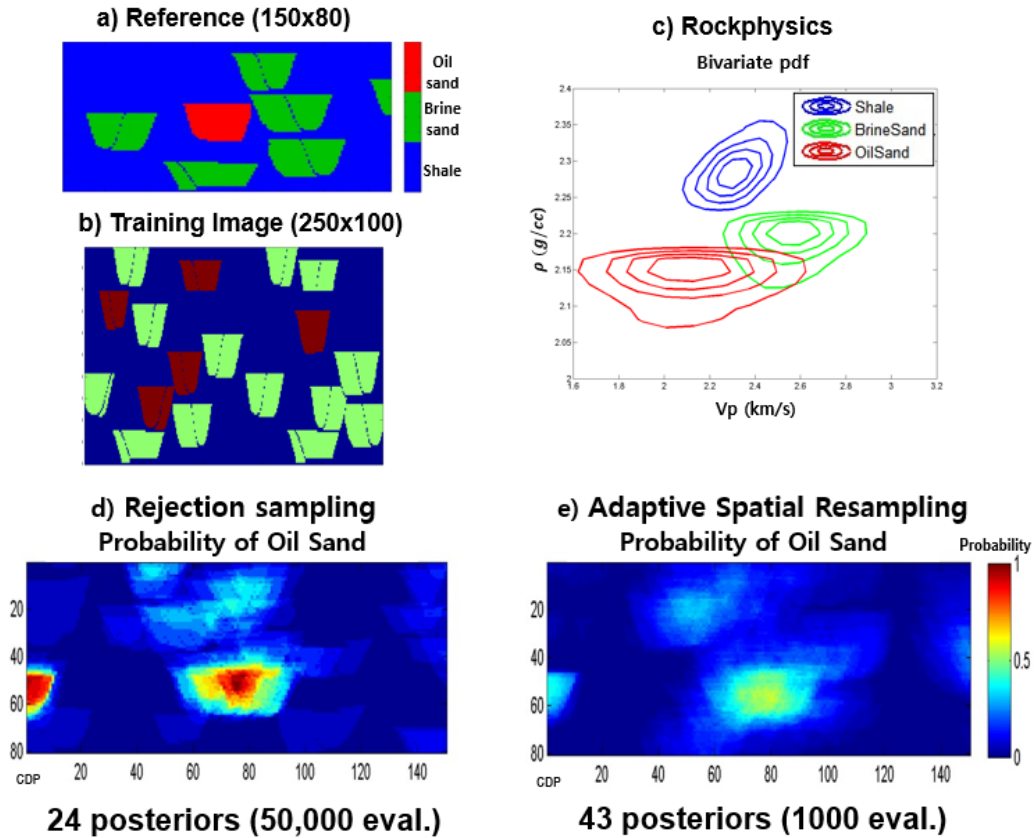


Figure 3. 13: A case study for detecting oil sand distribution away from wells, when wells do not have any oil sand: Representation of the averages of ensembles of models. a) the reference three facies, b) a training image, and c) a bivariate pdf of each facies as a rockphysics model; d) the probability maps for oil sand facies obtained from the rejection sampler and e) the probability maps of the oil sand facies obtained from the posterior models sampled by ASR. Within relatively limited evaluations, ASR shows similar probability maps compared to the result of rejection sampler.

3.5 A 3D seismic inversion compared to sequential approach

As we discussed in introduction, seismic inverse modeling can be classified as two groups such as the sequential approach and the simultaneous workflow in a Bayesian formulation. In this illustration case, we extend the proposed approach to 3D and its result is compared with a sequential approach using seismic data as soft-data to condition for geostatistical simulation (Bosch et al., 2010). The proposed approach generally takes a longer time because the seismic data is used only for falsifying models not generating models. However, this approach accounts for the elastic parameters and the reservoir properties together in a Bayesian formulation. Thus it can improve the consistency between properties and the obtained spatial data does not directly influence to prior generation. A problem setting is shown in Figure 3.14 and a probability map of the bottom right Figure 3.15 is generated by Bayes' rule in Castro et al. (2005). All the MPS input parameters are the same in both cases (see Table 3.1) and the goal is to generate 20 models from each approach. For the proposed approach, we run two parallel chains and sample 10 posterior models from each chain after the burn-in period. The result of each single realization in Figure 3.15 shows a distinctive difference in terms of reproduction of geological similarity in the given training image. Since seismic data is not used as conditioning data for model generation in the proposed workflow, it keeps geological features of training image (i.e. size of geobody, continuity, etc.) in all prior models. In contrast, the realization of sequential approach is strongly influenced by the probability map and thus it may lose some geological

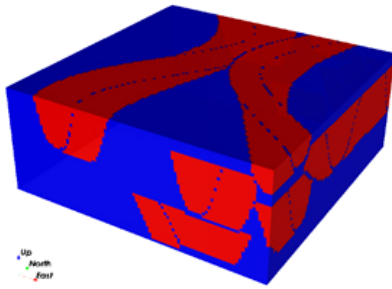
information in the training image. Compared to the reference, the averaged Etype map of the proposed workflow shows more similar and clear sand channels distribution than the results of the sequential inversion. As shown in Table 3.1, computational time is still a challenge even in ASR. However, since time consumption is mostly caused by MPS simulation, newly proposed MPS algorithms such as DISPAT (Honarkhah and Caers, 2012) and CCSIM (Tahmasebi et al., 2012) may help to speed up.

Table 3. 1: Comparison of input and output between the proposed inversion and sequential inversion.

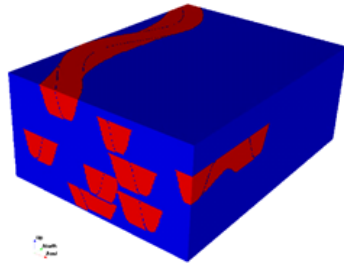
	Proposed inversion	Sequential inversion
MPS parameters	# of Nodes in Search Template : 60 Range: max 50/ med 50/ min 20 Angle: Azimuth 0/ Dip 0 / Rake 0	
Evaluations	2 chains (40 for burn-in) 280 evaluations	20 models
Computational time*	10 hours	3 hours

* 3.3GHz (4 CPUs) and 16GB RAM)

Reference: 100 x 100 x 40

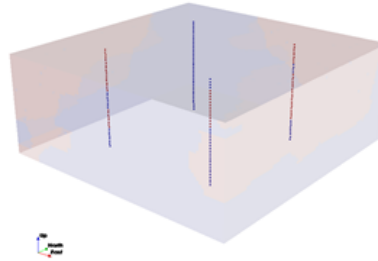


Ti: 150 x 200 x 80



Data

4 wells



3D Acoustic Impedance

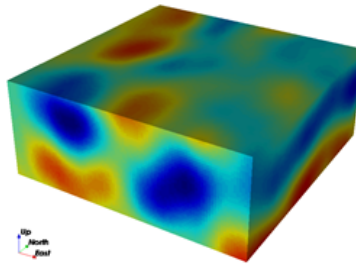


Figure 3. 14: A 3D case study for comparing sequential inversion with the proposed simultaneous inversion. Left: (top) the reference of sand and shale facies and (bottom) a training image of the first layer of the Stanford VI reservoir; Right: we have (top) 4 wells located at (25,25), (25,75), (75,25), (75,75) and (bottom) acoustic impedance data as seismic data.

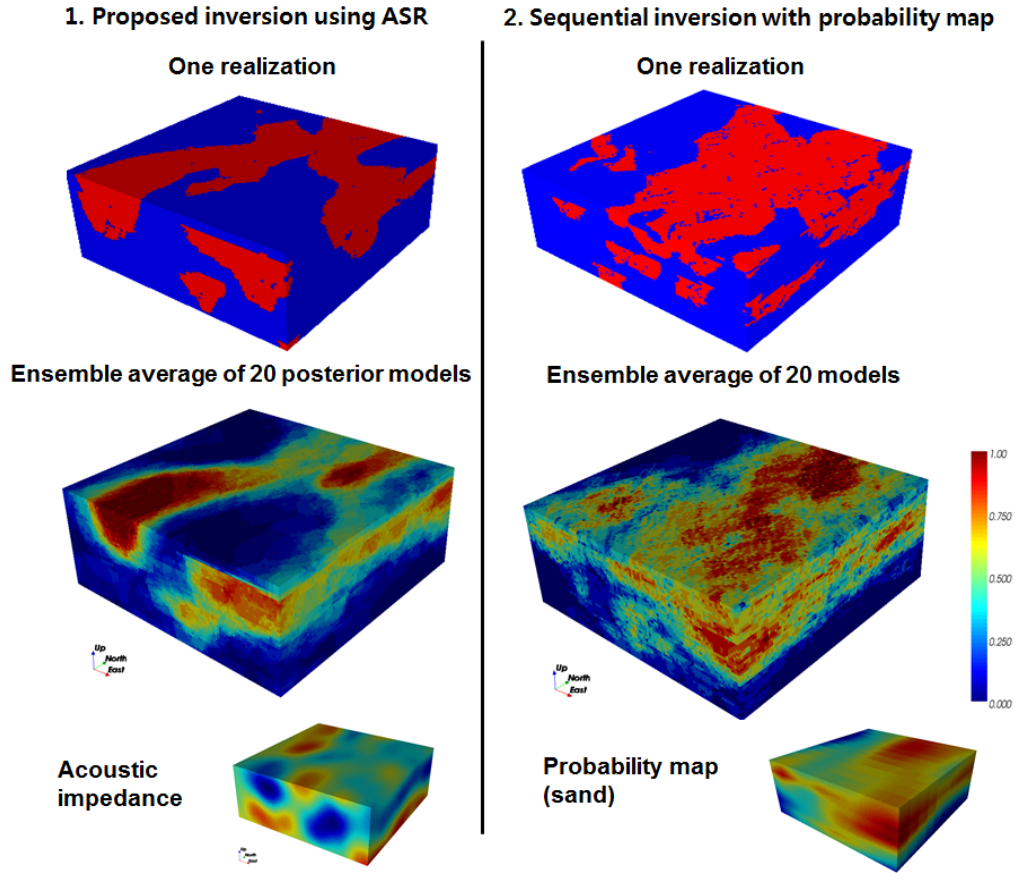


Figure 3. 15: A result of the 3D case study. Left: A set of result of the proposed simultaneous inversion using ASR; (top) a sampled posterior, (middle) an averaged Etype map of 20 posterior models, and (bottom) the given acoustic impedance. Right: A set of result of the sequential inversion using soft data; (top) a sampled posterior, (middle) an averaged Etype map of 20 posterior models, and (bottom) the sand probability map used as soft data for geostatistical simulation (Castro et al., 2005).

3.6 Conclusions

In this dissertation we presented the Adaptive Spatial Resampling method (ASR) for seismic inverse modeling, which is an improvement of the ISR method. ASR perturbs realizations of a spatially dependent variable while preserving its spatial structure. Compared to ISR, ASR accelerates the sampling efficiency. MDS plots show that both ISR and ASR have similar distribution of points with ASR showing a slight reduction in the spread. It uses the residual error at each step of the chain to guide the selection of conditioning data for the next step. In the studied cases, it yields posterior distributions reasonably close to the ones obtained by rejection samplers, with important reduction in time and computing cost. Thus ASR appears to be suitable for reservoir characterization by conditioning facies models to spatially distributed seismic data.

Depending on the acceptance/rejection criterion in the Markov process, it is possible to obtain a chain of realizations aimed to characterize a certain posterior distribution with Metropolis sampling. As a fast approximate sampler, ASR with the Metropolis sampling can be applicable in complex 3D seismic inversions. This study will be applied in actual field data as future task.

3.7 Acknowledgment

The authors thankfully acknowledge Stanford Center for Reservoir Forecasting (SCRF) sponsors.

3.8 Reference

- Andrieu, C. and J. Thoms, 2008. A tutorial on adaptive MCMC. *Stat. Comput.* 18, 343–373.
- Andrieu, C., N.De Freitas, A. Doucet, and M.I. Jordan, 2003. An introduction to MCMC for machine learning. *Machine Learning*, 50, 5-43.
- Arpat, B. G., 2005. Sequential simulation with patterns: Ph.D. dissertation. Stanford University.
- Avseth, P., T. Mukerji, and G. Mavko, 2005. Quantitative seismic interpretation applying rock physics to reduce interpretation risk: Cambridge University Press.
- Azevedo, L., R.F. Nunes, J.A. Almeida, L.M. Pinheiro, M.H. Caeiro, P.J. Correia, and A. Soares, 2012. Seismic attributes for constraining geostatistical seismic inversion. 9th International Geostatistics Congress, June 11-15, 2012, Oslo, Norway.
- Bachrach, R., 2006. Joint estimation of porosity and saturation using stochastic rock-physics modeling. *Geophysics*, 71, no. 5, O53–O63. doi: 10.1190/1.2235991.
- Bosch, M., L. Cara, J. Rodrigues, A. Navarro, and M. Diaz, 2004. The optimization

- approach to lithological tomography: Combining seismic data and petrophysics for porosity prediction. *Geophysics*, 69, 1272-1282.
- Bosch, M., T. Mukerji, and E.F. Gonzalez, 2010. Seismic inversion for reservoir properties combining statistical rock physics and geostatistics: A review. *Geophysics*, 75, no 5, 165-176.
- Castro, S, J. Caers, and T. Mukerji, 2005. The Stanford VI reservoir. 18th Annual Report, Stanford Center for Reservoir Forecasting, Stanford University.
- Contreras, A., C. Torres-Verdin, W. Chesters, K. Kvien, and T. Fasnacht, 2005. Joint stochastic inversion of 3D pre-stack seismic data and well logs for high-resolution reservoir characterization and petrophysical modeling: Application to deepwater hydrocarbon reservoirs in the central Gulf of Mexico. 75th Annual International Meeting, SEG, Expanded Abstracts, 1343–1346.
- Dubrule, O., 2003. Geostatistics for seismic data integration in earth models. SEG.
- Doyen, p. M., 2007. Seismic reservoir characterization: An earth modeling perspective. EAGE Publications.
- Eidsvik, J., P. Avseth, H. Omre, T. Mukerji, and G. Mavko, 2004. Stochastic reservoir characterization using prestack seismic data. *Geophysics*, 69, 978–993, doi: 10.1190/1.1778241.
- Gonzalez, E. F., T. Mukerji, and G. Mavko, 2008. Seismic inversion combining rock physics and multiple-point geostatistics. *Geophysics*, 73, no. 1, R11-R21.

- Griffin, J.E. and S.G. Walker, 2013. On adaptive Metropolis-Hasting methods. *Stat Comput* 23:123–134, DOI 10.1007/s11222-011-9296-2.
- Honarkhah, M. and J. Caers, 2012, Direct pattern-based simulation of non-stationary geostatistical models, *Mathematical Geosciences*, 44(6): 651-672
- Hansen, T. M., K. Mosegaard and K. C. Cordua, 2008. Using geostatistics to describe complex a priori information for inverse problems, *Proceedings from VIII International Geostatistics Congress*. Gecamin Ltd. ISBN: 978-956-8504-18-2. Mining Engineering Department, University of Chile. 1: 329-338.
- Hansen, T. M., K. C. Cordua and K. Mosegaard, 2012. Inverse problems with non-trivial priors - Efficient solution through Sequential Gibbs Sampling, *Computational Geosciences* 16(3): 593-611.
- Haario, H., E. Saksman, and J. Tamminen, 2001. An adaptive Metropolis algorithm. *Bernoulli* 7, 223–242.
- Larsen, A. L., M. Ulvmoen, H. Omre, and A. Buland, 2006. Bayesian lithology/fluid prediction and simulation on the basis of a Markov-chain prior model. *Geophysics*, 71, no. 5, R69–R78, doi: 10.1190/1.2245469.
- Mariethoz, G., P. Renard, and J. Straubhaar, 2010a. The direct sampling method to perform multiple-points geostatistical simulations. *Water Resources Research*, 46, W11536.
- Mariethoz, G., P. Renard, and J. Caers, 2010b. Bayesian inverse problem and

- optimization with iterative spatial resampling. *Water Resources research*, 46, W11530.
- Metropolis, N., et al., 1953. Equation of State Calculations by Fast Computing Machines. *Journal of Chemical Physics*, 21, 1087-1092.
- Mosegaard, K., and A. Tarantola, 1995. Monte Carlo sampling of solutions to inverse problems. *Journal of Geophysical Research*, 100(B7), 12, 431-412, 447.
- Mukerji, T., P. Avseth, and G. Mavko, I. Takahashi, and E. F. Gonzalez, 2001a. Statistical rock physics: Combining rock physics, information theory, and geostatistics to reduce uncertainty in seismic reservoir characterization. *The Leading Edge*, 20, no. 3, 313-319.
- Mukerji, T., A. Jorstad, P. Avseth, G. Mavko, and J. R. Granli, 2001b. Mapping lithofacies and pore-fluid probabilities in a North Sea reservoir: Seismic inversions and statistical rock physics. *Geophysics*, 66, 988-1001.
- Mukerji, T., Mavko, G., and Rio, P., 1997, Scales of reservoir heterogeneities and impact of seismic resolution on geostatistical integration, *Mathematical Geology*, v. 29, no. 7, p. 933–950.
- Tahmasebi, P., A. Hezarkhani, M. Sahimi, 2012. Multiple-point geostatistical modeling based on the cross-correlation functions, *Computational Geosciences*, 16:779–797, DOI 10.1007/s10596-012-9287-1
- Roberts, G.O., and J.S. Rosenthal, 2009. Examples of adaptive MCMC. *J. Comput.*

Graph. Stat. 18, 349–367.

Scheidt, C., & Caers, J., 2009. Representing spatial uncertainty using distances and kernels. *Mathematical Geosciences*, 41(4), 397-419.

Strebelle, S. B., and A. G. Journel, 2001. Reservoir modeling using multiple point statistics. *Society of Petroleum Engineers*, 71324.

Tarantola, A., 1987. *Inverse problem theory: Methods for data fitting and model parameter estimation*. Elsevier Scientific Publ. Co., Inc.

Tarantola, A., 2005. *Inverse problem theory and methods for model parameter estimation*. SIAM.

Ulvmoen, M. and H. Omre, 2010. Improved resolution in Bayesian lithology/fluid inversion from prestack seismic data and well observations: Part 1— Methodology, *Geophysics* 75(2), p.R21-R35.

Chapter 4

Field Application to a Channelized Turbidite Reservoir in Equatorial Guinea, West Africa

*“We can't solve problems by using the same kind of thinking
we used when we created them.”*

- Albert Einstein

4.1 Abstract

Traditional seismic inversion approaches have focused on reducing errors between the data and the model within a fixed geological scenario. The problem with this approach is that it either ignores uncertainty related to geological interpretation or requires repeating inversion for each scenario. In this dissertation we propose to

estimate the probability of all available scenarios with the given observed data first, by using pattern similarity between seismic data and forward simulated models.

The proposed workflow is applied to an actual channelized turbidite reservoir with 3D seismic data with various geological scenarios. The geological scenarios include rockphysics uncertainty, geometry uncertainty, and spatial distribution uncertainty. In this dissertation we provide a practical recipe for applying the proposed workflow to actual reservoir modeling. From studying well data to modeling reservoir geobodies, all significant geological variations will be discussed and modeled. Then the resulting distance matrix, calculated from pattern similarity algorithms, is projected in multi-dimensional scaling (MDS) space to sort out the more likely from the less likely scenarios with given data.

4.2 Introduction

A field in the early development stage has very limited data: a little well data, seismic data, and some geological observations. Reservoir forecasting in this stage is one of the most important tasks for future decision making, and modeling spatial variation based on geological observations and seismic data is a key challenge. However, seismic inversions often fail to converge while finding the best fit model within time and cost because the applied geological scenario is wrong. Even worse, we often have to discard the previously matched models due to a discrepancy with newly obtained data. The discrepancy is mainly caused by a too narrow range of uncertainty

as a result of an incorrect but fixed geological scenario. Thus, modeling geological scenarios is an essential step before matching data in seismic inversion. To do this we have to consider various sources of geological uncertainty such as geometry uncertainty, spatial distribution uncertainty, and rockphysics uncertainty.

This dissertation focuses on how to test a wide range of geological scenarios from the obtained seismic data. We propose a pattern-based procedure for estimating the probability of each scenario based on seismic data. As discussed in Chapter 2, to compute the distances, we applied pattern similarity algorithms such as Multiple Point Histogram (MPH, Deutsch and Gringarten, 2000; Lange et al., 2012) and Discrete Wavelet Transform (DWT, Chui, 1992; Daubechies, 1992; Mallat, 1999) for converting seismic data into a histogram of patterns. Next, a Jensen-Shannon (JS) divergence algorithm (Kullback, 1983; Cover and Thomas, 1991; Endres and Schindelin, 2003) is applied to calculate the distance between two frequency distributions. Lastly, the distances are projected in a Multi-Dimensional Scaling (MDS, Borg & Groenen, 1997; Caers, 2011) map for estimating the probability of each scenario given data. As a result, we can determine more likely geological scenarios or more promising geological parameters which are close to the data in the MDS map.

Through this chapter we provide a practical recipe for applying the proposed workflow to actual reservoir modeling. A turbidite reservoir in Equatorial Guinea, West Africa is used for verification of the workflow, and the study starts from the beginning stage of reservoir modeling. Based on a few well logs from one well, a

rockphysics relationship is established which links reservoir property (facies) and elastic properties (P-velocity and density), and it is used for a seismic forward simulation. After modeling a target canyon in seismic resolution, the geological scenarios are modeled to identify the more important geological parameters via sensitivity analysis, and to assess more promising scenarios. With the final results, modelers can provide a set of models constrained to well data, seismic data, and geological scenario uncertainty.

4.3 Methodology

4.4 Field application

4.3.1 Seismic inversion in a Bayesian framework integrating seismic data and geological scenario uncertainty

One of geomodelers' ultimate goals is to create reservoir models by integrating geological scenarios and obtained data. In a Bayesian framework we can formulate these relationship as equation (4.1):

$$P(m_{res}, S|d) = \sum_k P(m_{res} | S_k, d) P(S_k|d) \quad (4.1)$$

S_k is the k -th scenario, $P(S_k|d)$ is the posterior probability of each geological

scenario given data, $P(m_{res}|S_k, d)$ is the data-likelihood given the k -th scenario and models, and the final posterior probability is calculated by summing all the likelihood values for each scenario. In this dissertation we discuss about quantifying $P(S_k|d)$ in chapter 2, and have studied about sampling the posterior distribution within the given data and a geological scenario ($P(m_{res}|S_k, d)$) in chapter 3. For a field application, an experimental design to setup a number of geological scenarios (i.e. $S_k, \forall k = 1, \dots, n$) is often inefficient because the number of scenarios are drastically increased with a wide range of geological uncertainty. Thus using a continuous range of parameters is necessary. To build geometry uncertainty and spatial uncertainty as a part of geological uncertainty, we sampled all parameters from each uniform distribution. A model which is built from the sampled geological parameters represents a geological scenario in this study.

In Equation (2.2) and (2.3), we propose a distance-based approximation method for estimating $P(d|S_k)$. The samples in the MDS map represent forward simulated seismic responses from each model. From the samples of each scenario, we generate the probability density function of the scenario k , and use the pdf for estimating $f(X|S_k)$.

To project distances between models and data in a MDS map, we have to build a distance matrix. Since seismic data is a 2D or 3D image response, a big challenge is how to define distances between the seismic images. Traditional Euclidean distance is not appropriate for our goal, because we are interested in patterns of seismic response

influenced by various geologic parameters, not the specific locations of geobodies in seismic data. Therefore the key issues are how to capture the patterns in seismic responses and how to define differences between them. To do this we applied pattern similarity algorithms such as MPH or DWT for comparing patterns in seismic responses, and Jensen-Shannon divergence for defining the distance between two seismic responses. The proposed workflow details about pattern similarity algorithms are described in Chapter 2.

4.4.1 Field introduction

As an actual field case study, we applied the proposed workflow to a channelized turbidite reservoir. It is deposited in offshore Equatorial Guinea, West Africa. Figure 4.1 shows the location of the study area. The dataset includes a full-stack seismic cube, digital core images, a pilot well which penetrates the middle of the seismic cube and encounters oil reservoirs, and some relevant geology studies on this site. Based on core observations, Lowe (2004) confirms that fining upward signals on well logs of the study area confirms channelized turbidite deposition in submarine canyons. Daily et al. (2002) point out that the sandstones in this area were deposited within the submarine canyons. Thus we can infer from these studies that our target reservoirs may be channelized turbidite infill canyons. Generally submarine canyons are important containers or conduits of coarse sediments, and these stacked turbidite canyon fills often constitute significant petroleum reservoirs (Anderson et al., 2006;

Normak and Carlson, 2003).

Figure 4.2 shows our interpretation of the present-day seafloor, mapped from 3D full-stack seismic data. Jobe et al. (2011) have studied a location in the Benito and Mitemele rivers in Equatorial Guinea (covering our dataset location) and recognize two types of submarine canyons (Type I and Type II) from seafloor data. Based on the seafloor data, the study area is more likely classified as a Type II canyon. However, it is hard to conclude which type of canyon is in our target zone as it's 1000m deep. The more important task is to model the submarine canyon as a conduit of sediments and a container of channelized reservoirs.

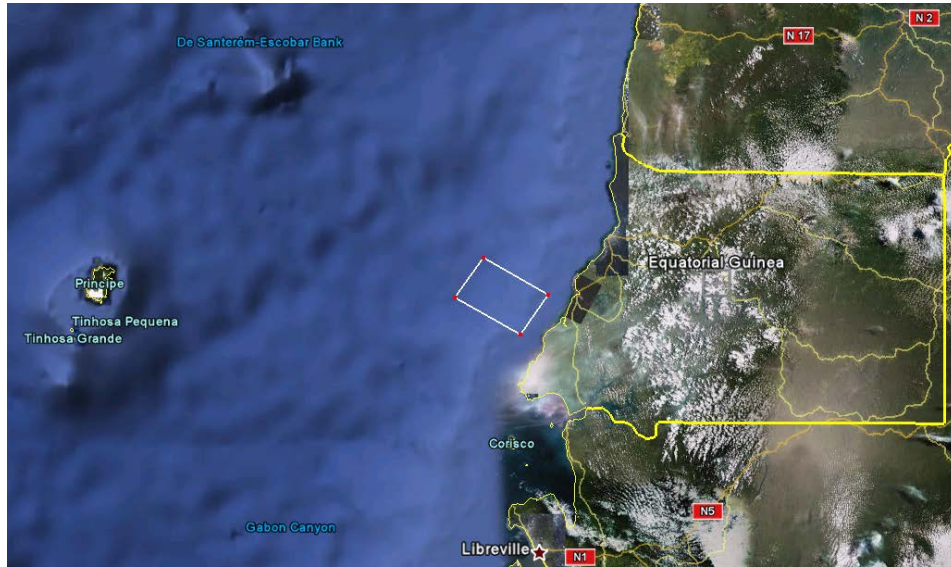


Figure 4. 1: Location of the study area (white rectangle) in offshore Equatorial Guinea, West Africa.

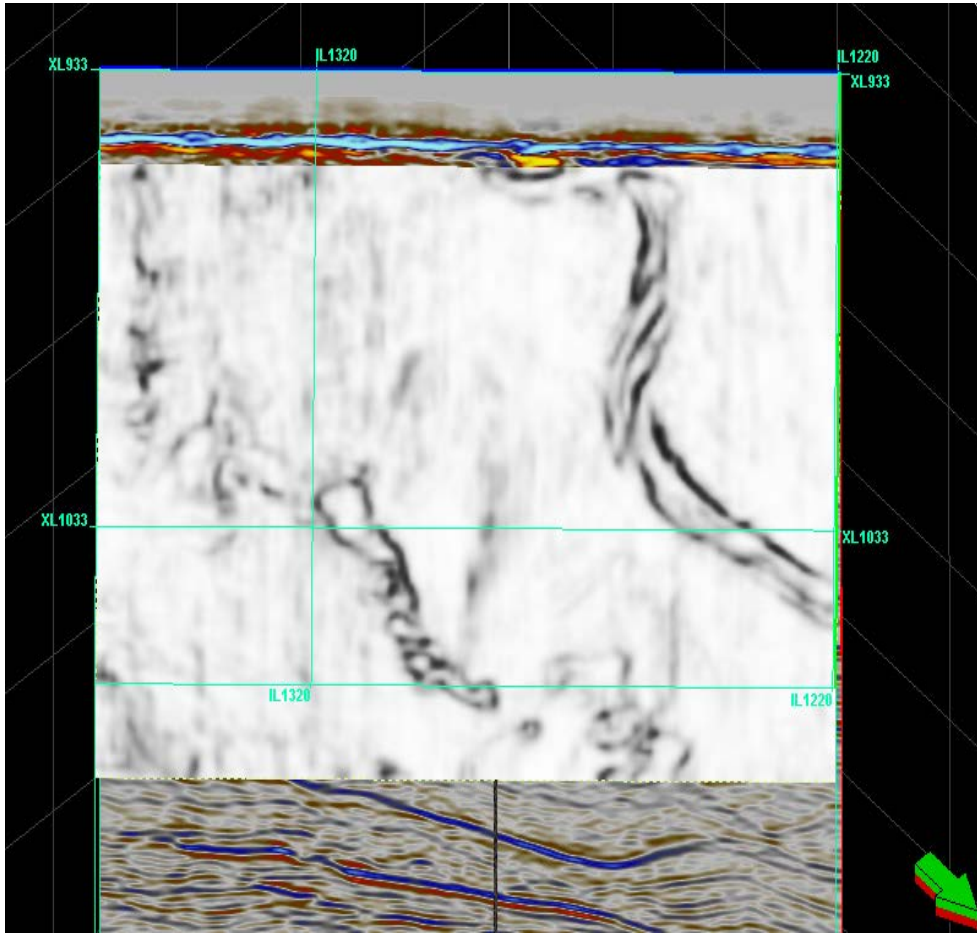


Figure 4. 2: Present-day seafloor map interpreted from 3D seismic data.

4.4.2 Modeling a submarine canyon

In seismic resolution, we can model the submarine canyon as a container. Along with the distinctive seismic reflections, the top and base surfaces are modeled in Figure 4.3. Note that the top and bottom surfaces are not generated from only the two slices shown in Figure 4.3, but from interpretation of all the 2D seismic sections. As a result, a submarine canyon is built in the target zone (see Figure 4.4). Figure 4.5 shows a thickness map between the top and base surfaces, and the blue and purple region can be interpreted as a main submarine canyon. Since the ultimate goal of this dissertation is to model geological uncertainty from seismic data, it focuses on uncertainty in sub-seismic resolution of the submarine canyon inside. To model infill geobodies inside the canyon, we cut the canyon into the target grid (black rectangle) shown in Figure 4.6. The original seismic cube in the target zone was 135 x 142 x 100 cells (3.375km x 3.55km x 100m), and the target grid is built of 90 x 40 x 100 cells (2.25km x 1km x 100m).

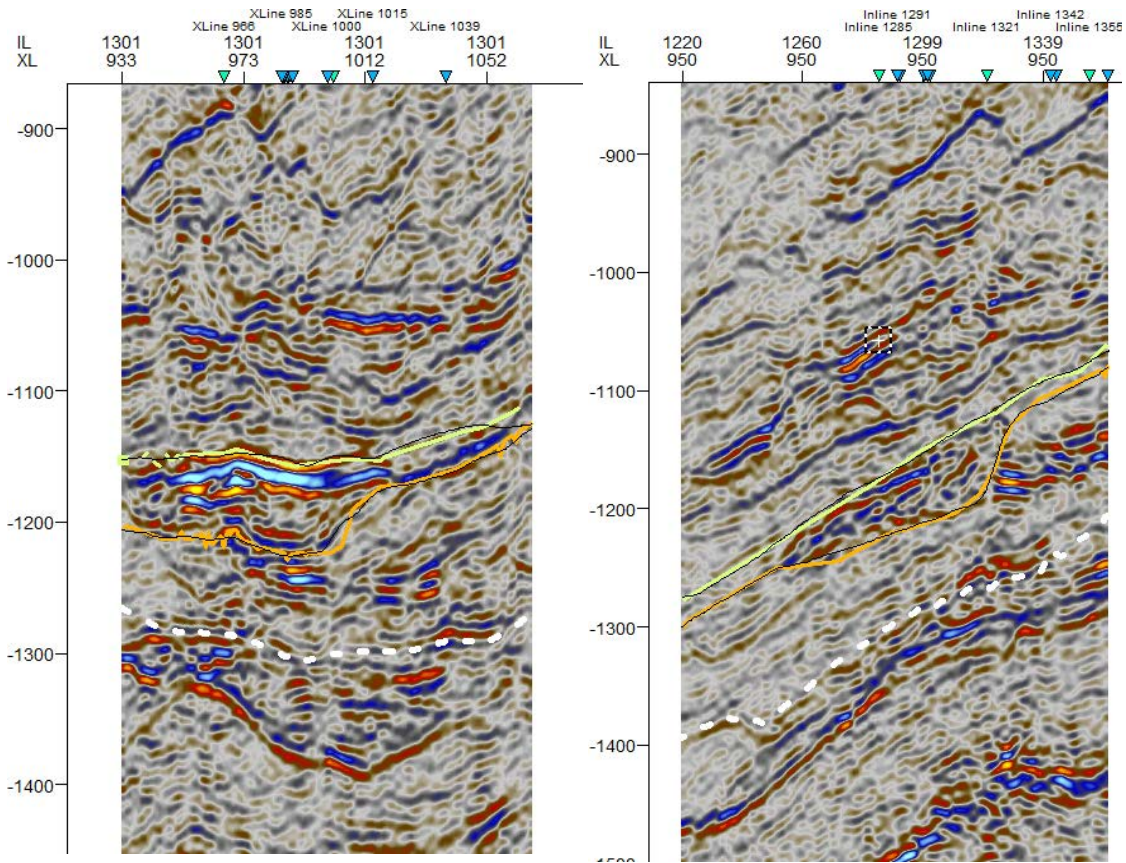


Figure 4. 3: 2D seismic sections from Inline 1301 (left) and Xline 950 (right) for modeling the top (green line) and base (orange line) surfaces. Along the distinctive seismic reflections, both surfaces are interpreted.

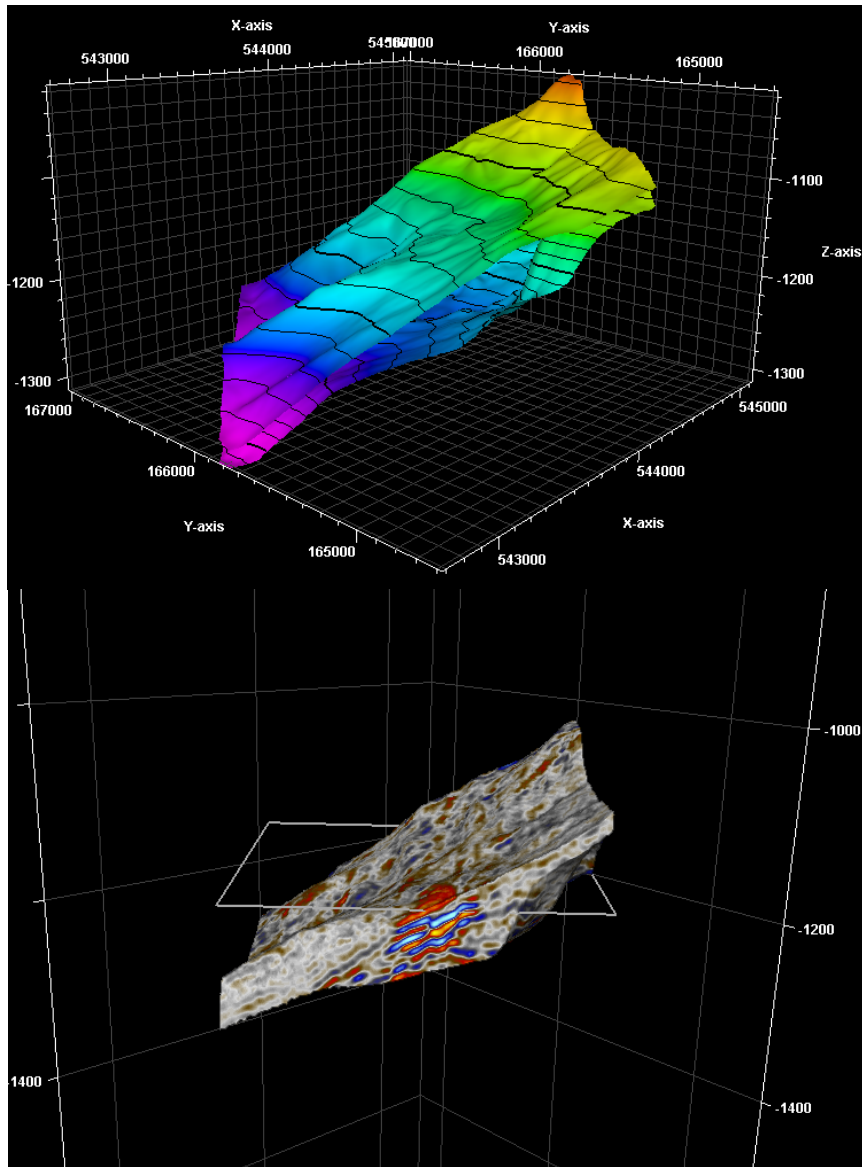


Figure 4. 4: A modeled submarine canyon. Top: The top and base surfaces are shown with their topography in TWT. Bottom: the seismic amplitudes (bottom picture) are extracted along the canyon boundary. Seismic reflections inside of the canyon show mixed responses of infill geobodies.

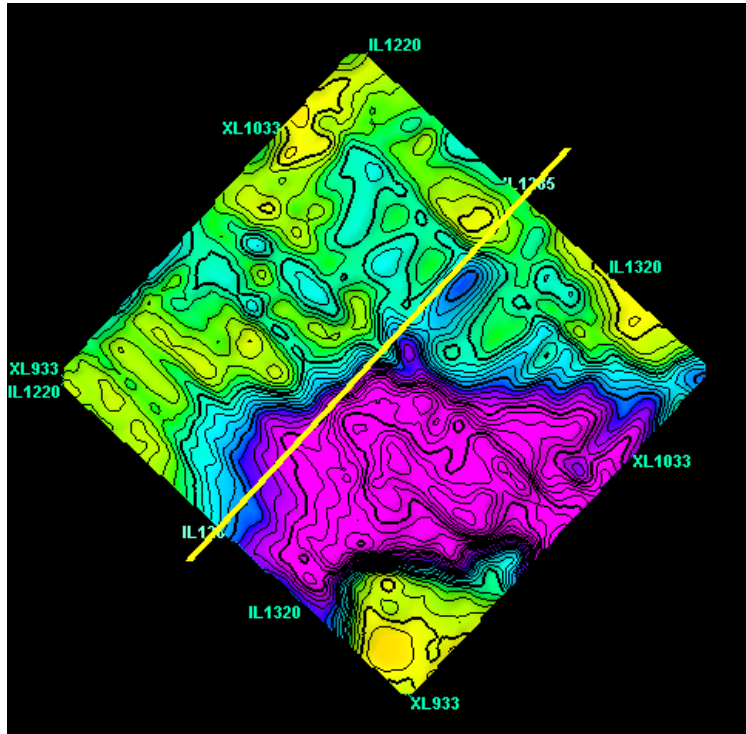


Figure 4. 5: A thickness map between the top and base surfaces. The contour map, colored in blue and purple, shows the target canyon from the right corner to the left center.

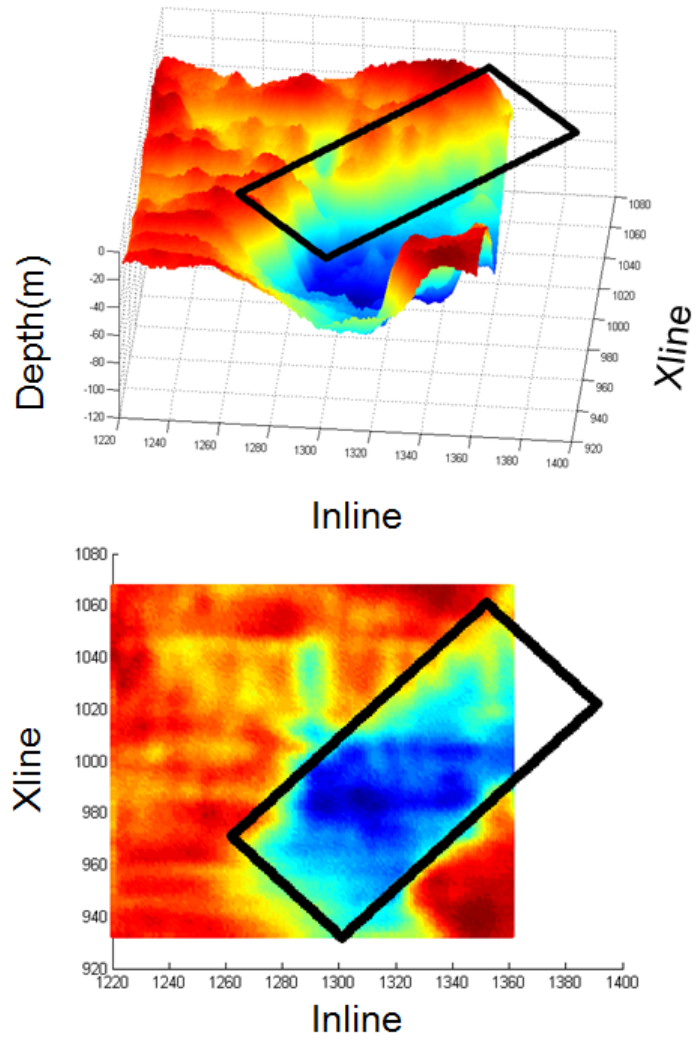


Figure 4. 6: Thickness map in 3D (top) and 2D (bottom). The black rectangle is the target grid for modeling infill geological scenarios.

4.5 Defining geological scenario uncertainty

4.5.1 Hierarchy of geological scenario uncertainty

We establish a hierarchy of geological scenarios from seismic resolution to sub-seismic resolution, as summarized in Figure 4.7. In seismic resolution, we build a submarine canyon as a container, and next we model infill geological scenarios for sub-seismic resolution. Note that vertical seismic resolution in this field is about 10m. Below the seismic resolution limits, thin and small geobodies are not clearly detectable. Thus we propose a workflow to build a set of geological scenarios and test them using a pattern similarity technique. The goal of this workflow is to sort the uncertain geological scenarios into more likely and less likely ones. All significant geological scenarios get started from ‘What-if’ ideas based on the obtained data, previous geological observation and possible geological concepts.

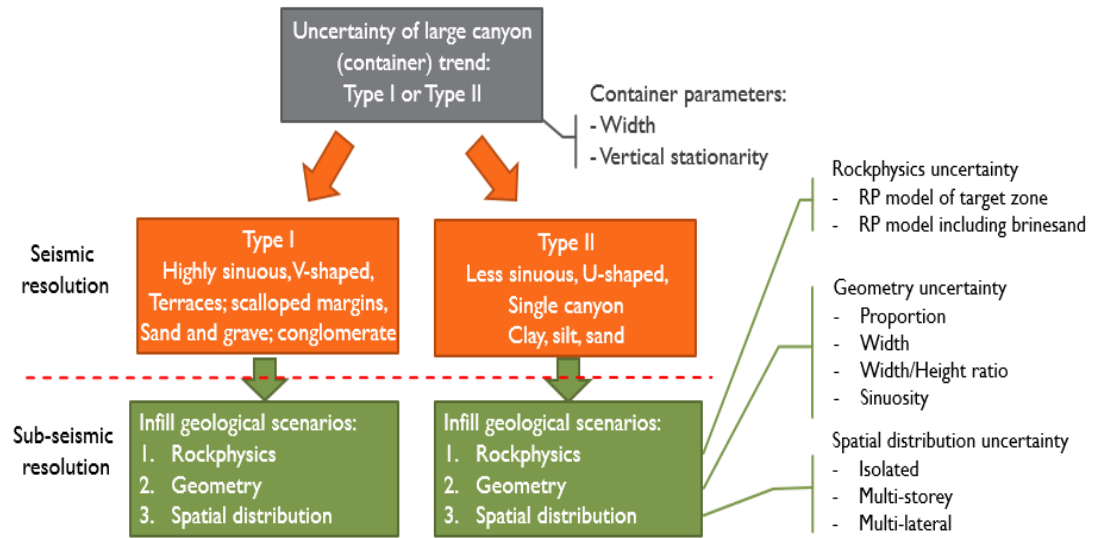


Figure 4. 7: A diagram of geological scenario uncertainty hierarchy.

4.5.2 Rockphysics uncertainty

Rock Physics (RP) models which link the reservoir property (facies) and elastic properties (P-wave velocity, S-wave velocity, and density) are the first key step for seismic forward simulation. If we use an incorrect rockphysics relationship, final models having similar seismic responses may predict completely different facies than the real facies. Therefore, establishing a correct relationship between facies and elastic properties based on the obtained well logs is an essential process in actual fields. In Figure 4.8, well X has various well log data, which shows that we have oil sand distribution in the well. From 1055m to 1080m in the target zone (marked as red circles), the facies has low Gamma Ray (GR) values and high resistivity (R) log values,

which are typically good signatures of oil sand. Based on well logs such as GR, Resistivity (AHT10 and AHT90), V_p (1/DTCO), V_s (1/DTSM), Density (RHOZ), Porosity (Phie), and V_p/V_s ratio, K-means clustering classifies the target zone from 1050m to 1150m (100m) as the three facies shown in Figure 4.9 (a). Digital core images confirm the existence of the facies in the well, and we can use this model as the first possible rockphysics relationship in the target zone. Further away from the well, the target zone may have different reservoir fluids such as water instead of oil. Below the oil water contact (OWC, thick blue line), we can find water sand (or brine sand) distribution (marked as blue circles in Figure 4.8), and we can use this to predict the brinesand distribution away from the well. Figure 4.9 (b) shows the second rockphysics relationship including the brine sand information.

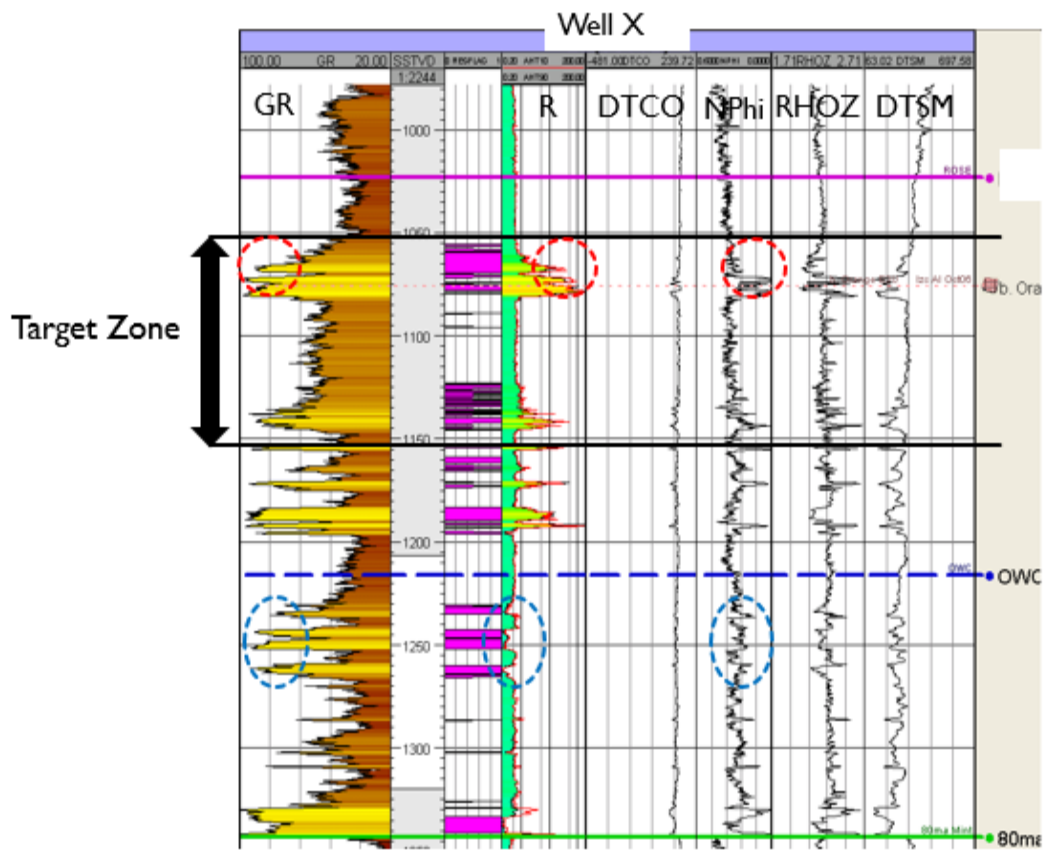


Figure 4. 8: Multiple well log data from well X. Well X is located in the middle of the target grid and encounters oil sand while drilling. In well X, the target zone from 1050m to 1150m (100m deep) is marked by black lines.

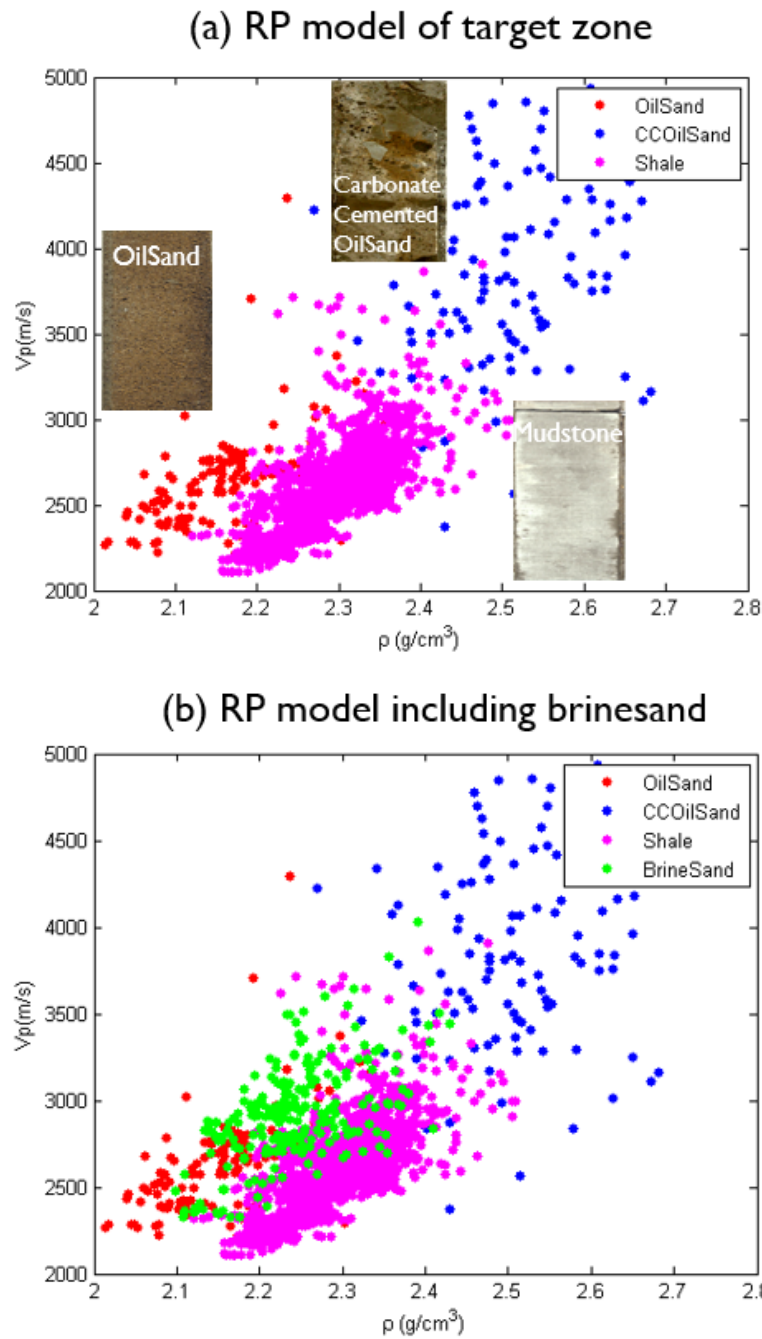


Figure 4. 9: (a) Rockphysics relationship generated from well X in the target zone. Oilsand (marked by red), Carbonate-Cemented Oilsand (CCOilSand, marked by blue), and Shale (marked by magenta) facies are classified from well log information. (b) Rockphysics

relationships, including Brinesand distribution (marked by green). Brinesand distribution is obtained via water sand below the oil-water-contact line in well X. This second rockphysics model is prepared for geological scenarios having brinesand distributions away from the well.

4.5.3 Geometry uncertainty

Geometry uncertainty includes all significant geobody parameters. Mayall et al. (2006) summarized several key elements of turbidite channel reservoirs, such as variability of sinuosity, proportion (NtoG ratio), width, depth, and stacking patterns. Based on geological observation in this field, we focus on channel geometry, which includes proportion, width, width/height ratio, and sinuosity. Note that all the geometry parameters are sampled from a continuous uniform distribution instead of assigning discrete values from an experimental design.

Since the facies proportion highly depends on the local facies distribution, analogous study may not be sufficient to determine a range of proportion. To guide the proportion of each facies, we applied a Naïve Bayes classifier in the inverted P-impedance cube. The P-impedance cube is inverted from full stack seismic data by using model-based inversion in Hampson & Russell Software (HRS). Since impedance histograms of each facies are overlapped on each other, and the inverted impedance is also a model-based interpretation result, these classification results are very uncertain and unstable. However, they are useful to guide the proportion of each facies. Figure 4.10 shows a classification result from each rockphysics model. In RP model 1, oil sand was 32% and carbonate-cemented oil sand was 6%, while the remaining background shale was 62%. In RP model 2, brine sand facies is added and it occupies 37% of the total proportion. Oil sand and carbonate-cemented oil sand distribution are 32% and 3%, respectively. Due to the brine sand proportion, shale

fraction has decreased to 28%. According to this classification result, we set up a range of proportions depending on each facies, as summarized in Table 1 (low and high boundaries for each rockphysics model are displayed). Figure 4.11 shows an example of RP 1 and RP 2, respectively. The RP 1 example in Figure 4.11(a) is generated from a 10% proportion of oil sand and 3% proportion of carbonate-cemented sand. This combination is the lowest setting for both oil sand and carbonate-cemented sand. The RP 2 example in Figure 4.11(b) shows the largest proportion setting for all three sand facies: 25% for oil sand, 10% for carbonate-cemented oil sand, and 25% for brine sand.

The size of the geobody is also an important geometry parameter. Abreu et al, (2003) and Mayall et al. (2002) note that slope turbidite channels in West Africa are typically classified as one of two types of channels. Large Channels are typically 1-3km wide, 50-200m thick, confined by an erosional base, and comprising multiple stacked smaller channels and small infill channels stacked in a series of high net to gross channels, each of which are typically 100m-500m wide and 1-10m thick. In this dissertation, we tested width parameter as a range value sampled from 1/8 to 1/4 of the canyon width (i.e. 125m – 250m), and width/height ratio sampled from 0.5 to 1.5 (it varies from 2.5m to 15m deep). Some examples are shown in Figure 4.12.

The last key parameter for geometry uncertainty is sinuosity. Most turbidite channels are very sinuous, and a difference in sinuosity can affect the distribution of reservoir facies. We can easily observe the sinuosity in our study area from the

seafloor image in Figure 4.2. The sinuosity can be modeled by the wavelength of the sinusoids. Figure 4.13 shows a range of sinuosity variation from 200m to 50m wavelengths. In general, sinuosity arises from several very complex geological parameters, influenced by the larger scale bending in the canyon and the stacking patterns of channels (Beydoun et al., 2002; Kolla et al., 2001). However, in this dissertation, we assume the variation in sinuosity is controlled by wavelength values, generated from a uniform distribution from 50 to 200.

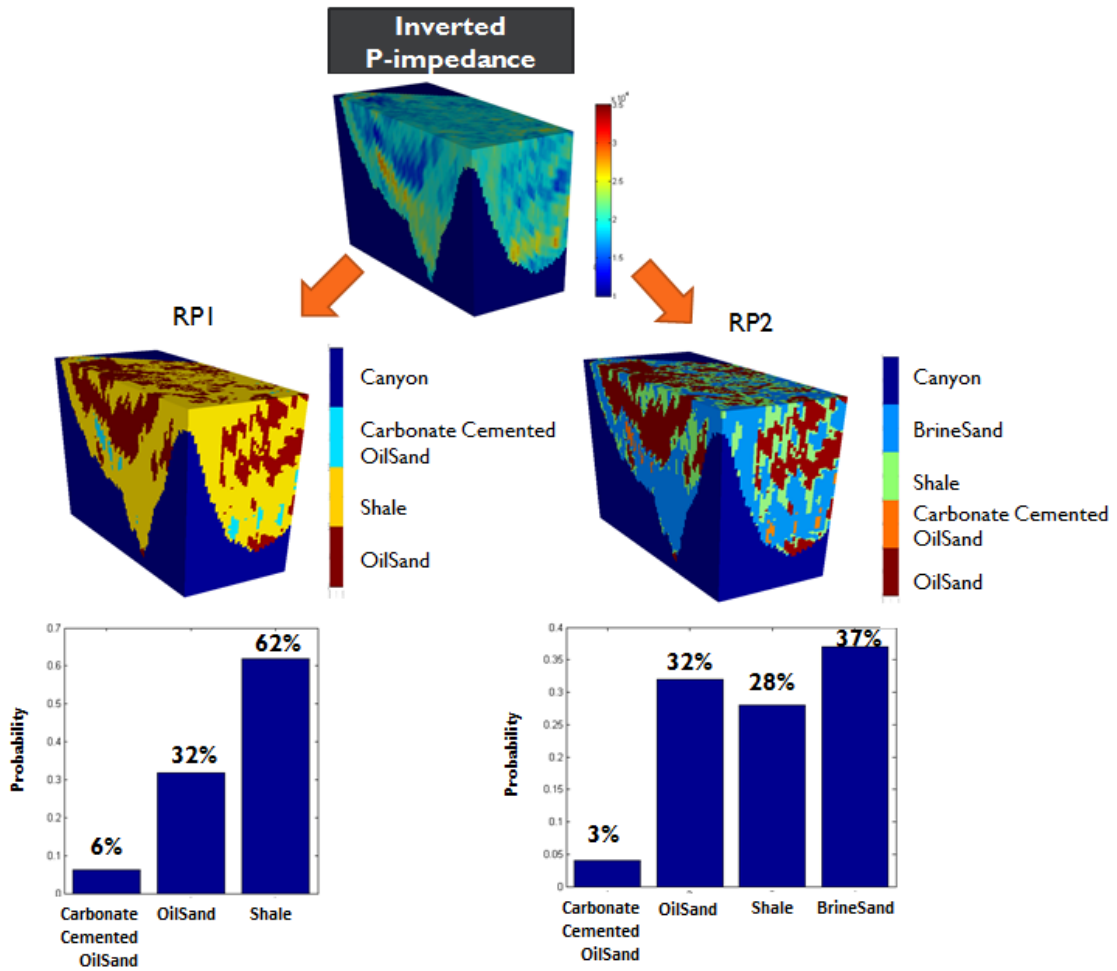


Figure 4. 10: Facies classification results from an inverted P-impedance cube using a Naïve Bayes classifier. Depending on the rockphysics models, facies classification results and their proportions can be very different. These classification results can be used as a guideline for the proportion of each facies.

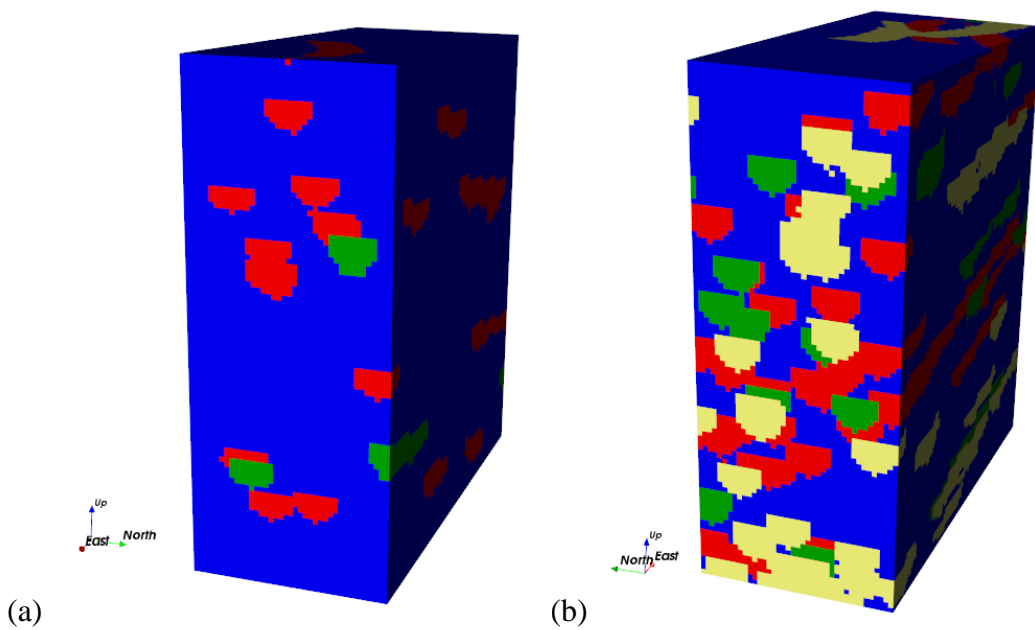


Figure 4. 11: (a) An example of the Earth model based on rockphysics model 1. The minimum values from each uniform distribution are applied for the example: 10% proportion for oilsand and 3% proportion for carbonate-cemented oilsand. (b) An example of the Earth model based on rockphysics model 2. The maximum values from a range of parameters are applied to generate the model: 25% proportion for oilsand. 25% proportion for brine sand, and 10% proportion for carbonate-cemented oil sand.

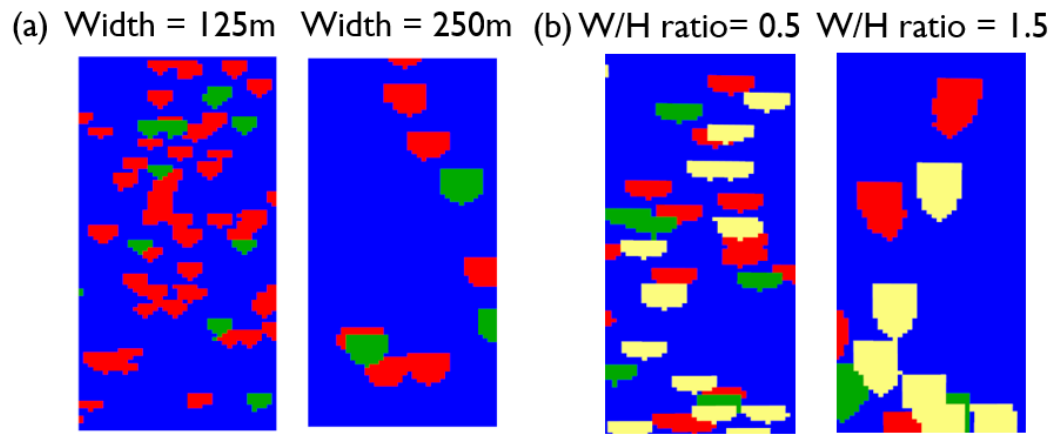


Figure 4. 12: (a) Examples of the width variation. The left model is made from a 125m wide sample while the right one is generated from with 250m as the width value. The both examples used the same Width/Height (W/H) ratio as 1. Since the 2D slice is vertically 25 times exaggerated, the W/H ratio 1 means 25m in horizontal and 1m in vertical. (b) Examples of the width/height ratio difference. Within the same width (250m wide), the left model uses 0.5 (5m deep) and right model uses 1.5 (15m deep) as the w/h ratio.

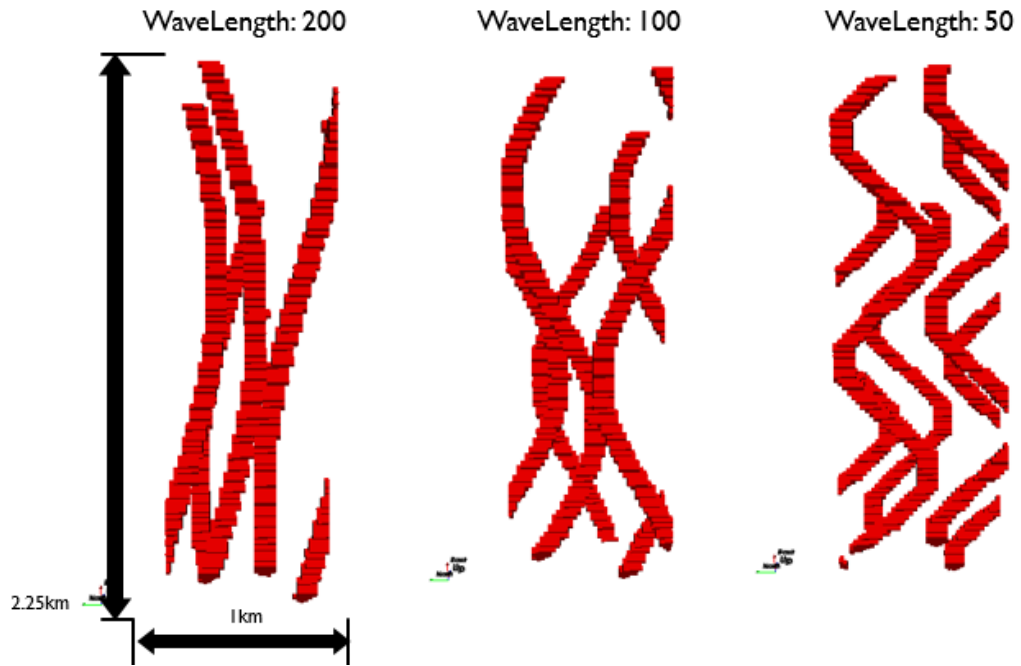


Figure 4. 13: A set of sinuosity variations from wavelengths 200 to 50. Note the wavelength value means the number of voxels between two peaks.

4.5.4 Spatial distribution uncertainty

Spatial distribution uncertainty is mainly about stacking patterns in geological scenarios. A stacking pattern is also a very important parameter for constructing an effective development plan. Clark and Pickering (1996) proposed various stacking patterns and geological possibilities for each. A vertical stacking pattern, which we call a “multi-storey” pattern here (see Figure 4.14(b)), is produced by focusing on the channel cutting and filling events leading to the pronounced differential compaction. Conversely, a lateral stacking pattern (“multi-lateral” in Figure 4.14(c)) commonly takes the form of systematic stacking in one direction, or alternating on either side of a pre-existing channel. Additionally, some unconstrained random stacking patterns can be classified as “isolated,” as shown in Figure 4.14 (a). Common characteristics of stacking patterns in turbidite channels are well summarized in Mayall et al. (2002) and Mayall et al. (2006).

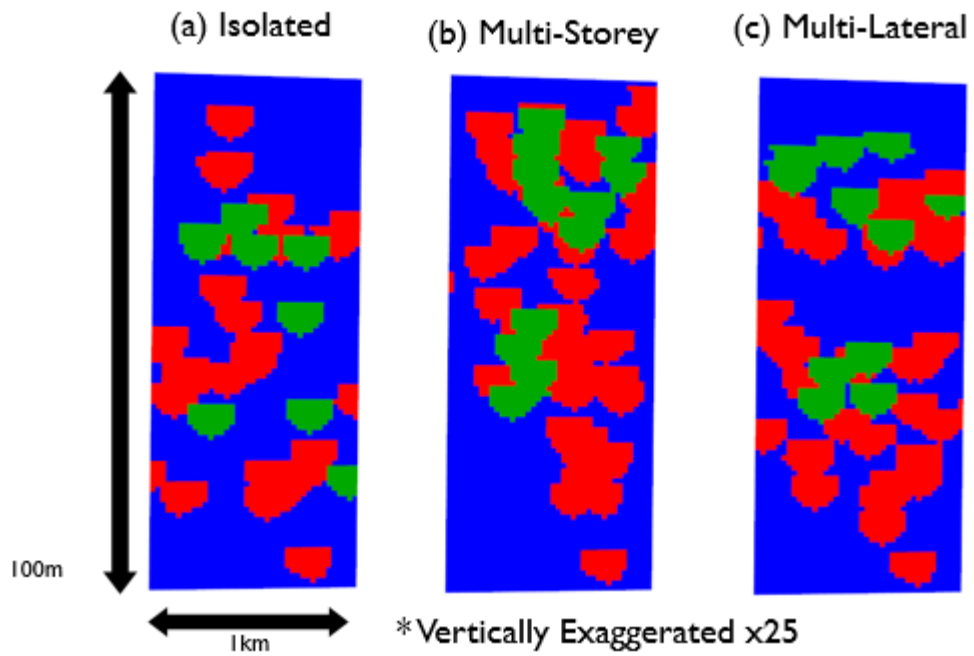


Figure 4. 14: Spatial distribution uncertainty is modeled as a wide variety of staking patterns. In this dissertation, we set up three stacking patterns for a series of turbidite channels: (a) isolated, (b) multi-story, and (c) multi-lateral.

4.5.5 Forward simulation for seismic data prediction

To compare the proposed geological scenarios to the given seismic data, we have to convert a facies model of geological scenario to corresponding seismic responses (see Figure 4.15). To predict the seismic data, we applied normal-incidence convolution model. Based on rockphysics relationship the facies model can be transformed to elastic property such as P-wave velocity and density. Then we calculate a normal incidence reflectivity from P-impedance. To predict a seismic section of seismograms, the normal incidence reflectivity is convolved with a wavelet trace by trace.

For the wavelet, we extract a well-tied wavelet from Hampson & Russell Software (HRS). Figure 4.16 and Figure 4.17 show the wavelet extraction results. One wavelet is directly extracted from well (See Figure 4.16) and the other one is deterministically selected among the preset wavelets in the HRS software (See Figure 4.17). Both wavelets show very good match compared to the seismograms of 2D seismic section and cross correlation coefficient was 0.6, respectively.

Conventionally, the well-tie wavelet extraction has some potential problems. At the well location, the seismic data should strongly correlate (or tie) with the synthetic seismogram generated by convolving the primary reflectivity series with an appropriate zero-phase wavelet. If there is a mis-tie, and the synthetic seismogram is then adjusted to make the tie through a time shift, or an adjustment to the amplitude spectrum of the wavelet, and an adjustment to the phase spectrum of the wavelet

(Nyman et al., 1987; Richard and Brac, 1988). We can make an almost perfect tie wavelet with the adjustment at any well location; however, the previously well-tied wavelet normally can make huge errors (a mis-tie) to the next well. Therefore, wavelet determination from well-tie location is still debatable.

To apply the wavelet for the whole seismic cube, the generalized Ricker wavelet can be a safer choice for forward simulation. Thus we use the zero-phase Ricker wavelet which shows a high cross-correlation at well location, for the normal incidence convolution model to generate seismic responses corresponding geological scenarios.

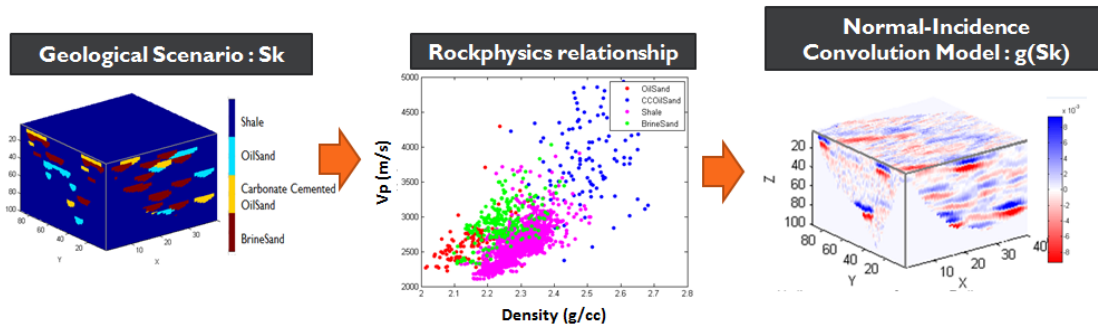


Figure 4. 15: A schematic diagram of forward simulation for seismic responses corresponding to the geological scenarios.

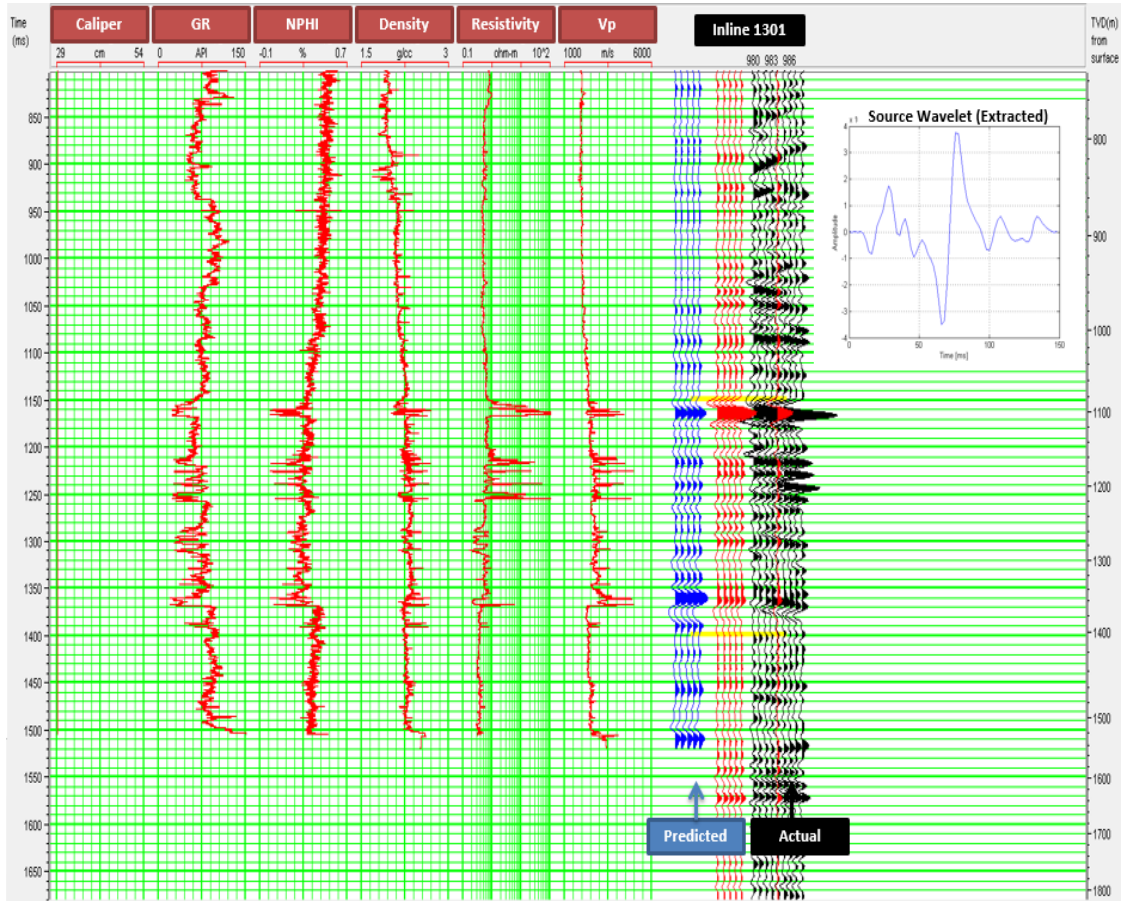


Figure 4. 16: Well-tied wavelet extraction in HRS software. A source wavelet is extracted in the software, and the predicted seismograms using the extracted wavelet (blue and red) and actual seismic section (black) are well matched.

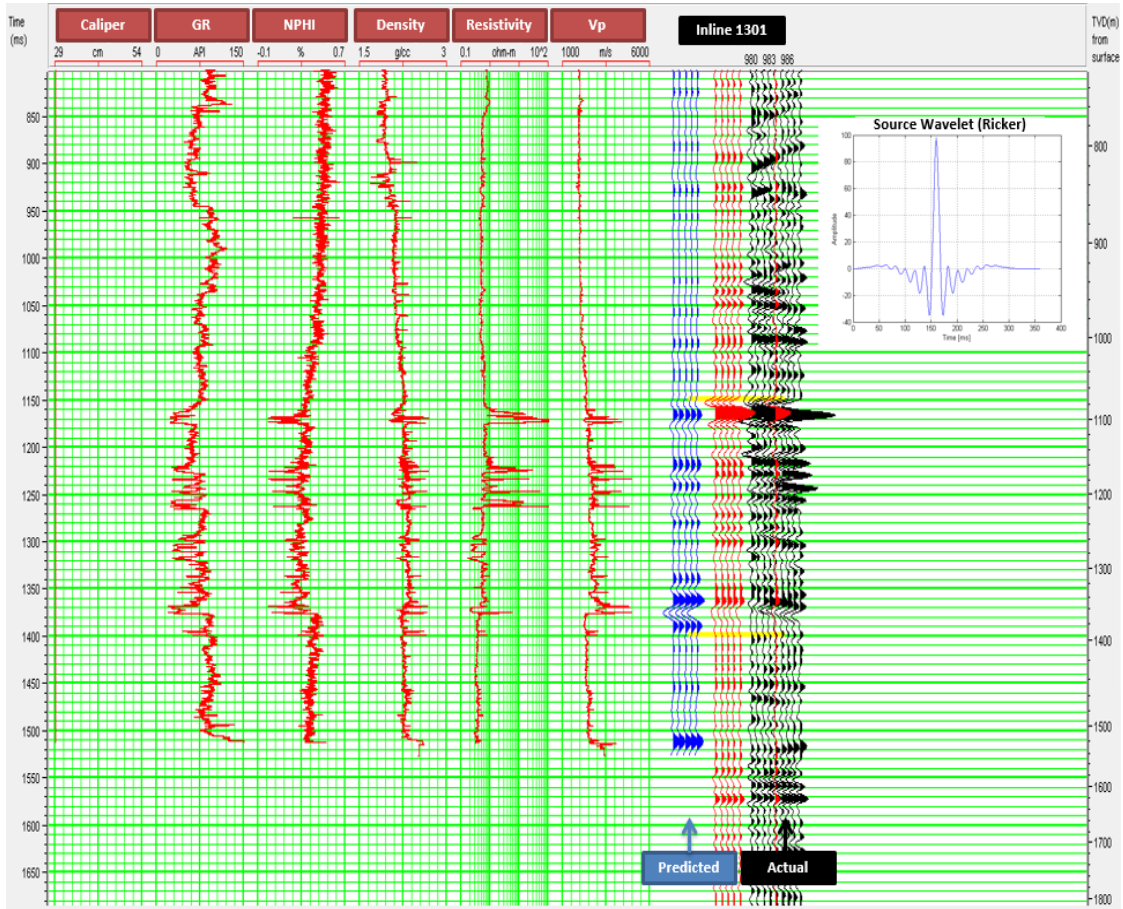


Figure 4. 17: Well-tied wavelet extraction in HRS software. Among the preset wavelets, Ricker wavelet shows the best match.

4.6 Results

4.6.1 Modeling geological scenario uncertainty

In this dissertation we propose to assess the consistency of all available geological scenarios with the given seismic amplitude data. Some examples of geological scenarios are shown in Figure 4.18. Note that each model is generated by a set of geological parameters randomly sampled from uniform distributions. The input range of uniform distributions is summarized in Table 4.1. To minimize a possible correlation between parameters, Latin Hypercube Sampling (LHS) design is applied for parameter sampling (Iman et al., 1980; Tang, 1993). Next, forward simulated geological scenarios and the obtained seismic data in the target grid are compared by distance-based pattern similarity (See Figure 4.19). Here we compare global patterns in seismic data instead of comparing local amplitudes trace by trace. Hence, we define the distance between seismic data and models based on the global pattern similarity.

We applied the Cluster-based Histograms of Patterns (CHP) algorithm (Honarkhah and Caers, 2010) as an improved version of MPH. Since the cluster-based histogram of patterns (CHP) lists only a few prototypes and their frequencies, instead of recording all patterns, it drastically reduce computing time and cost. In this case study, the CHP classifies 12,000 patterns in the given seismic data as 359 prototypes and counts its frequencies as a histogram. Next JS divergence determines a distance between the histograms recorded by the CHP for all realizations Figure 4.20 shows a MDS projection result of the distances calculated by the CHP and JS divergence.

Models from Rockphysics relationship 1 (RP1) and models from Rockphysics relationship 2 (RP2) consist of distinctive two clouds in MDS map. The data is surrounded by models in RP2. Through the MDS plot, we can infer that seismic patterns generated from RP2 are more probable than RP 1 models. Also our target zone and grid may include brine sand distribution away from well. Based on the distance, we can select a few models close to the data. To select the models, we use the Euclidean distance in MDS map (See Figure 4.21). Since the MDS map in 2D explains more than 71 % of total distribution of samples, the distance in MDS map can be used as a guideline of similarity. A cumulative frequency of histogram shown in Figure 4.22 supports the similarity in MDS map. The histograms of patterns are closer, the cumulative functions are more similar each other. The selected model in MDS map are marked by red curves and the data (marked by blue) shows very similar cumulative frequency of histogram to the red curves. The selected models and the assigned geological parameters for each model are summarized in Figure 4.23.

Due to the randomness of object-based modeling, the input parameters of selected model cannot perfectly guarantee the exact geological scenario setting in actual data. However, these can be a good approximation for promising geological scenarios or possible training images for data matching in seismic inversion process. The goal of this application is to sort the geological scenarios uncertainty from less likely scenarios to more likely ones. As the result, we could sort the geological scenarios and reduce a wide range of parameters to a smaller set of parameters. Now the selected models can be used as training images for seismic inverse modeling.

Figure 4.24 shows a MDS projection to estimate the probability of geological scenarios given seismic data among the most probable geological scenarios. We assume the nearest geological scenarios in Figure 4. 21 are equiprobable. Next, we regenerate 50 models from each promising geological scenario and recalculate the pattern-based distances. As the result we could observe the geological scenario 2 is much closer than the others. Kernel-Smoothing density estimation which is introduced in Chapter 2 shows the probability of scenario 2 given data is approximately 72%. Note that this value is just an approximately estimated probability among the models generated from the probable geological scenarios. However, based on the assessment, we can select a model from geological scenario 2 as a training image for seismic inverse modeling.

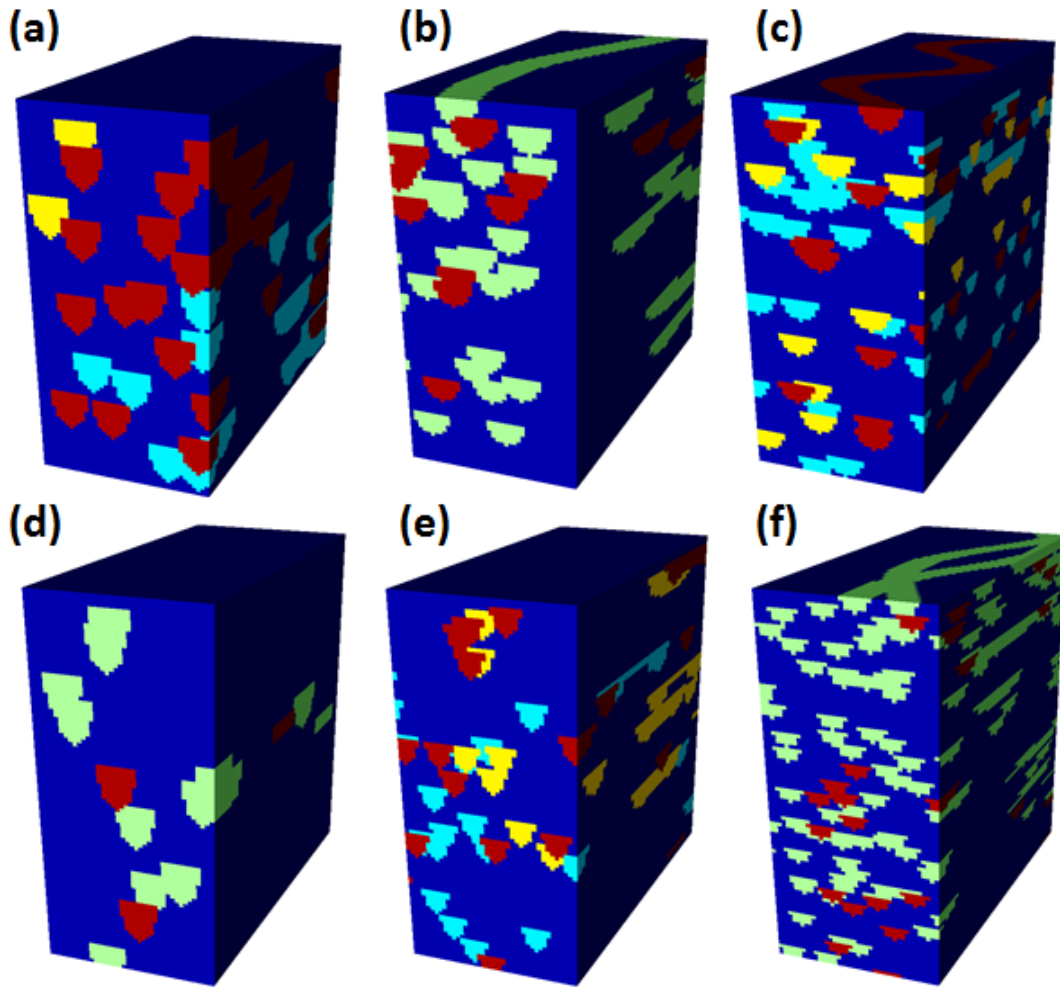


Figure 4. 18: Some examples of various geological scenarios. Compared to (a), (d) scenario contains smaller channel proportion with only two sand facies such as oil-sand (green) and carbonated cemented oil-sand (red). Stacking pattern in scenario (d) is multi-story (vertically stacked) while channels in scenario (a) spread out widely. We can see a variety of channel dimension from scenario (d), (e), and (f). A range of sinuosity is also shown in scenario (b), (c) and (f). Scenario (b) is less sinuous while scenario (c) has meandering channels.

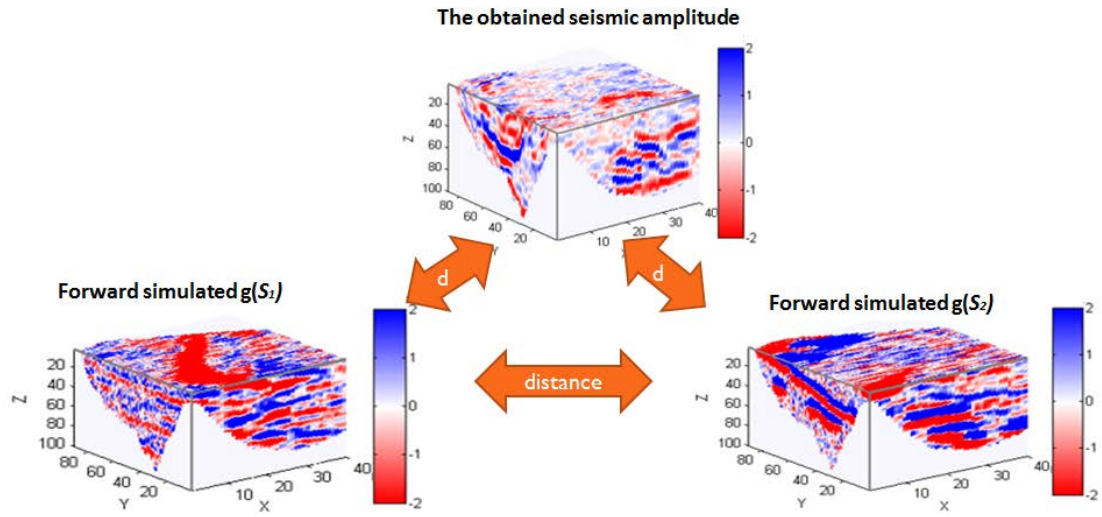


Figure 4. 19: A schematic diagram to calculate pairwise distances between the obtained seismic data and the forward simulated geological scenarios. Here we do not compare the local amplitude trace by trace but we globally compare the patterns and count the frequency of each pattern in seismic data.

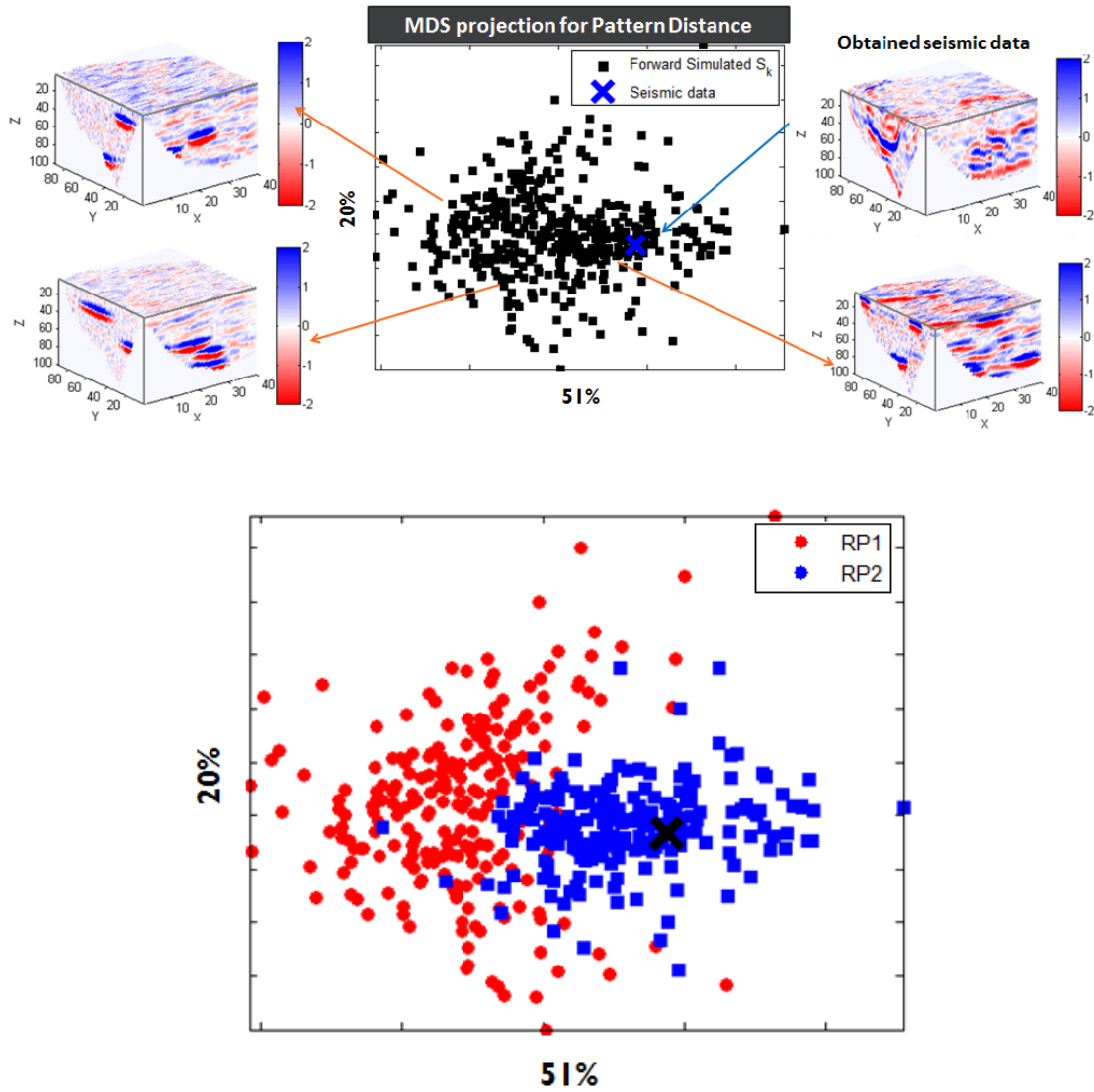


Figure 4. 20: A MDS projection of Cluster-based Histogram of Patterns (CHP) results using 450 models to obtain seismic data. The data (marked with a black cross) is located in the middle of blue clouds, and thus we can infer that rockphysics model 2 is more likely than rockphysics model 1 in the target grid of the case study.

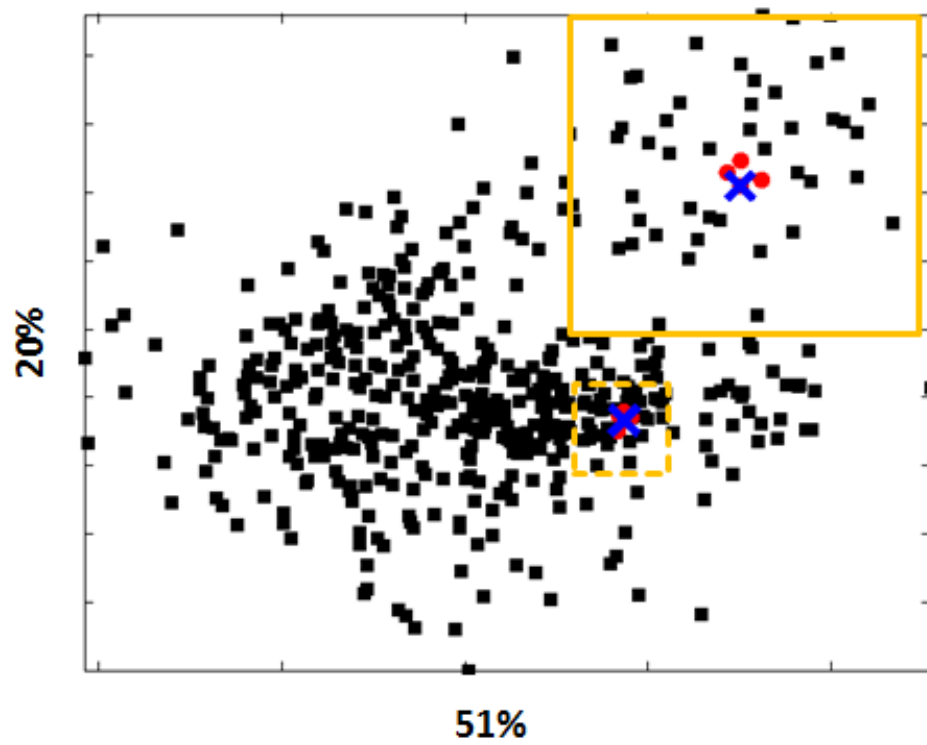


Figure 4. 21: To discover the most promising geological setting, close samples are selected. The models are selected by their distance from the data in MDS map (marked in red).

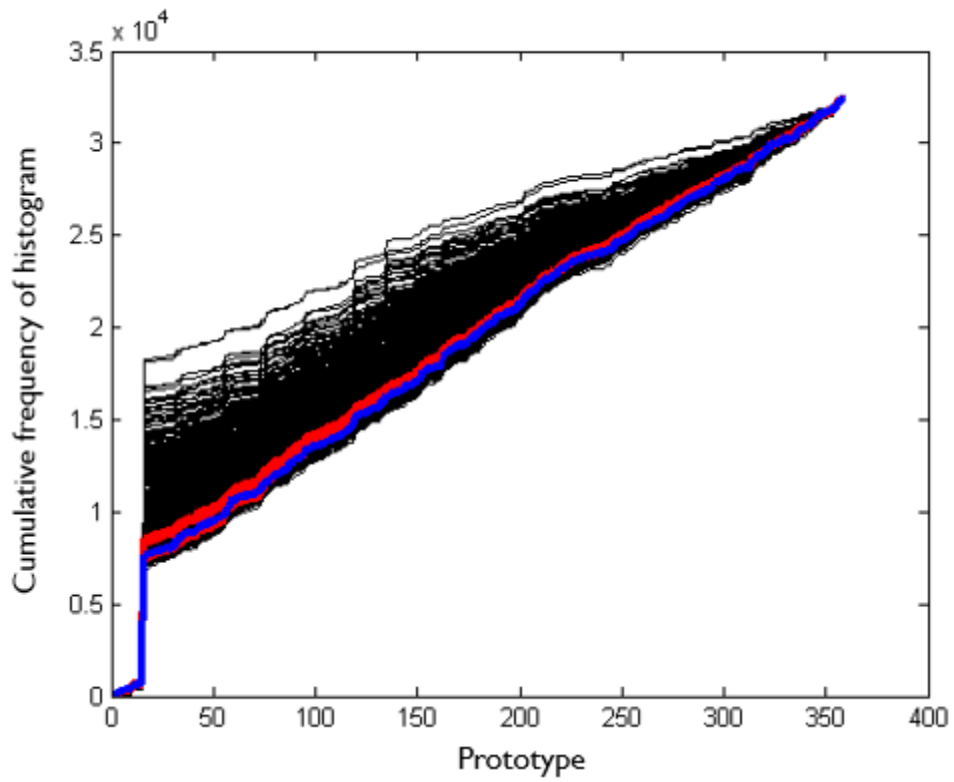


Figure 4. 22: A cumulative frequency of histogram for the CHP result. The histograms of patterns are closer, the cumulative functions are more similar each other. All prior models are plotted as black curves and the selected model in MDS map are marked by red curves. The data (marked by blue) shows very similar cumulative frequency of histogram with the red curves.

Table 4. 1: Input geological parameters for generating object-based models spanning the range of geological scenarios.

Priors Input Parameters			
	Minimum		Maximum
Stacking Pattern	Isolated	Multi-Storey	Multi-Lateral
Wave Length (m)	1250		5000
Width (m) Height (m)	W:125 H:2.5		W:250 H:15
Proportion OilSand (%)	13		50

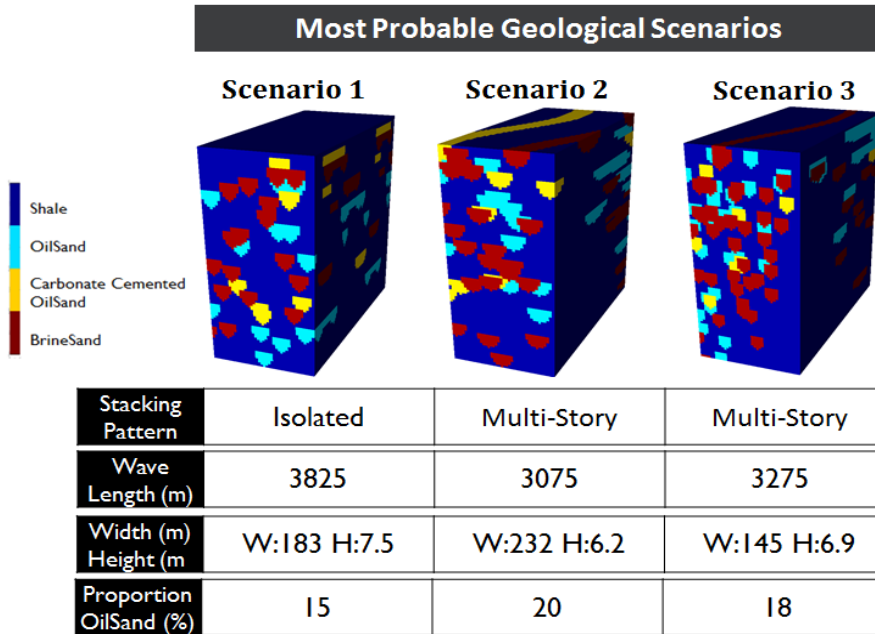


Figure 4. 23: Most probable geological scenarios and its geological parameters. Based on the MDS projection, all models from rockphysics model 2 are rejected, while a multi-story stacking pattern is promising in this study area. Also, we can observe that the range of proportion, width, and W/H ratio are relatively narrower than the initial input distribution.

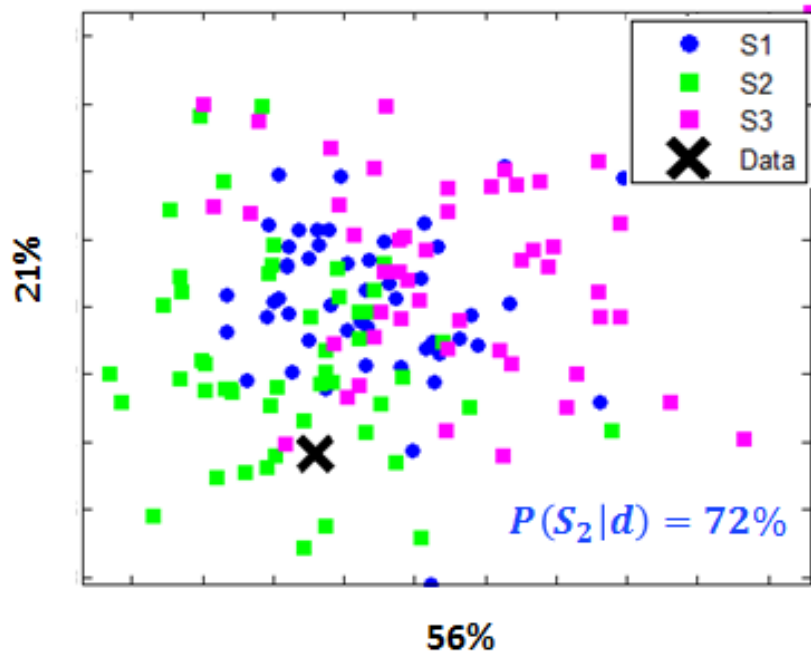


Figure 4. 24: Re-generated models based on the three nearest geological scenarios and its geological parameters. Based on the MDS projection and Kernel-Smoothing density estimation, geological scenario 2 is more likely among the selected scenarios.

4.6.2 Seismic inverse modeling conditioned to the geological scenario uncertainty

Based on the most probable geological scenarios, we could select a training image (or multiple training images) for seismic inverse modeling. Then a remaining goal is to sample a posterior distribution in a Bayesian framework. As introduced in Chapter 3, we applied the Metropolis sampler using ASR (M-ASR) to sample posteriors consistent with the all given data including geological scenario uncertainty. In this case study, we keep 0.5% subset points to preserve spatial information in current state.

Figure 4.25 shows a Markov chain of the adaptive spatial resampling. With iterations in a Markov chain, the overall Mean Absolute Error (MAE) between the obtained seismic data and forward simulated seismic data is getting smaller. After the burn-in period of 100 iterations, posterior models are sampled. Figure 4.26 shows cross-correlation coefficients between realizations after the burn-in period. Correlation between successive samples in the Markov chain goes down after 10 iterations, (cross-correlation coefficient is 0.14) and we sampled 20 posteriors by leaving out 10 samples between each selected sample. Note that we run an additional Markov chain in parallel after the burn-in for reducing sampling time. Depending on the computer setting, running multiple chains in parallel may drastically increase the sampling efficiency. However, a remaining issue is how to reach the posterior region rapidly. As we discussed in Chapter 3, M-ASR makes fast evolution to the low error zone using spatial error information. After burn-in, the M-ASR works like a pure Markov chain (i.e. M-ISR) because the spatial error is less informative than the burn-in period

containing larger errors.

One posterior realization and Ensemble average maps of the 20 posteriors are shown in Figure 4.27 and Figure 4.28, respectively. In Figure 4.28, we could observe channel shape connectivity in oil-sand and carbonate cemented oil-sand distribution. Since the ASR proposes a set of points from the previously accepted model for data-conditioning, MPS realizations may lose some channel shapes in a training image. However, each averaged ensemble of oil-sand and carbonate cemented oil-sand shows it preserves spatial connectivity in a training image while matching the given seismic data. Figure 4.29 shows an example of the matched 2D seismic section compared to the given data. Overall seismic reflections are very similar, and the cross-correlation calculated by each trace verifies the similarity.

One remaining challenge is to distinguish between brine-sand and shale. Due to the large overlap of P-impedance (See Figure 4.9 (b)), it is hard to differentiate brine-sand from background shale in the current normal-incidence seismic data (post-stack seismic data). Since we assign the P-velocity and density values corresponding to each facies based on the rockphysics model in Figure 4.6 (b), shale and brine-sand are highly uncertain. We can account for this as rockphysics uncertainty; however, it is really problematic in flow simulation level. Shale plays a barrier in flow simulation while sand channels are a main path of flow. A possible idea is to use S-wave velocity with multiple angle-stacked seismic data (pre-stack seismic data) for obtaining additional information to distinguish the distributions or minimize the overlap.

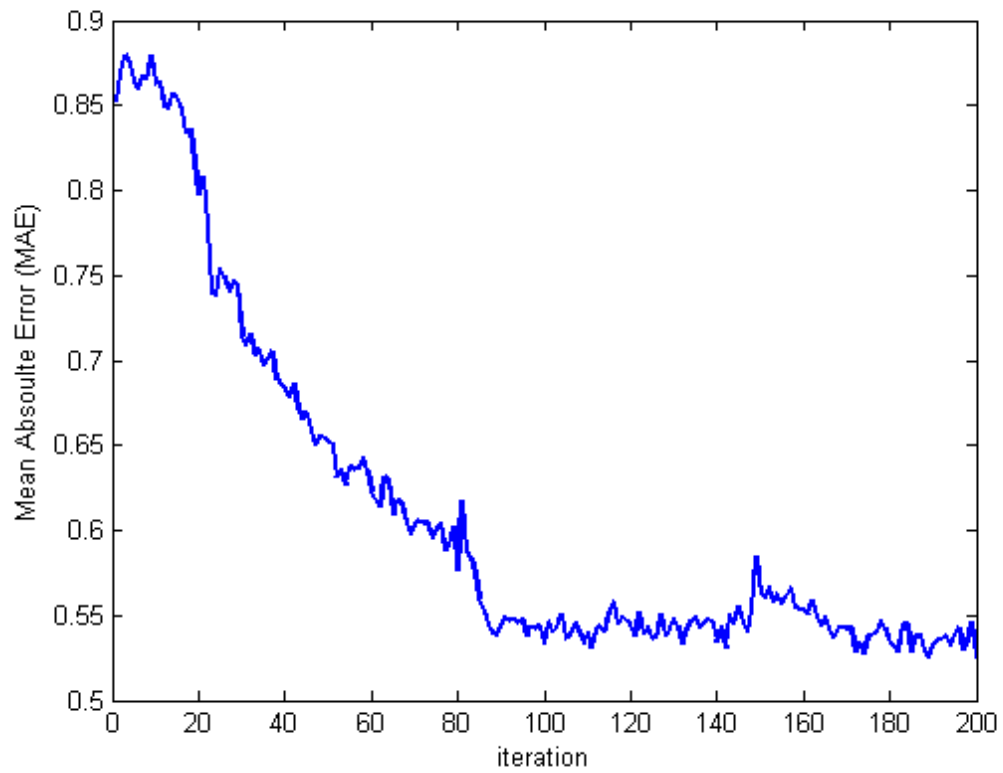


Figure 4. 25: A functional estimation of Mean Absolute Error(MAE) between the given seismic data and predicted one. With iterations, a Markov chain formed by ASR is getting closer to the posterior distribution.

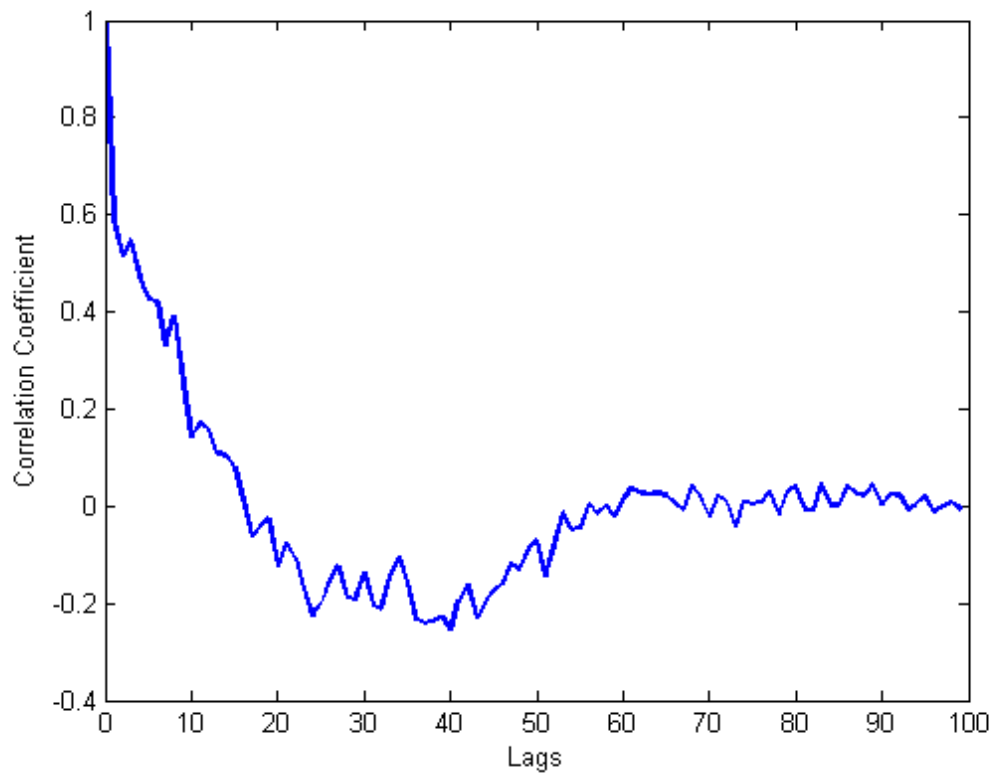


Figure 4. 26: Correlation coefficients after the burn-in period. To sample independent posteriors which are not correlated with a previous sample, we tested cross-correlation between models in a Markov chain after the burn-in period. After 10 iterations later, cross-correlation is almost disappeared (correlation coefficient is 0.14) and we setup this as a lag distance to sample posteriors.

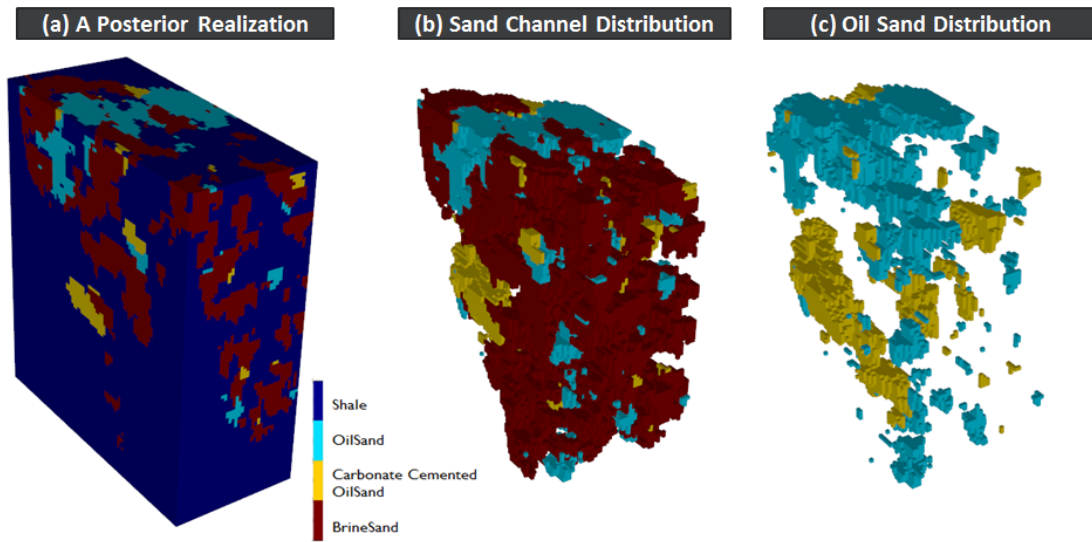


Figure 4. 27: (a) A sampled posterior from M-ASR. (b) A transparent image of the posterior and it shows all sand channel distributions. (c) Conditioned to geological scenarios and given seismic data, oil sand distribution (cyan) and carbonate cemented oil sand distribution (yellow) are predicted.

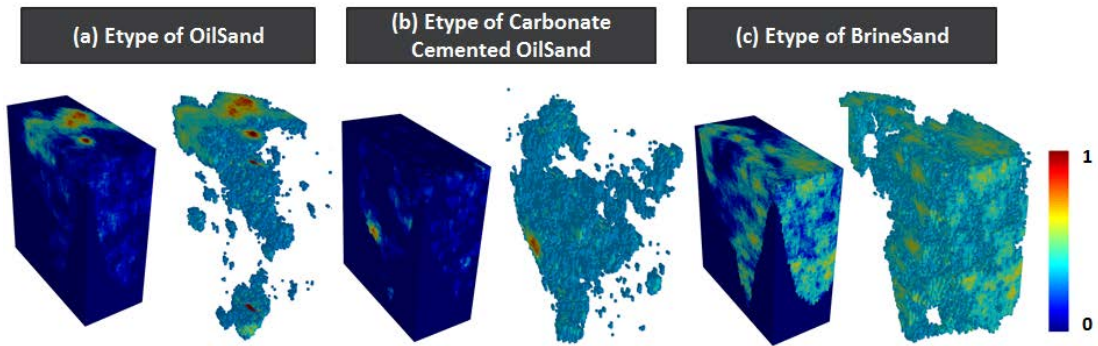


Figure 4. 28: An Ensemble average map of 20 posterior samples.

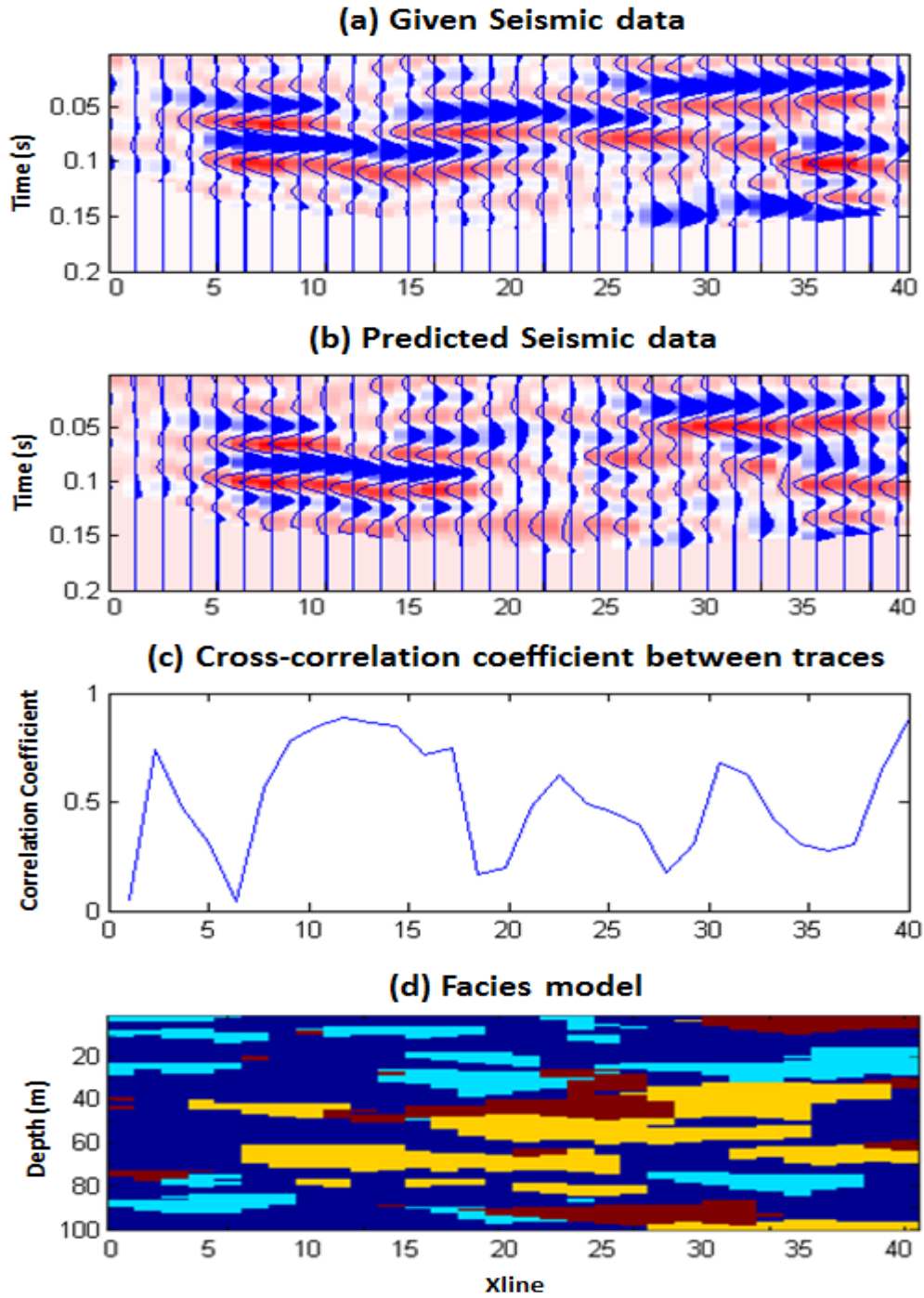


Figure 4. 29: 2D seismic section matching. (a) A 2D seismic section from the obtained seismic data, and (b) the forward simulated seismic section based on a facies model shown in (d). (c) Cross-correlation between (a) and (b) shows overall traces are matched well.

4.7 Conclusions

As the result of actual field case, the proposed approach sorts the available geological scenarios within given seismic data. Measuring pattern similarity based on CHP and JS divergence shows reasonable distinction in MDS map for two different rockphysics models. Based on the result, we can infer that seismic patterns generated from RP2 are more similar to the given seismic data than RP1. Thus we can reject the models from RP1. The goal of this workflow is to sort the geological scenarios uncertainty from less likely models to more likely ones. As the result, we could sort the geological scenarios and reduce a wide range of parameters to a smaller set of parameters. The selected models can be used as training images for seismic inverse modeling. As a fast approximate sampler, M-ASR (Metropolis sampler using Adaptive Spatial Resampling) samples a set of posteriors in a Bayesian framework. Through the sampled posteriors, we can predict channel distributions of each facies and its uncertainty.

An important challenge for actual field application is how to embody the geological observation into the object-based Earth models. Based on previous geological studies, we setup a wide range of geological parameters for building geological scenarios. As shown in the results, it is not necessary to use an experimental design using discrete parameter sets but we can use a set of continuous uniform distributions for discovering more likely geological scenarios. As a result, we

can pick some promising geological scenarios and its parameter settings from the projected MDS map. Using the selected geological scenario as a training image, M-ASR successfully samples the posterior consistent with seismic data and well data. Since the samples are originally generated from a training image based on the selected geological scenario, the final samples integrate all available data and geological scenario uncertainty.

4.8 Acknowledgement

This work was supported by the Stanford Center for Reservoir Forecasting (SCRF) sponsors. We acknowledge Hess Corporation for providing the data, and thank to Steve Graham, Tim McHargue, Scott Marler and Steve Uchytel for valuable discussions.

4.9 References

- Abreu, V., Sullivan, M., Pirmez, C., Mohrig, D., 2003, Lateral accretion packages (LAPs): an important reservoir element in deep water sinuous channels. *Marine and Petroleum Geology* 20, 631–648.
- Anderson, K., Graham, S., and Hubbard, S., 2006, Facies, architecture, and origin of a reservoir-scale sand-rich succession within submarine canyon fill: insights from Wagon caves rock (Paleocene), Santa Lucia Range, California, U.S.A: *Journal of*

- Sedimentary Research, 76, 819-838.
- Borg, I., Groenen, P. 1997. Modern multidimensional scaling: theory and applications, New-York, Springer.
- Caers, J., 2011, Modeling uncertainty in the Earth sciences, Wiley-Blackwell.
- Clark, J.D., Pickering, K.T., 1996, Architectural elements and growth patterns of submarine channels: applications to Hydrocarbon exploration. American Association of Petroleum Geologists 80 (2), 194–221.
- Cover, T. M., Thomas, J. A., 1991, Elements of information theory, Wiley-Interscience, New York, NY, USA.
- Dailly, P., Lowry, P., Goh, K., and Monson, G., 2002, Exploration and development of Ceiba Field, Rio Muni Basin, Southern Equatorial Guinea: The Leading Edge, 21, 1140-1146.
- Deutsch, C., Gringarten, E., 2000, Accounting for multiple-point continuity in geostatistical modeling, In: of Southern Africa, G. A. (Ed.), 6th International Geostatistics Congress. Vol. 1. Cape Town, South Africa, pp. 156-165.
- Endres, D. M. and Schindelin, J. E., 2003, A new metric for probability distributions, IEEE Transactions on Information Theory 49 (7), 1858-1860.
- Honarkhah, M. and Caers, J. 2010, Stochastic Simulation of Patterns Using Distance-Based Pattern Modeling, Mathematical Geosciences, 42: 487-517, DOI: 10.1007/s11004-010-9276-7.

- Iman, R.L., Davenport, J.M., Zeigler, D.K., 1980, Latin hypercube sampling (program user's guide), OSTI 5571631.
- Jobe, Z. R., Lowe, D. R., and Uchytíl, S. J., 2011, Two fundamentally different types of submarine canyons along the continental margin of Equatorial Guinea, *Marine and Petroleum Geology* 28: 843-860.
- Kullback, S., 1983, Kullback information, *Encyclopedia of Statistical Sciences*, Vo14, 421-425 New York: Wiley.
- Lange, K., Frydendall, J., Cordua, K. S., Hansen, T. M., Melnikova, Y., & Mosegaard, K., 2012, A Frequency Matching Method: Solving Inverse Problems by Use of Geologically Realistic Prior Information, *Mathematical Geosciences*, 44: 783-803, DOI: 10.1007/s11004-012-9417-2.
- Lowe, D.R., 2004, Report on core logging, lithofacies, and basic sedimentology of Equatorial Guinea, Hess internal report.
- Mayall, M., O'Byrne, C., 2002, Reservoir Prediction and Development Challenges in Turbidite Slope Channels: OTC Conference Proceedings, Contribution No. 14029.
- Mayall, M., Jones, E., and Casey, M., 2006, Turbidite channel reservoirs – Key elements in faces prediction and effective development, *Marine and Petroleum Geology* 23: 821-841.
- Normak, W. R., and Carlson, P. R., 2003, Giant submarine canyons; is size any clue to their importance in the rock record?, in Chan, M.A., and Archer, A.W., eds.,

- Extreme Depositional Environments; Mega End Members in Geological Time:
Geological Society of America, Special Chapter 370, p. 175–190.
- Nyman, D. C., Parry, M. J., and Knight, R. D., 1987, Seismic wavelet estimation using well control: 57th Annual International Meeting, SEG, 211–213.
- Park H., Scheidt C., Fenwick, D., Boucher A. and Caers J., 2013, History matching and uncertainty quantification of facies models with multiple geological interpretations, Computational Geosciences, DOI: 10.1007/s10596-013-9343-5.
- Richard, V., and Brac, J., 1988, Wavelet Analysis using well-log information: 58th Annual International Meeting, SEG, Expanded Abstracts, 946–949.
- Tang, B., 1993, Orthogonal Array-Based Latin Hypercubes, Journal of the American Statistical Association 88 (424): 1392–1397, doi:10.2307/2291282.
- Thomas, E. C., and Stieber, S. J., 1975, The Distribution of Shale in Sandstones and Its Effect Upon Porosity: Trans. Of the 16th Annual Logging Symposium of the SPWLA paper.

Chapter 5

Conclusion

*“The scientists of today think deeply instead of clearly.
One must be sane to think clearly, but one can think deeply
and be quite insane.”*

- Nikola Tesla

5.1 Summary

The work in this dissertation will enable reservoir modelers in the upstream petroleum industry to perform seismic reservoir characterization in a more geologically feasible way. This dissertation proposes a workflow in a Bayesian framework to integrate seismic data and various geological scenarios, as summarized in Equation (4.1). Chapter 2 covers how to estimate the probability of each geological

scenario given seismic data (i.e. $P(S_k|d)$, first part of Equation (4.1)), while Chapter 3 covers how to sample the posterior distribution within a given geological scenario and set of seismic data (i.e. $P(m_{res}|S_k, d)$, second part of Equation (4.1)).

Specifically, in Chapter 2, we present a methodology to screen prior geological scenarios based on seismic data. The statistical distance between seismic images is defined using pattern capturing algorithms (MPH or DWT), and JS divergence is capable of identifying geological scenarios consistent with the observed seismic response. This helps evaluate which less likely scenarios can be rejected. Using the proposed approach, we were able to reproduce quite accurately the probabilities obtained by rejection sampling, using only a fraction of the evaluations.

In Chapter 3, we present the Adaptive Spatial Resampling method (ASR) for seismic inverse modeling in a Bayesian framework. ASR perturbs realizations of a spatially dependent variable while preserving its spatial structure, with an accelerated sampling efficiency compared to ISR. It uses the residual error at each step of the Markov chain to guide the selection of conditioning data for the next step. In the studied cases, it yields posterior distributions reasonably close to those obtained by rejection samplers, with important reductions in time and computing cost. Thus, ASR appears to be suitable for reservoir characterization by conditioning facies models to spatially distributed seismic data.

In Chapter 4, we provide a practical formula for reservoir modelers, based on the studies in Chapters 2 and 3. An important challenge for actual field application is how

to embody geological observations into object-based Earth models. Based on previous geological studies and given geological observations, we set up a wide range of geological parameters for building geological scenarios. Instead of an experimental design using discrete parameter sets, we use a set of continuous uniform distributions to discover more likely geological scenarios. As a result, we can pick out promising geological scenarios and their parameter settings from the projected MDS map.

5.2 Future implications and visions

An immediate extension of our work would be different geological settings such as fans or levees, and different reservoir rocks such as a shale or a carbonate. The distance-based pattern similarity for modeling geological scenario uncertainty may be applicable to the other geological depositions and reservoir rocks to find out more promising geological settings.

Moreover, one can extend our work to make seismic reservoir characterization even more integrated, taking into account uncertainties related to variability in rockphysics uncertainty and seismic forward simulation uncertainty. In the case study in Chapter 4, we setup two possible rockphysics uncertainty based on the well data. However, if there were some completely unknown facies distributions away from wells, we cannot explain the obtained seismic data within the assigned rockphysics models and geological scenarios. Thus to keep a wide range of uncertainty is always the most important task for modeling geological scenario uncertainty. It is not only for

geological scenario uncertainty including rockphysics uncertainty, but also seismic forward simulation uncertainty. We extract wavelets from a well-tie study and use a Ricker wavelet for convolution modeling to generate synthetic seismic data. However, one can keep all available wavelets and test a wavelet uncertainty in pattern similarity comparison or seismic inverse modeling. It also can be extended to uncertainties in seismic data acquisition and interpretation.

Also one can extend our work with additional data such as partial-stack seismic data or production data. As discussed in Chapter 4, current well data and post-stack seismic data are not able to perfectly distinguish shale and brine-sand due to a large overlap of the P-velocity and density between the two facies. If we use some partial-stack (angle-stack) seismic data and S-wave velocity, we can reduce the uncertainty related to rockphysics. Even though there is a large uncertainty in seismic data, additional production data may reduce the uncertainty by rejecting unmatched flow simulation results.

A training image is often insufficient to explain actual spatial uncertainty in field and thus inefficient to find out a posterior distribution consistent with seismic data. Using multiple training images or geological scenarios equally likely (or with the estimated probability) at every model generation in a Markov chain can be an efficient solution for seismic inverse modeling in actual cases.

Lastly, the proposed workflow and methodology may be applied to other source of spatial data such as inverted CSEM (controlled-source electromagnetic) data or

inverted resistivity sections or GPR (ground penetrating radar) data, and other resources such as aquifer characterization.